LBNL-40923
UC-404

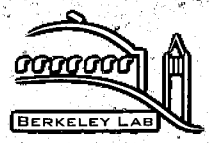

ERNEST ORLANDO LAWRENCE
BERKELEY NATIONAL LABORATORY

Equilibrium Vortex Motion in Two- and Three-Dimensional Superconductors Studied with a dc SQUID

Timothy J. Shaw

Materials Sciences Division

October 1997

Ph.D. Thesis

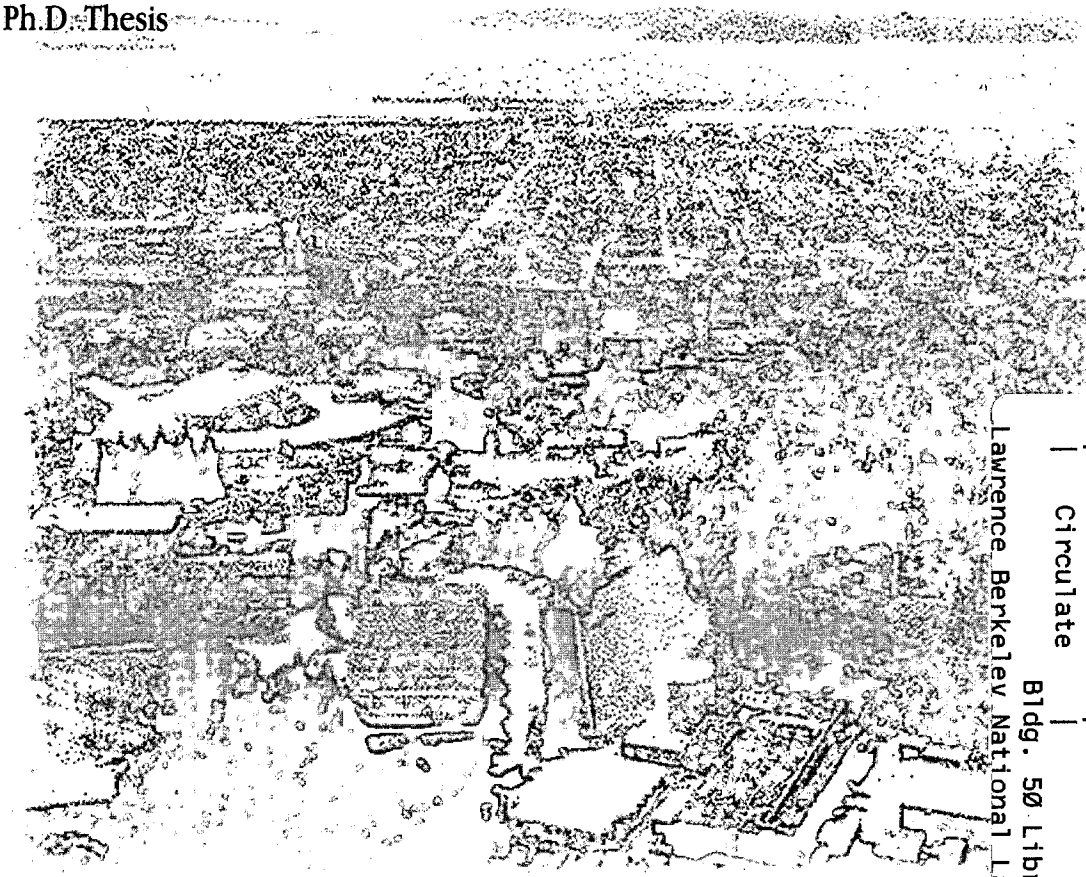

DISCLAIMER

LBNL-40923

Equilibrium Vortex Motion in Two- and Three-Dimensional Superconductors Studied with a dc SQUID

Timothy J. Shaw
(Ph.D. Thesis)

Department of Physics, University of California
and
Materials Sciences Division
Lawrence Berkeley National Laboratory
University of California
Berkeley, CA 94720

October 1997

This work was supported by the Office of Basic Energy Sciences, Materials Sciences Division of the U.S. Department of Energy under contract number DE-AC03-76SF00098.

Equilibrium Vortex Motion in Two- and Three-Dimensional Superconductors Studied With a DC SQUID

by

Timothy J. Shaw

M.S. (University of California) 1992
B.S. (Cornell University) 1990

A dissertation submitted in partial satisfaction of the
requirements for the degree of
Doctor of Philosophy

in

Physics

in the

GRADUATE DIVISION
of the
UNIVERSITY of CALIFORNIA at BERKELEY

Committee in charge:

Professor John Clarke, Chair
Professor T. Van Duzer
Professor Dung-Hai Lee

1997

Equilibrium Vortex Motion in Two- and Three-Dimensional Superconductors Studied with a dc SQUID

by

Timothy J. Shaw

Abstract

Equilibrium Vortex Motion in Two- and Three-Dimensional Superconductors Studied With a DC SQUID

by

Timothy J. Shaw

Doctor of Philosophy in Physics

University of California at Berkeley

Professor John Clarke, Chair

The equilibrium motion of vortices in two- and three-dimensional superconductors has been studied with a dc Superconducting QUantum Interference Device (SQUID). This technique has the advantage of probing the system in a non-invasive manner as well as providing dynamic information over many decades in frequency.

Through measurements of the spectral density of magnetic flux noise, $S_\Phi(\omega)$, as a function of temperature and applied magnetic field, the effects of proton and heavy ion irradiation on flux noise in crystals of $YBa_2Cu_3O_{7-\delta}$ have been measured and compared with the effects on the critical current, J_c. Both proton and heavy ion irradiation proved effective at reducing $S_\Phi(\omega)$, with proton irradiation having a larger effect. These changes are attributed to the change in defect structure caused by the irradiation, which also increased J_c. From the temperature dependence of $S_\Phi(\omega)$, the distribution of activation energies, $D(U_0)$, for vortex hopping ha been extracted. Irradiation moved the peak in $D(U_0)$ from ~ 0.2 eV before irradiation to ~ 0.1 eV after irradiation and greatly reduced its magnitude. The change in the total number of active vortices over the measurement temperature range caused by irradiation is attributed to creation of high-energy pinning sites. Finally, comparison of $S_\Phi(\omega)$ of the irradiated crystals to that of a typical thin film is argued to indicate that irradiation would not be a likely candidate for decreasing flux motion in superconducting magnetometers.

Measurement of $S_\Phi(\omega)$ due to the equilibrium Kosterlitz-Thouless-Berezinskii transition in two-dimensional Josephson Junction Arrays (JJAs) was studied as a function of

temperature for three different arrays and using three different sensors. $S_\Phi(\omega)$ is shown to obey dynamic scaling over as many as five decades in frequency, and estimates are made for the dynamic critical exponent z. An analytic theory for the high- and low-frequency behavior of $S_\Phi(\omega)$ is presented and compared to the measured data, with the result that the low-frequency behavior is well described by the theory but the high-frequency behavior is not. Other theories and numerical simulations are described and compared with the data, but none are completely satisfactory. Lastly, suggestions for necessary further theoretical work and possible future experimental work are suggested.

To my grandfather, who looked up at me about two years ago and said,

> "Tim, when are you going to graduate?".

When I replied that it would be about two years, he remarked,

> "You know, I'm over 80 years old now. You'ld better hurry up because I'm not sure how much longer I have."

Grandpa, we both made it.

Contents

List of Figures

List of Tables

List of Symbols

a ..... array lattice constant

$a(T)$ ..... non-linear current-voltage exponent

A ..... array area

$b, C, C_J, F, K, \kappa, \gamma$ ..... constants

$\mathbf{B}$ ..... magnetic field

B_z ..... magnetic field perpendicular to sensor due to vortices

d ..... array-sensor separation

dV/dI ..... differential resistance

D ..... vortex diffusion constant

$D(U)$ ..... distribution of activation energies

E_{barrier} ..... energy barrier for vortex moving between adjacent cells

E_c ..... vortex core energy

E_J ..... Josepshson coupling energy per junction

E_{pair} ..... creation energy of vortex-antivortex pair

f ..... frustration (fraction of Φ_0 per unit cell of array)

F_{Lorentz} ..... Lorentz force

$\mathcal{F}$ ..... scaling function

$g(r, \omega)$ ..... vortex response function

$g^V_{\ell_{\text{eff}}}$ ..... vortex number noise

g_θ ..... zeroth-momentum phase correlation function

$G(r, r')$ ..... two-dimensional lattice Green's function

H ..... Hamiltonian

i_c ..... critical current per junction

I ..... current

I_b ..... SQUID bias current

J_c ..... critical current density

ℓ ..... vortex hopping distance

ℓ_{eff} ..... sensor diameter

ℓ_ξ ..... $\ell n(\xi/r_0)$

ℓ_ω ..... $\ell n(r_\omega/r_0)$

L_k ..... superfluid kinetic inductance

$\mathcal{M}$ ..... array-sensor coupling function
M_f ..... SQUID-modulation coil mutual inductance
n ..... total vortex density
N ..... integer
p ..... vortex density tuning parameter of Coulomb gas model
r_ω ..... characteristic vortex separation
r_0 ..... minimum vortex separation
R ..... system size
R_b ..... transformer blocking resistor
R_f ..... feedback resistor
s ..... superconductor thickness
$S_\Phi(\omega)$ ..... spectral density of magnetic flux noise
S_Φ^w ..... magnitude of spectral density of white noise
T_c ..... bulk transition temperature
T' ..... effective temperature
T_{KTB} ..... KTB transition temperature
T'_{KTB} ..... effective temperature at the KTB transition temperature
U ..... vortex pinning energy
V_f ..... feedback voltage
w ..... width of SQUID washer
W ..... noise function
Y ..... characteristic parameter of regime interpretation
z ..... dynamic critical exponent
α ..... slope of $S_\Phi(\omega)$ on a log-log plot at high frequency
α_R ..... damping parameter
$\beta(T)$ ..... temperature parameter for thermally-activated vortex hopping
γ ..... critical current parameter
Γ ..... Langevin equation damping parameter
Γ_0 ..... single junction phase diffusion rate
δ ..... Dirac delta function
ϵ ..... vortex dielectric constant
$\tilde{\epsilon}_{cg}$ ..... Coulomb gas vortex gas dielectric constant
$\tilde{\epsilon}(r)$ ..... length-dependent vortex dielectric function

ϵ_b ..... vortex dielectric constant due to bound vortices
ϵ_f ..... vortex dielectric constant due to free vortices
ϵ_c ..... vortex dielectric constant at KTB transition temperature
ε ..... vortex line energy
ζ ..... scaling parameter
η ..... fluctuating noise
θ ..... phase of superconducting order parameter
Θ ..... step function
λ ..... penetration depth for perpendicular fields
λ_{cg} ..... Coulomb gas screening length
Λ_{vv} ..... vortex-vortex correlation function
μ_0 ..... permittivity of free space
ξ ..... correlation length of KTB transition
ξ_0 ..... minimum free vortex separation
ρ_v ..... free vortex density
σ ..... effective vortex conductivity
τ ..... attempt time
Υ ..... form factor of sensor
Φ_0 ..... superconducting flux quantum
Φ_{ac} ..... SQUID ac modulation flux
Φ_{qs} ..... quasistatic flux
Ψ ..... superconducting order parameter
ω ..... angular frequency
ω_ξ ..... characteristic frequency of KTB transition
ω_{cg} ..... characteristic frequency of Coulomb gas model
ω_{cut} ..... crossover frequency to $1/\omega^{3/2}$ or $1/\omega^2$ noise
ω_{hop} ..... characteristic frequency of vortex diffusion
ω_{ld} ..... characteristic frequency of local damping model

Acknowledgements

I am greatly indebted to my advisor, John Clarke, for taking me on as a graduate student and providing excellent guidance and insight for the many projects, both successful and unsuccessful, in which I have participated. His ability to know which studies will be interesting and experimentally feasible, as well as to see directly to the heart of a complicated issue, are traits of which I hope to have inherited a small part. In addition, I would like to thank my thesis committee for their work, useful comments, and suggestions.

Nearly all of the apparatus and samples which made the work described in this thesis possible were provided by others. I have benefitted richly from the hard work and helpful hand of Mark Ferrari who built the apparatus used to make all the measurements, which lasted from the advent of high-temperature superconductivity to the present, and who took me under his wing at the outset of my studies. His knowledge and work methods set the tone for the remainder of my work. The YBCO crystals were grown by Alice White and their critical current was measured by Bruce van Dover. I am grateful to both of them, and especially to Bruce for his helpful discussions regarding pinning and irradiation effects in high-temperature superconductors. I am also indebted to Lydia Sohn for providing the Josephson junction arrays. Lastly, none of the measurements would have been possible without the processing skills of Fred Wellstood, Tom Lee, Dinh Ton, and Mark Ketchen who provided the SQUIDs.

Although this thesis is concerned only with the scientific aspects of my work, I would like to thank the many people who made the rest of my life enjoyable during my graduate studies. Gene Dantsker, Tom Lee, Yann Chemla, and Marc-Olivier André all made the basement of Birge Hall an enjoyable workplace, sharing their ideas on physics and the other important things in life. Most importantly, Isabel Zumel has been a continual source of inspiration as well as making two and a half years of my graduate studies some of the most remarkable in my life.

I consider it a privilege to have been paid to pursue a PhD and the directions of my curiosity, and for that I thank the Department of Energy's Lawrence Berkeley National Laboratory.

Finally, I owe a world of gratitude and thanks to my family and friends who consoled me in times of melancholy and celebrated with me in times of joy.

Preface

A Ph. D. thesis should, I believe, satisfy two criteria. First, and foremost, it should present a clear and precise demonstration of original research worthy of the degree. Second, and almost as importantly, it should contain a more detailed description of the methods and thought processes that went into the work than would appear in scientific journals, so that future researchers might find it to be a valuable reference.

To these ends, the following pages describe a portion of the research that I have done during my studies at Berkeley. I have attempted, wherever possible, to make it relatively self-contained in so far as it should be possible to understand the body of the work without reference to other sources. In addition, there appear rather detailed descriptions of the experimental apparatus and techniques which I hope will provide details which one often only obtains from the physicists with whom one works, such as the type of adhesive used in a cryogenic measurement which, although seemingly minor, nevertheless play an important role in the functioning of an experiment. Lastly, I have drawn heavily on the theoretical work of others and have attempted, rather than just to cite the results, to provide details and insights into the calculations which are relevant to the measurements and which might provide a perspective not contained in the original work.

Chapter 1

Introduction

The research presented here is comprised of the results and analysis of two rather different projects, but with a common thread–the study of equilibrium vortex motion in superconducting materials. The first project, the study of the effects of proton and heavy-ion irradiation on the pinning properties of $YBa_2Cu_3O_{7-\delta}$ (YBCO) well below the superconducting transition temperature, was motivated by two factors, a desire to understand the nature of pinning defects caused by irradiation and the hope of finding a technique to reduce the effects of vortex motion on the performance of superconducting magnetometers. This study of vortex pinning led to a project with the motivation of understanding vortex motion and the superconducting transition on a more fundamental level. In order to do so, we chose to examine a system in which pinning is unimportant and which is also much more uniform than high-temperature superconductors such as YBCO, namely a two-dimensional Josephson junction array (JJA). These arrays have long been regarded as an ideal system to study the two-dimensional metal-superconductor transition (commonly called the Kosterlitz-Thouless-Berezinskii [KTB] transition after the authors who first gave a foundation for its understanding) [5, 6, 7], and the understanding of this phase transition could lead to a better understanding of the superconducting transition in the quasi-two-dimensional high-temperature superconductors such as $Bi_2Sr_2CaCu_2O_{8+\delta}$. Before going into the details of the measurements and their interpretations, I will give a general overview of vortices in two- and three-dimensional superconductors, pinning in high-temperature superconductors, and the KTB transition.

1.1 Vortices in Two- and Three Dimensional Superconductors

The magnetic properties of superconductors can be well described by a complex order parameter, Ψ, as originally proposed on a phenomenological level by Ginzburg and Landau[8] and later justified as derivable from the microscopic theory of Bardeen, Cooper, and Schrieffer[9] by Gorkov[10]. The magnitude of Ψ can be understood as being proportional to the density of superconducting electrons, and the gradient of the phase is proportional to the current. In a famous publication, Abrikosov[11] showed that for $\lambda/\xi > 1/\sqrt{2}$, where λ is the penetration depth for perpendicular magnetic fields and ξ is the correlation length, a magnetic field larger than the lower critical field enters the superconductor in the form of flux vortices, each containing a single quantum of magnetic flux, $\Phi_0 = hc/2e$.

The structure of a vortex is very different in two- and three-dimensional superconductors. A vortex in a three-dimensional superconductor is shown schematically in Fig. 1.1. The order parameter goes to zero at the vortex center and approaches the bulk value on the scale of ξ, and the magnetic field is a maximum in the center and decays towards zero with the characteristic length scale λ. In a two-dimensional JJA, or in any two-dimensional superconductor, the situation is very different. The system can be modelled in a similar manner as for three-dimensional materials, in which the order parameter is zero at the center of the vortex and approaches the bulk value on the characteristic length scale of the core size (which I will call r_0 in order to not confuse it with another correlation length traditionally called ξ to be discussed in Chapter 4), but the perpendicular penetration depth is infinite. Since real materials are never two-dimensional, there is a finite penetration depth, but as far as the topics to be discussed here are concerned, λ is infinite in the JJAs.

The differences between vortices in two and three dimensions has important implications on the energy needed to create a vortex as well as the interaction between vortices. The energy needed to create an isolated vortex in a three-dimensional superconductor is approximately (see, for example, Ref. [1])

$$E_{3\mathrm{d}} \approx \frac{s\Phi_0^2 \ell n(\lambda/\xi)}{4\pi\mu_0\lambda^2}, \tag{1.1}$$

where s is the thickness of the superconductor along the vortex axis, whereas for a two-dimensional JJA the creation energy is (see, for example, Ref. [12])

$$E_{2\mathrm{d}} = \pi E_J \ell n(R/r_0) + E_c, \tag{1.2}$$

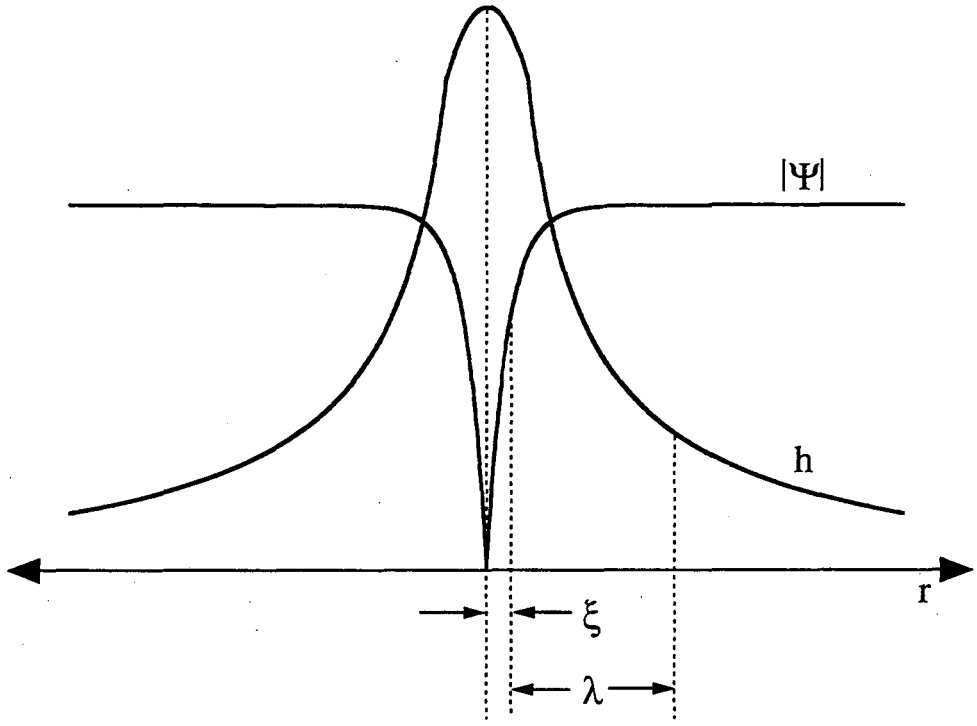

Figure 1.1: Structure of a vortex in a three-dimensional superconductor. The magnitude of the order parameter, $|\Psi|$ represents the superfluid density, and h is the value of the local magnetic induction. From Ref. [1].

where E_J is the Josephson coupling energy per junction, E_c is the core energy, and R is the size of the system. The important difference here is that in a two-dimensional system the creation energy grows with the system size. In addition to the difference in isolated vortex creation energies, the interaction between vortices is very different in two- and three-dimensions. The circulating current around a vortex decays as a function of distance from the core as

$$I(r) \propto 1/r \qquad \xi \ll r \ll \lambda \tag{1.3a}$$

$$e^{r/\lambda}/r^{3/2} \qquad r \gg \lambda \tag{1.3b}$$

in three dimensions, and has the dependence

$$I(r) \propto 1/r \tag{1.4}$$

in two dimensions. The force exerted on another vortex by this current is given by the

Lorentz force

$$\mathbf{F}_{\text{Lorentz}} = \mathbf{I} \times \Phi_0. \tag{1.5}$$

Therefore, from an examination of Eqs. (1.3)–(1.4) it is evident that vortices with large separation have negligible interaction in three dimensions whereas the interaction is extremely long-ranged in two dimensions.

1.2 Vortex Pinning in High-Temperature Superconductors

Pinning is a generic term for the tendency of vortices to be preferentially attracted to certain regions of the sample due to inhomogeneities. There are many types of defects which can cause pinning, as described in the monograph of Campbell and Evetts[13] and the text by Ullmaier[14]. The most common are regions where Ψ is suppressed by local structural defects which allow the vortex core to save condensation energy by passing through the defect region, and surface roughness, which reduces the total energy of the vortex in thinner regions by allowing it to minimize its length. For the small magnetic fields in which the work here was carried out, the vortices have an average separation much greater than λ and via Eqs. (1.3) and (1.5) can be considered non-interacting. In this field regime, pinning and thermal excitations are the dominant mechanisms determining vortex motion, and the interaction of vortices and structure of the vortex lattice predicted by Abrikosov[11] are irrelevant.

1.3 Two Dimensions and the Kosterlitz-Thouless-Berezinskii Transition

The system-size-dependent vortex creation energy and long range vortex interaction discussed above have important implications on the existence of superconductivity in two dimensions. This can be seen by examining the creation energy for an isolated vortex in Eq. (1.1). A rough estimate of the possibility of an isolated vortex can be made by noting that the for a system of size R, the vortex core can be located in approximately $(R/r_0)^2$ different locations. Its entropy is then $k_B \ln[(R/r_0)^2]$ and the free energy cost for creating an isolated vortex is $(\pi E_J - 2k_B T)\ell n(R/r_0)$. Therefore, free vortices will be favorable for $T > \pi E_J/2k_B$ and even for temperatures at which the sample would be superconducting in three dimensions, namely when there is a finite superfluid density, isolated vortices can

occur which make the sample have a finite static resistance. The low-temperature phase, in which there are no isolated vortices, can be understood by noting that the energy needed to create a vortex-antivortex pair of separation r is (see, for example, Ref. [15])

$$E_{\rm pair}(r) = 2\pi E_J \ell n(r/r_0) + 2E_c. \tag{1.6}$$

Since the size of the system does not appear in the pair creation energy of Eq. (1.6), the low-temperature phase will consist of an equilibrium density of bound vortex-antivortex pairs, and the transition to the resistive state in this rough argument occurs at a temperature

$$T_{\rm KTB} = \pi E_J / 2k_B. \tag{1.7}$$

The transition to the superconducting state in two dimensions occurs below the bulk transition temperature as described above. This phase transition is driven by fluctuations in the phase of the order parameter in the form of vortices, in sharp contrast to the three dimensional superconducting transition (in small magnetic fields) in which fluctuations in the magnitude of the order parameter drive the transition.

Chapter 2

Experimental Techniques and Samples

2.1 Flux Noise Measurements

2.1.1 Cryogenic Insert

The apparatus used to carry out the flux noise measurements to be described in this thesis was designed by Mark Ferrari for the purpose of studying vortex motion in high-temperature superconductors[16]. Subsequently, I made modifications to provide a larger frequency bandwidth and an improved sample alignment technique as will be described below. The main goal of the design was to provide an ideal environment for the heart of the apparatus, a dc Superconducting Quantum Interference Device (SQUID) (namely at a temperature well below the ~7 K transition temperature and free from large static and varying magnetic fields), while allowing a sample at a temperature up to about 130 K to be placed within 100 μm of the SQUID. The insert which satisfied these criteria is shown in Fig. 2.1, and fits inside of a fiberglass, superinsulated, liquid helium dewar. A mu-metal shield surrounds the dewar and reduces the earth's magnetic field to less than 1 μT, and a lead can surrounding the vacuum can drastically reduces fluctuating fields, the worst of which are due to the ubiquitous 60 Hz noise. The plumbing is relatively standard for cryogenic studies – a vacuum line to a vacuum can with an indium o-ring seal clamped with eight screws. A helium transfer line allows the five liter dewar to be filled without removing the insert.

The heart of the apparatus is shown in Fig. 2.2, and consists of a hot side and a

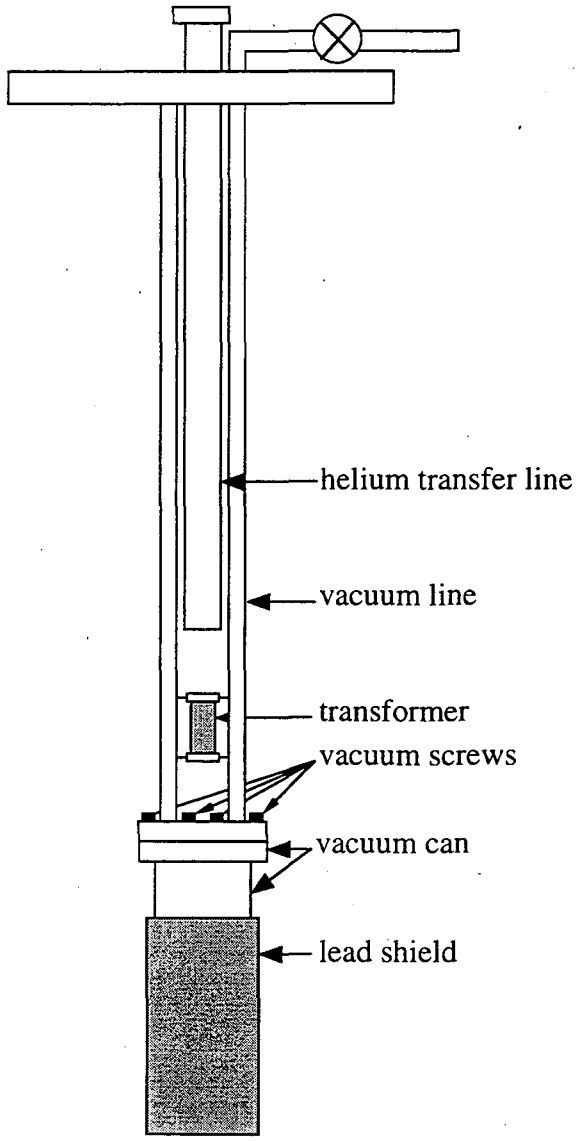

Figure 2.1: Schematic drawing of cryogenic insert.

cold side. The cold side is formed by a $\sim$ 1 cm $\times$ $\sim$ 10 cm $\times$ 0.75 mm sapphire stage which is attached by a copper clamp to a copper plate which is in turn soldered to the top of the vacuum can, thereby providing good thermal contact between the sapphire stage and the liquid helium bath. Since the sapphire is relatively fragile, it is supported by a thick piece of fiberglass, which was chosen over metal in order to avoid excess noise at the SQUID due to Johnson noise currents.

An expanded view of the hot and cold sides is shown in Fig. 2.2(b). On one side of the sapphire stage, the SQUID substrate is mounted with vacuum grease. On the reverse side a superconducting persistent-field coil is glued (with Miller-Stephenson epoxy). This coil has an outer diameter of 1.2 cm, an inner diameter of 0.75 cm, and consists of 450 turns of 3 mil niobium wire. Inside the field coil is a 10 turn concentric coil used to provide the alternating and feedback flux necessary to operate one of the SQUIDs.

The hot side consists of sample stage, on one side of which is mounted the sample and on the other side of which is mounted a thermometer and a resistive heater. Two different sample stages were used, one of which has a silicon sample stage and another with a sapphire stage. The thermal isolation between the the hot and cold sides was realized using two different methods. The first, as discussed in Ref. [16], employed Macor spacers between which was placed plastic bristles (such as those found in pastry brushes). Since this method was difficult and not very mechanically stable, and resulted in the destruction of at least one SQUID, a second method was used in which sharpened brass screws provided the thermal isolation and, in addition, allowed the separation between the SQUID and sample to be easily adjusted. Brass was chosen because of its relatively low thermal conductivity at liquid helium temperatures and its small thermal contraction (as opposed to nylon or other plastic), but more importantly because it is not highly magnetic.

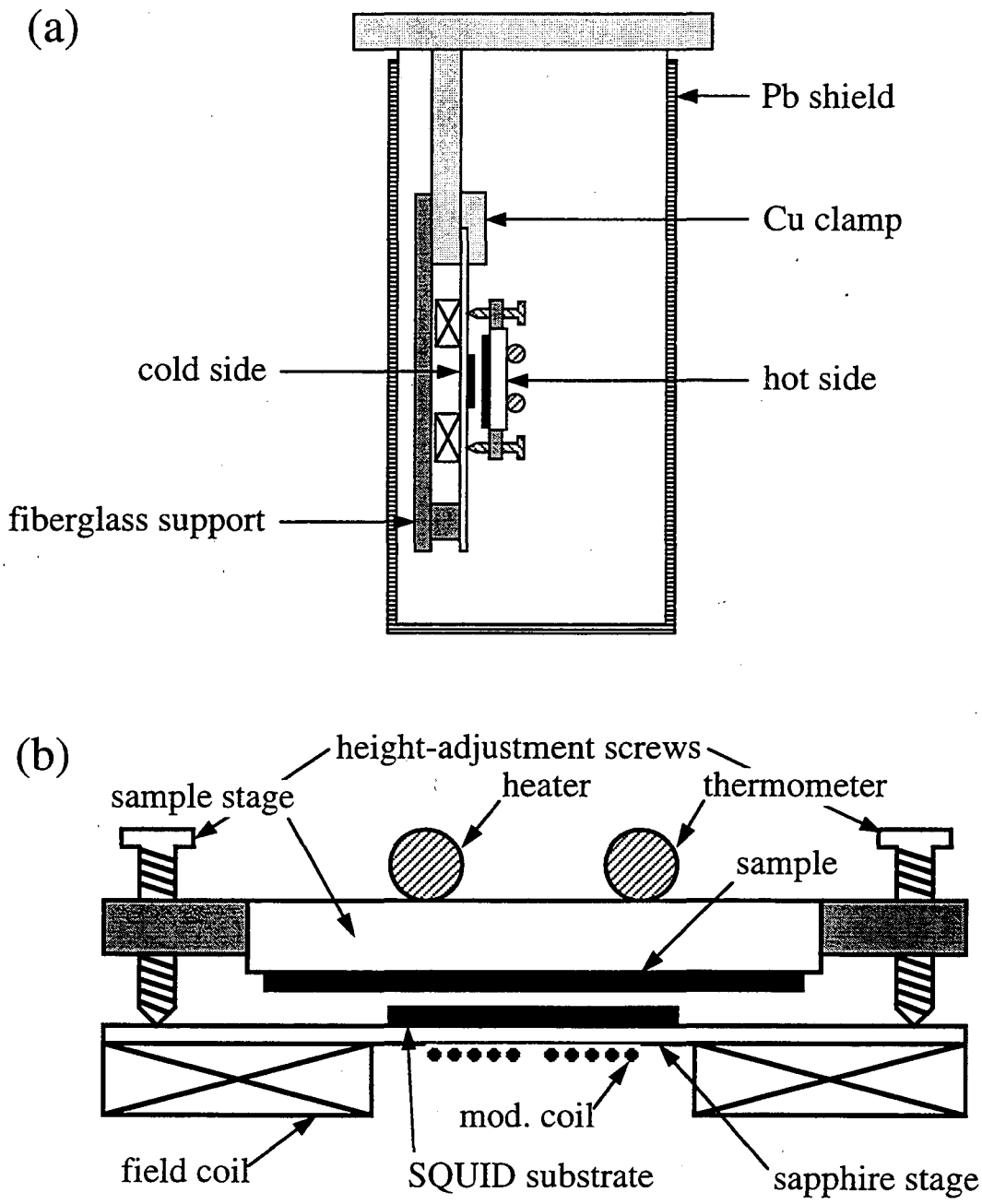

Figure 2.2: (a) Schematic drawing of cross section of vacuum can. (b) Magnified view of components of hot and cold sides.

2.1.2 SQUIDS and SQUID Electronics

The three types magnetic flux sensors used in the measurements are of the geometries shown schematically in Fig. 2.3. The first type of sensor, shown in Fig. 2.3(a) and labelled SQUID 1, is a conventional square-washer design[17]. For the measurements on YBCO, two SQUIDs of this type were used, one with inner diameter 200 μm and outer diameter 1 mm and another with inner diameter 26 μm and outer diameter 1 mm. For the measurements on Josephson junction arrays, three different SQUIDs were used. The first is a square-washer SQUID with inner diameter 180 μm and outer diameter 900 μm. The second sensor, shown in Fig. 2.3(b) and labelled SQUID 2, is a square pickup loop of width 250 μm. The leads extend approximately 1.5 mm and form a five-turn input coil which is coupled inductively to a square-washer SQUID as shown in the image in Fig. 2.4(a). The leads lie on top of each other so that when a sample is placed over the pickup loop only the loop picks up the perpendicular magnetic field. The third sensor, shown schematically in Fig. 2.3 and labelled SQUID 3, is very similar to SQUID 2 but the pickup loop has a diameter of 100 μm and is an extension of the SQUID body itself, as shown in the image in Fig. 2.4(b).

During measurements, the sample was placed directly over the sensor. The SQUIDs were operated in the standard flux-locked-loop mode at a modulation frequency of 100 kHz. Readers interested in the details can consult Ref. [17] and references therein, but a rough description will be given here. The general principle of of operation can be understood by first examining Figs. 2.5 and 2.6. In order operate the SQUID, the bias current and dc flux is adjusted as shown in Fig. 2.5 to give the largest signal from the SQUID. The voltage across the SQUID is a periodic function of the flux threading the SQUID, with period $\Phi_0 = hc/2e$, the superconducting flux quantum. A portion of the voltage-flux response is shown schematically in the top left curve of Fig. 2.6(a). In the flux-locked-loop mode, the ac flux is adjusted to have a peak-to-peak magnitude of $\Phi_0/2$. As shown in the lower left curve of Fig. 2.6(a), when the quasistatic flux, Φ_{qs} is an integer number of flux quanta, the resultant voltage across the SQUID will be at twice the 100 kHz reference frequency, shown in the right curve of Fig. 2.6(a). In this way, when the amplified signal is referenced to the 100 kHz modulation frequency by the mixer as shown in Fig. 2.5, the result will be zero. If Φ_{qs} is now set at $(N + 1/4)\Phi_0$, as shown in Fig. 2.6(b), the SQUID signal is at 100 kHz and will produce a maximum signal after being referenced to the modulation frequency. One can

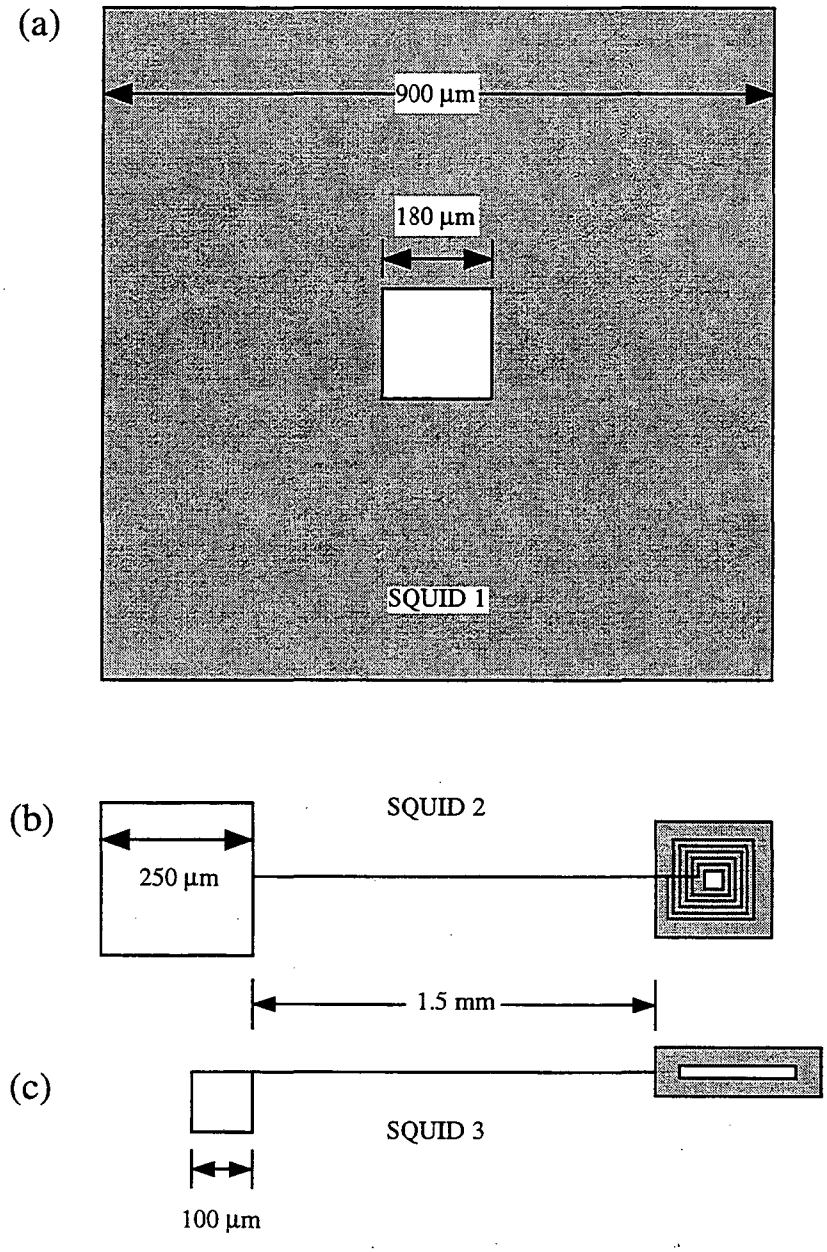

Figure 2.3: Schematic drawings of (a) SQUID 1, (b) SQUID 2, and (c) SQUID 3. See text for detailed descriptions.

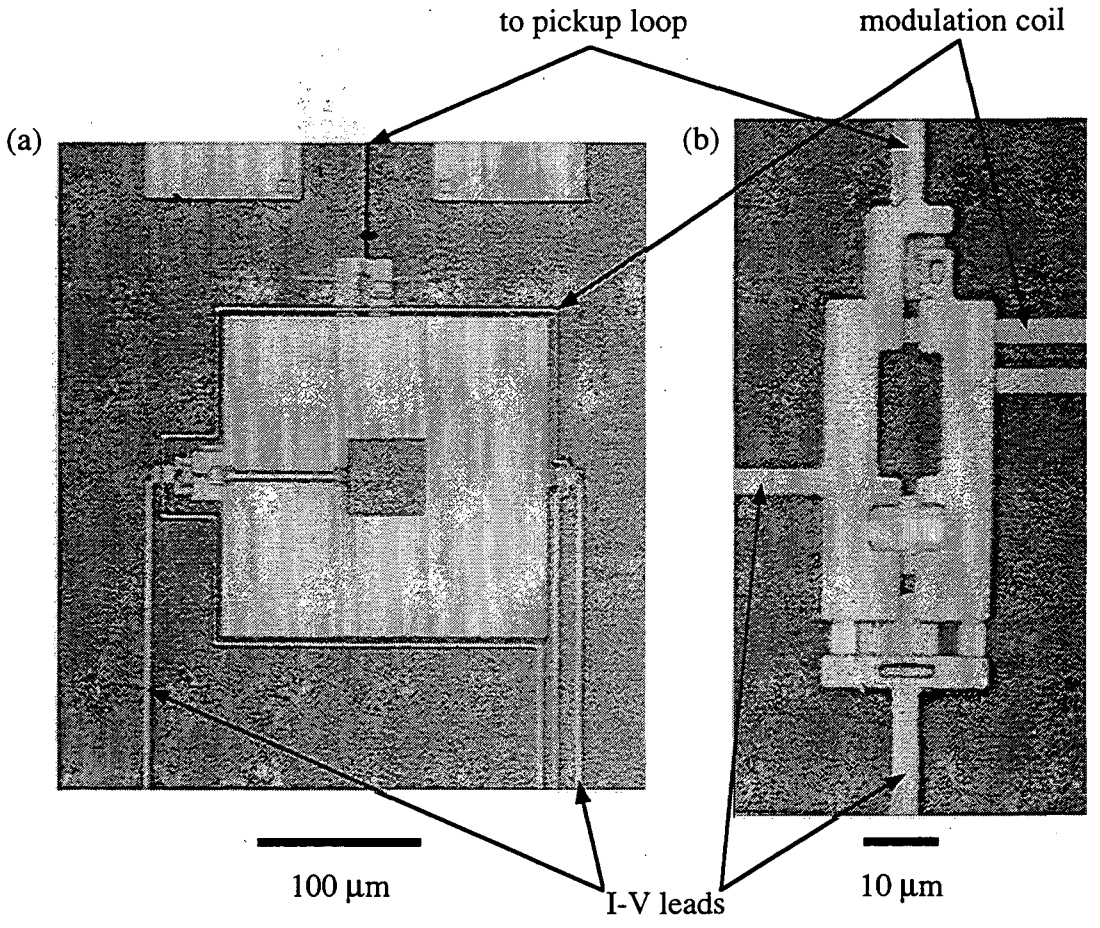

Figure 2.4: Image of (a) SQUID 2 and (b) SQUID 3

see that as the quasistatic flux is changed from $N\Phi_0$ to $(N + 1/4)\Phi_0$, the signal from the mixer will steadily increase, and similarly decrease as the quasistatic flux is changed from $N\Phi_0$ to $(N - 1/4)\Phi_0$. Therefore, when the signal output from the mixer is sent through an integrating amplifier and the feedback on switch in Fig. 2.5 is closed, the electronics will feed a current through the feedback resistor, R_f, which generates a flux through the SQUID via the mutual inductance M_f to null any changes in the quasistatic flux. In this way, the SQUID and electronics acts as a null detector of the flux through the SQUID.

This describes the general operation procedure of the flux-locked-loop, but two aspects which are not obvious from the description is the reason for the 100 kHz modulation and the necessity of the transformer to couple the SQUID signal to the preamplifier. A modulation frequency of $100 - 500$ kHz is used in order to overcome the $1/f$ noise in the preamplifier which typically extends up to $10 - 50$ kHz, and also to alleviate low frequency drift in the bias current and preamplifier. The transformer presents an impedance $N^2 R_d$ to the preamplifier, where N is the turns ratio of the transformer and R_d is the dynamic impedance of the SQUID, in order to optimize impedance matching between the SQUID and preamplifier and to amplify the SQUID noise to a level higher than that of the preamplifier.

The transformer used in the apparatus of Figs. 2.1 and 2.5 is a superconducting transformer consisting of a secondary coil with 750 turns of niobium wire wound around a teflon form, around which are wound 11 turns of lead tape, forming the primary coil. The transformer sits outside of the vacuum can as shown in Fig. 2.1, and was used instead of the apparatus' original tuned tank circuit because it provides a larger frequency bandwidth. A small blocking resistor, R_b, prevents all of the SQUID bias current from being shunted through the primary coil of the transformer. A tunable room temperature capacitor is used to adjust the resonant frequency of the transformer to 100 kHz with a small $Q \approx 2$.

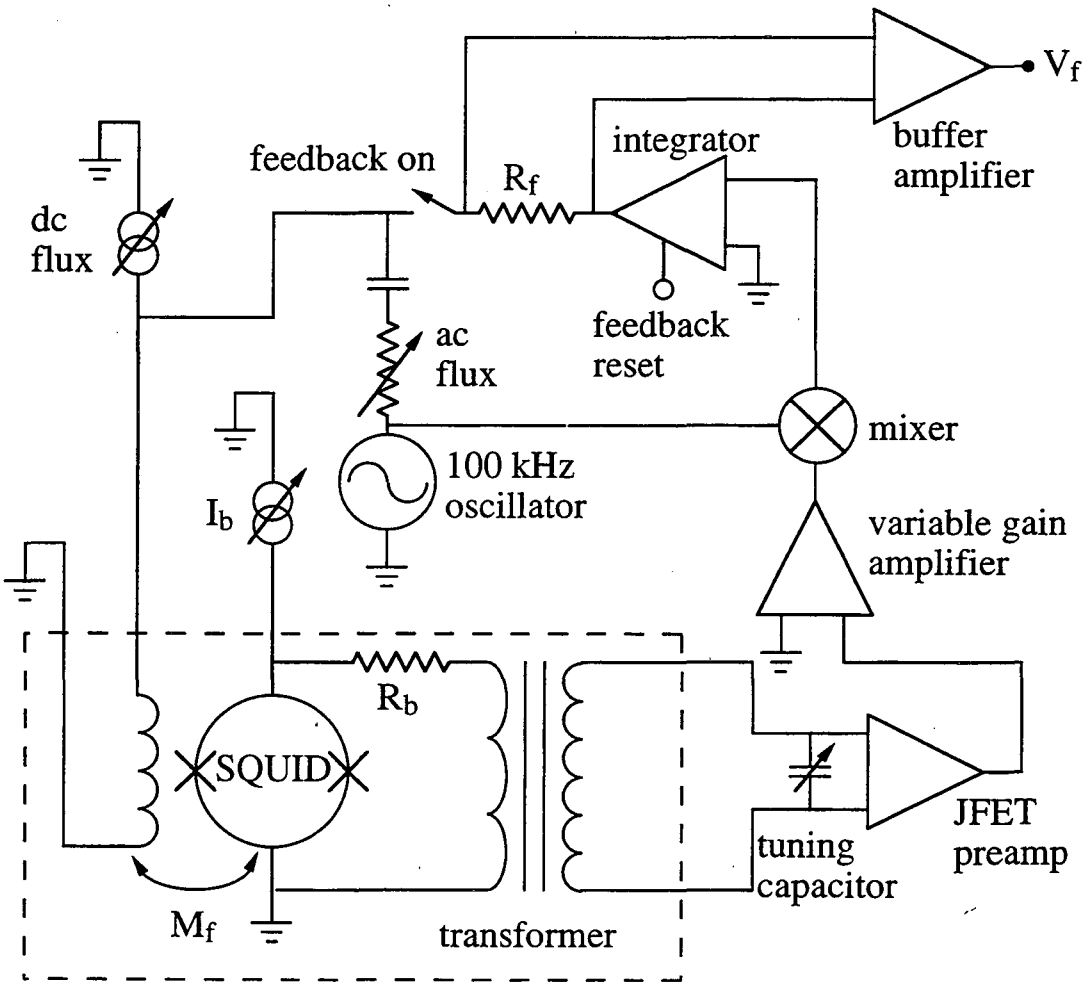

Figure 2.5: Schematic of electronics used to operate SQUID.

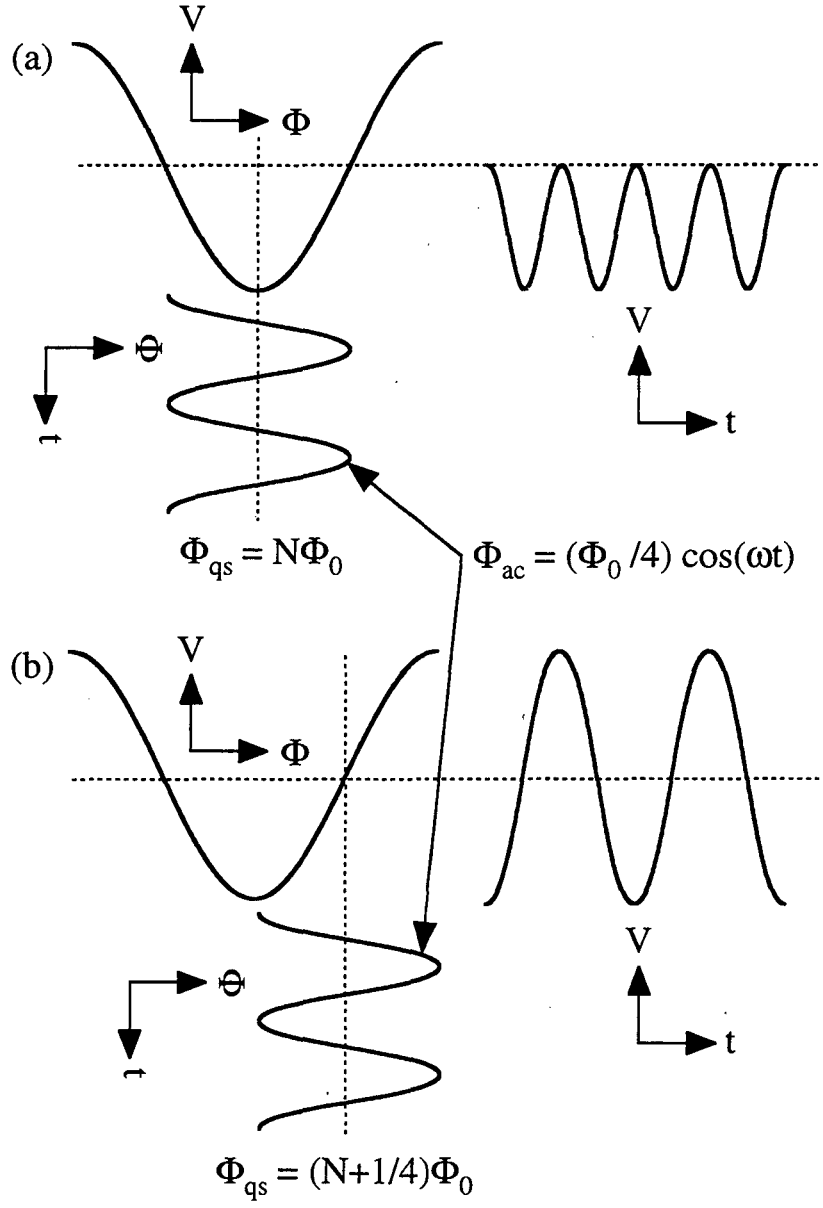

Figure 2.6: Flux modulation scheme for SQUID with (a) $\Phi_{qs} = N\Phi_0$ and (b) $\Phi_{qs} = (N + 1/4)\Phi_0$.

2.1.3 Measurement Procedure

The general flux noise measurement procedure was to first adjust the current to the resistive heater of the hot side and wait for the temperature to stabilize. Next, the SQUID bias current and alternating flux modulation were optimized as described in Section 2.1.2. Then, the feedback on switch was closed to begin the flux-locked-loop mode (see Fig. 2.5 for visualization of the procedures discussed here), and the conversion factor between flux through the SQUID and output buffer voltage, R_f/M_f (see Fig. 2.5), was determined. The standard procedure for determining R_f/M_f was to manually increase the static flux input and then reset the integrator. This caused the lock point of the feedback loop to jump by an integer number of flux quanta through the SQUID (chosen to be $\pm 1\Phi_0$ by judicious adjustment of the static flux), and the resultant change in V_f gave R_f/M_f, or equivalently the current needed to produce a flux change of Φ_0 through the SQUID.

In order to measure the power spectral density of flux noise, $S_\Phi(\omega)$, the buffer voltage, V_f, was fed to a spectrum analyzer. The spectrum analyzer bandwidth was then set and 50 to 1000 averages were taken, depending on the measurement bandwidth, followed by a dump of the resultant spectra to a computer.

In addition to the flux noise measurements, for the measurements on Josephson junction arrays it was necessary to make electrical measurements, namely the differential resistance, dV/dI, as a function of static bias current and temperature. A measurement schematic is shown in Fig. 2.7. An alternating current at a frequency of 47 Hz was fed into the array via a function generator to provide an rms current of 10 μA. The voltage leads to the array were coupled to a PAR 190 transformer, with a gain of 100, and the resultant voltage was fed to a lock-in amplifier. The temperature dependence of dV/dI, at zero static bias, was measured by adjusting the current to the resistive heater (see Fig. 2.2), waiting for temperature to stabilize, and then recording the lock-in output. In order to measure dV/dI as a function of static bias current, at fixed temperature, the ac current was set as described as above and a computer running LABView^{TM} stepped up the bias current while recording the output from the lock-in.

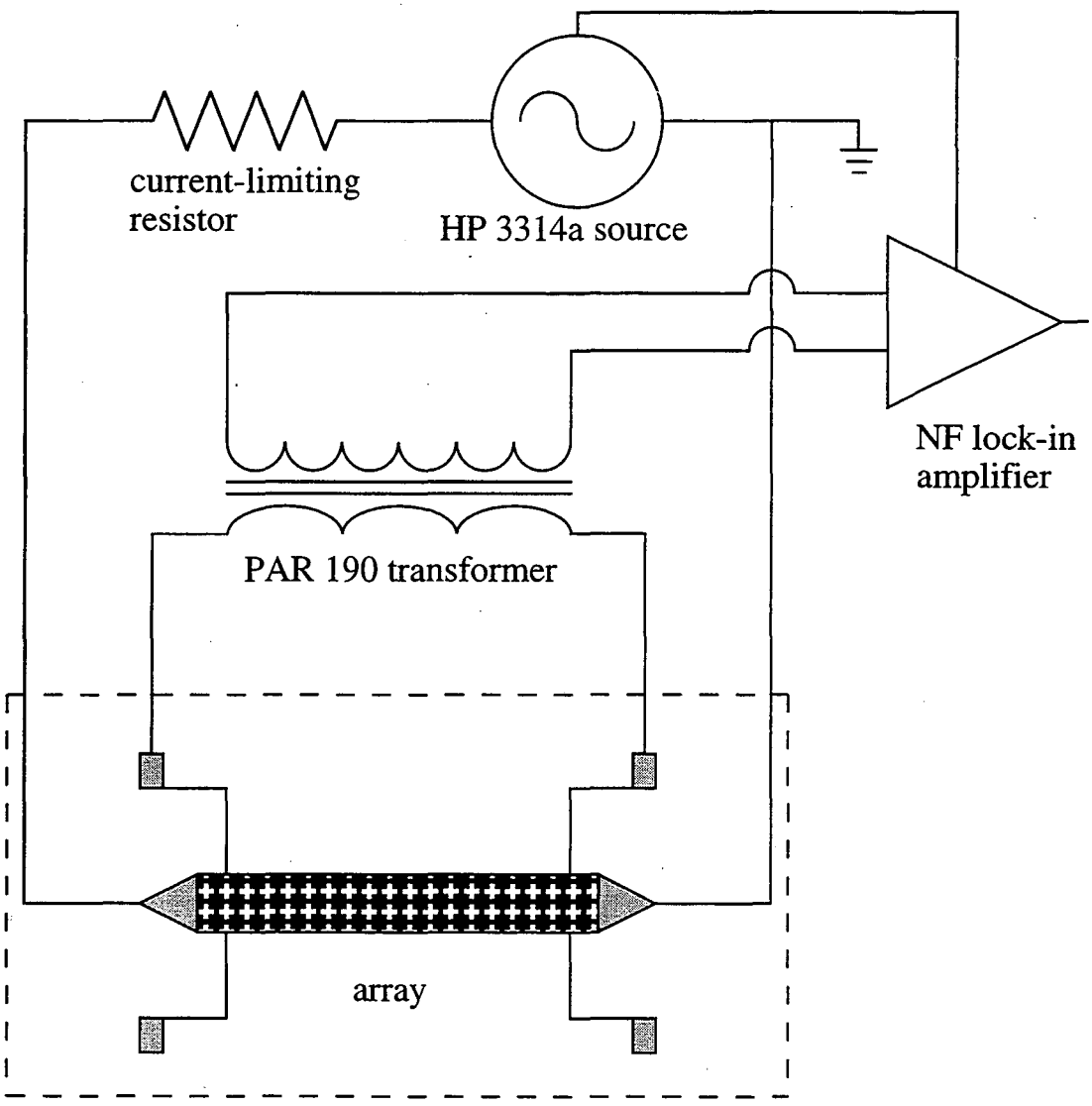

Figure 2.7: Scheme for electrical measurements of arrays.

2.2 Samples

The two crystals of $YBa_2Cu_3O_{7-x}$ (YBCO) were grown by Alice White from a partially melted $BaCuO_2$-CuO based mixture[18], and have approximate dimensions of 1 mm $\times$ 1 mm $\times$ 30 μm, with the c-axis along the smallest dimension. One crystal was irradiated with 3.1 MeV protons at a fluence of 3×10^{20} m^{-2}, which has been shown[19] to produce the optimal enhancement of J_c by introducing a large number of small ($\approx$ 2 nm diameter) defects approximately 2 nm apart[20]. The second crystal was irradiated with 1 GeV Au ions at a fluence of 4.8×10^{14} m^{-2}, which produces columnar defects through the sample of average diameter $\sim$ 5 nm with an average separation of about 50 nm[21, 22]. The samples will be referred to as: P1 and P2, proton irradiated sample before and after irradiation; I1 and I2, heavy ion irradiated sample before and after irradiation.

The Josephson junction arrays [23] consist of 0.2 μm-thick niobium islands on top of a 0.3 μm-thick copper film. The islands form an array of SNS Josephson junctions of width 4 μm and length 2 μm. In order to determine the effects of lattice geometry and critical current on the measured flux noise, three different arrays were studied: one of a triangular-lattice geometry [Fig. 2.8(a)] with a lattice constant of 14 μm, which will be denoted as array A, and two of a square-lattice geometry [Fig. 2.8(b)] with a lattice constant of 10 μm, which will be denoted as array B and array C. Array A is 3mm wide and 10 mm long, corresponding to 217 $\times$ 625 junctions, array B is 1 mm wide and 10 mm long, corresponding to 100 $\times$ 1000 junctions, and array C is 1 mm wide and 10 mm long, corresponding to 140 $\times$ 1400 junctions (the lattice of array C is rotated 45 degrees in comparison to the lattice of array B).

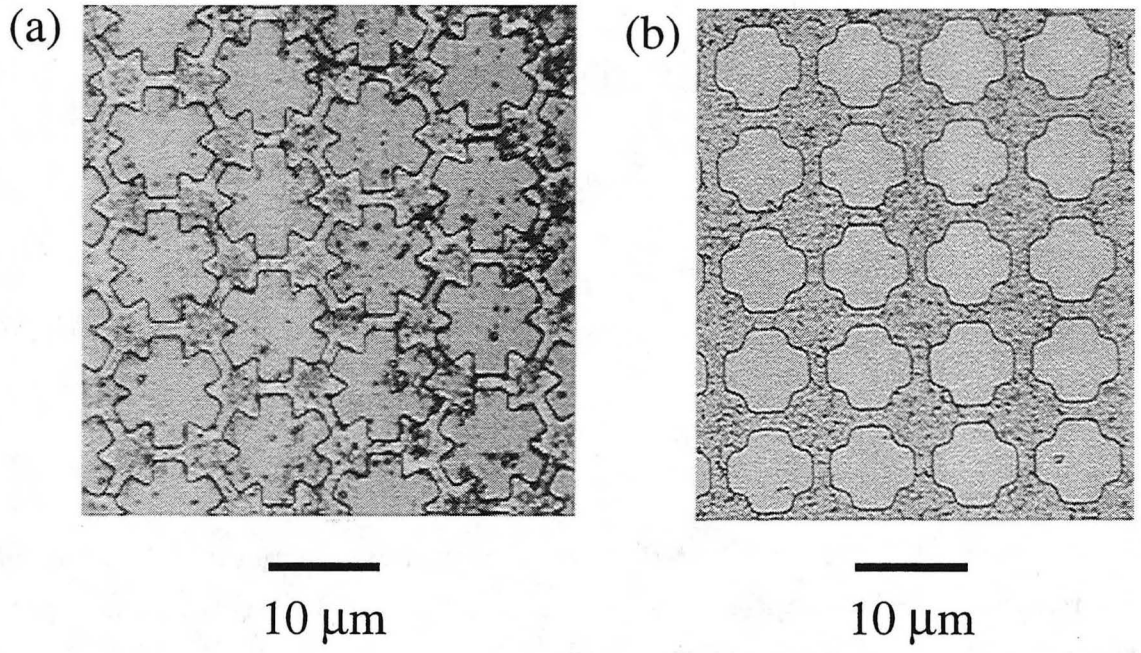

Figure 2.8: Images of small sections of (a) array A and (b) array B.

Chapter 3

Effects of 3.1 MeV Proton and 1 GeV Au Ion Irradiation on the Magnetic Flux Noise and Critical Current of $Y_1Ba_2Cu_3O_{7-\delta}$

3.1 Introduction

For both fundamental and technological reasons, vortex motion in high-temperature superconductors (HTSCs) has been intensely studied since the discovery of these materials. When a HTSC is cooled through its transition temperature, T_c, in the presence of a magnetic field, the magnetic field penetrates the sample in the form of vortices, each containing a single flux quantum, Φ_0. Even in the absence of a field, vortex-antivortex pairs and vortex rings have a sufficiently small energy of formation that they are spontaneously created near T_c. The vortices can be pinned at defects, which provide regions of reduced superconductivity. Defects in as-grown materials often vary appreciably from sample to sample, and currently there is no consensus as to the types of defects which are largely responsible for vortex pinning[24, 25]. From a fundamental viewpoint, understanding vortex motion is essential for determining the properties of pinning sites. From a technological viewpoint, it is vitally important to develop materials which effectively restrict vortex motion, since thermal fluctuations and applied currents can cause vortices to move. Vortex motion produces

dissipation and noise—both highly detrimental to the performance of HTSC devices. Dissipation limits the critical current of wires and tapes used to carry large currents, for example, in superconducting magnets, and low frequency noise can severely limit the magnetic field sensitivity of Superconducting Quantum Interference Devices (SQUIDs).

In order to study the effects of a known type of defect, and also in attempts to make HTSCs with higher critical current densities, J_c, many groups have introduced artificial defects through irradiation with high energy particles, namely protons, neutrons, and heavy ions[24]. Most of the experimental studies have used techniques such as ac and dc magnetization, flux creep, and current-voltage measurement to determine the effects of irradiation on J_c, pinning energies, and pinning forces[25]. Usually, these studies involve large magnetic fields (>0.1 T) and large current densities ($\sim J_c$). In the presence of large magnetic fields and currents, the vortices interact strongly and their motion is determined by the largest available pinning energies and forces. In contrast, in the presence of small magnetic fields and currents the interaction between vortices is negligible and their motion is determined by thermal activation between pinning sites. In order to investigate the link between between these two regimes, and also with the hope of finding a method to reduce flux noise in SQUIDs, we undertook a study of the effects of irradiation on the flux noise and critical current of the two YBCO samples described in Section 2.2. Crystals were chosen instead of the more technologically important thin films because as-made crystals have a much lower density of defects, and therefore a larger effect due to irradiation was expected.

3.2 Critical Currents

Figure 3.1 shows J_c of both samples before and after irradiation, determined with a vibrating-sample magnetometer at a frequency of 84 Hz with field sweep rates of 20–40 mT/s. Within a factor of two, the critical currents are identical in samples P1 and I1, at a given temperature and field, at all temperatures and fields studied. The same is true in samples P2 and I2, demonstrating that both proton and ion irradiation with the fluences given above produced nearly identical increases in J_c. This temperature- and field-dependent increase in J_c ranged from factors of 2–30. In this regime of large magnetic fields and currents, the two relevant sample-dependent factors determining J_c are the pinning force of an individual defect and the density of defects[26]. Since the defect structure, and hence the pinning force, created by a given type of irradiation are much more difficult to control than the

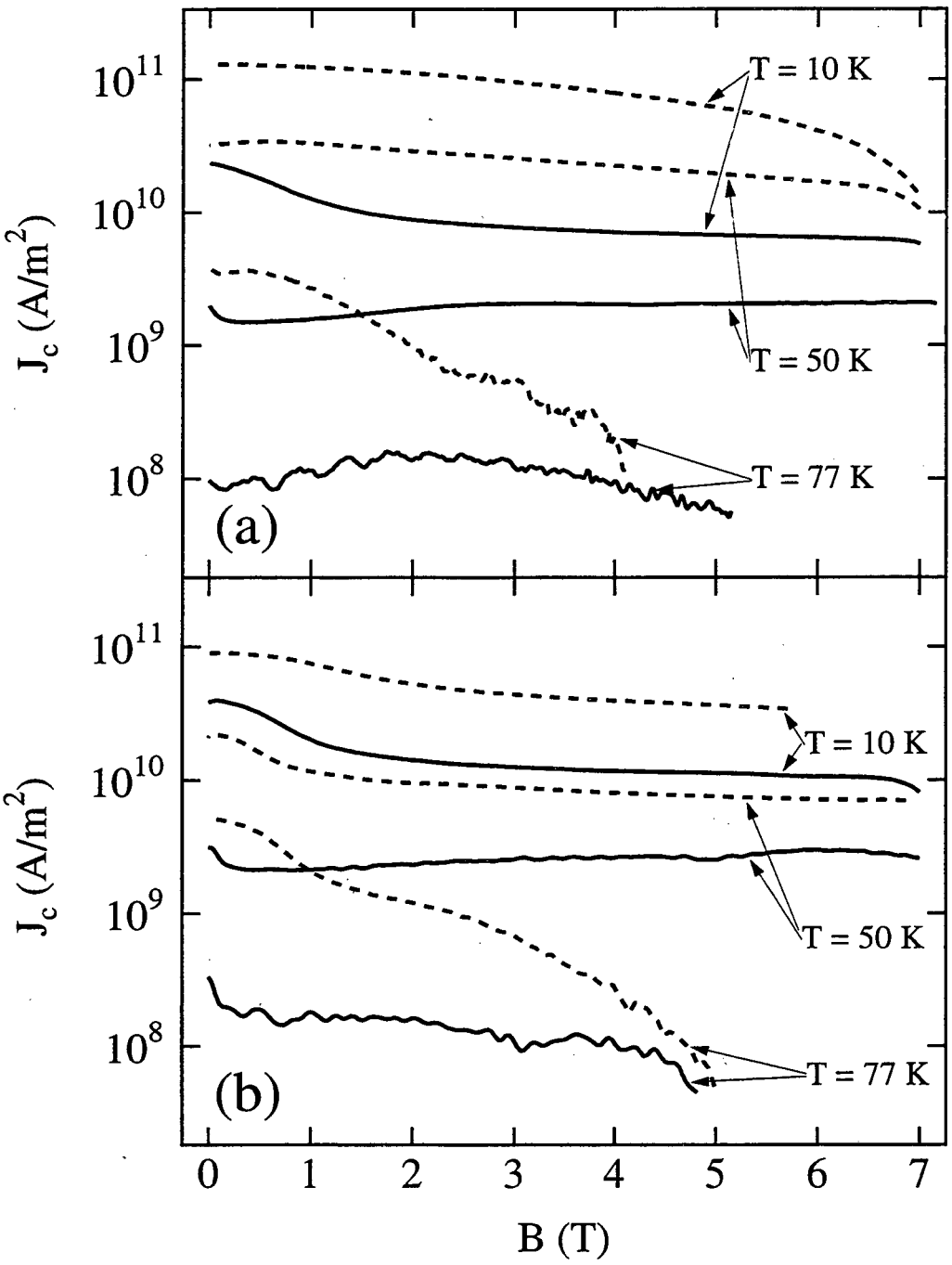

Figure 3.1: J_c versus B for (a) P1 (solid line), P2 (dotted line) and (b) I1 (solid line), I2 (dotted line).

density of defects, one aims to create the largest possible defect density without degrading the superconductivity in too large a fraction of the sample. In order to check the damage done by the irradiation, we determined T_c of both samples by measuring the static magnetic shielding with a dc SQUID (see Sec. 3.3). The proton irradiation reduced T_c from 90.0 K to 86.5 K and the ion irradiation reduced T_c from 89.5 K to 89.0 K, indicating that irradiation had not destroyed the superconductivity in a large fraction of either sample. As is evident from Fig. 3.1, these large densities of defects proved to be effective in decreasing vortex motion, and hence in increasing J_c, in good agreement with earlier studies[25, 19, 20].

3.3 Magnetic Flux Noise

3.3.1 Measurement of Vortex Motion in Equilibrium

In contrast to applications involving large magnetic fields and currents, where the density and pinning *force* of defects is important, for HTSC SQUID magnetometers one aims to restrict vortex motion and hence reduce the low frequency magnetic field noise in the presence of small magnetic fields and currents. In this regime, since the density of vortices is low and vortex motion is determined by thermal activation, it is important to create defects with the largest possible pinning *energies*. Of course, for operation of SQUIDs in the earth's magnetic field, the density of defects should be greater than the density of vortices created. Since a field of 100 μT creates 5×10^{10} vortices/m^2, the defect density produced by the irradiation described in Sec. 3.2 is much larger than the vortex density present in the measurements described below. To our knowledge, there have been no previous studies of the effects of irradiation in reducing vortex motion in the presence of small magnetic fields and currents.

In order to study the effects of irradiation in the small field regime (<2 mT), we measured the noise generated by the motion of vortices in thermal equilibrium[16] (that is, with no applied current) in the same samples for which we determined J_c. Two different SQUIDs were used, both of the square washer design shown schematically in Fig. 2.3, with inner and outer dimensions of 200 μm and 1 mm (sample P1) and 26 μm and 1 mm (samples P2, I1, and I2). The superconducting persistent current coil shown in Fig. 2.2 was used to apply a magnetic field, B, parallel to the c-axis of the sample. Our procedure was to raise the temperature of the sample above T_c, store a field in the coil, cool the sample to the

desired temperature, and measure the spectral density of magnetic flux noise, $S_\Phi(\omega)$.

3.3.2 Magnetic Field Dependence: Data and Qualitative Explanation

We first determined the effects of irradiation on the magnetic field dependence of $S_\Phi(\omega)$. Figure 3.2 shows $S_\Phi(1\text{ Hz})$ at $T = 75$ K of both samples before and after irradiation. The data at $|B| = 1$ μT were taken at zero *applied* field, so that the ambient field was ≤ 1 μT. Open and closed symbols correspond to opposite signs of the applied field (except for the points at 1 μT), showing that the direction had no effect. Over the entire field range, both types of irradiation reduced $S_\Phi(1\text{ Hz})$. At $|B| = 50$ μT, $S_\Phi(1\text{ Hz})$ of P2 was roughly 100 times smaller than that of P1. In contrast, at the same field, $S_\Phi(1\text{ Hz})$ of I2 was reduced by a factor of only 3 compared with that of I1. In addition, the data show two different types of field dependence. For both samples P2 and I2, $S_\Phi(1\text{ Hz})$ is approximately linear in $|B|$ above a threshold value, and flattens off at smaller fields. For P1, $S_\Phi(1\text{ Hz})$ increases linearly with $|B|$ over the entire field range, but for I1 we do not have sufficient data to determine if $S_\Phi(1\text{ Hz})$ flattens off at low fields.

Qualitatively, we understand the two types of field dependence of $S_\Phi(1\text{ Hz})$ as follows. When the sample is field-cooled through T_c, there are two sources of vortex formation, thermal fluctuations and the magnetic field. The field produces a density of vortices proportional to $|B|$ and of the same sign. In addition, near T_c, the energy needed to create vortex-antivortex pairs and vortex rings is smaller than k_BT. Many of these pairs and rings annihilate as the sample cools, but some become pinned. Therefore, at small enough fields the density of thermally created vortices is larger than the density of field-created vortices and the noise is independent of field. At higher fields, the number of field created vortices dominates and the noise increases with $|B|$.

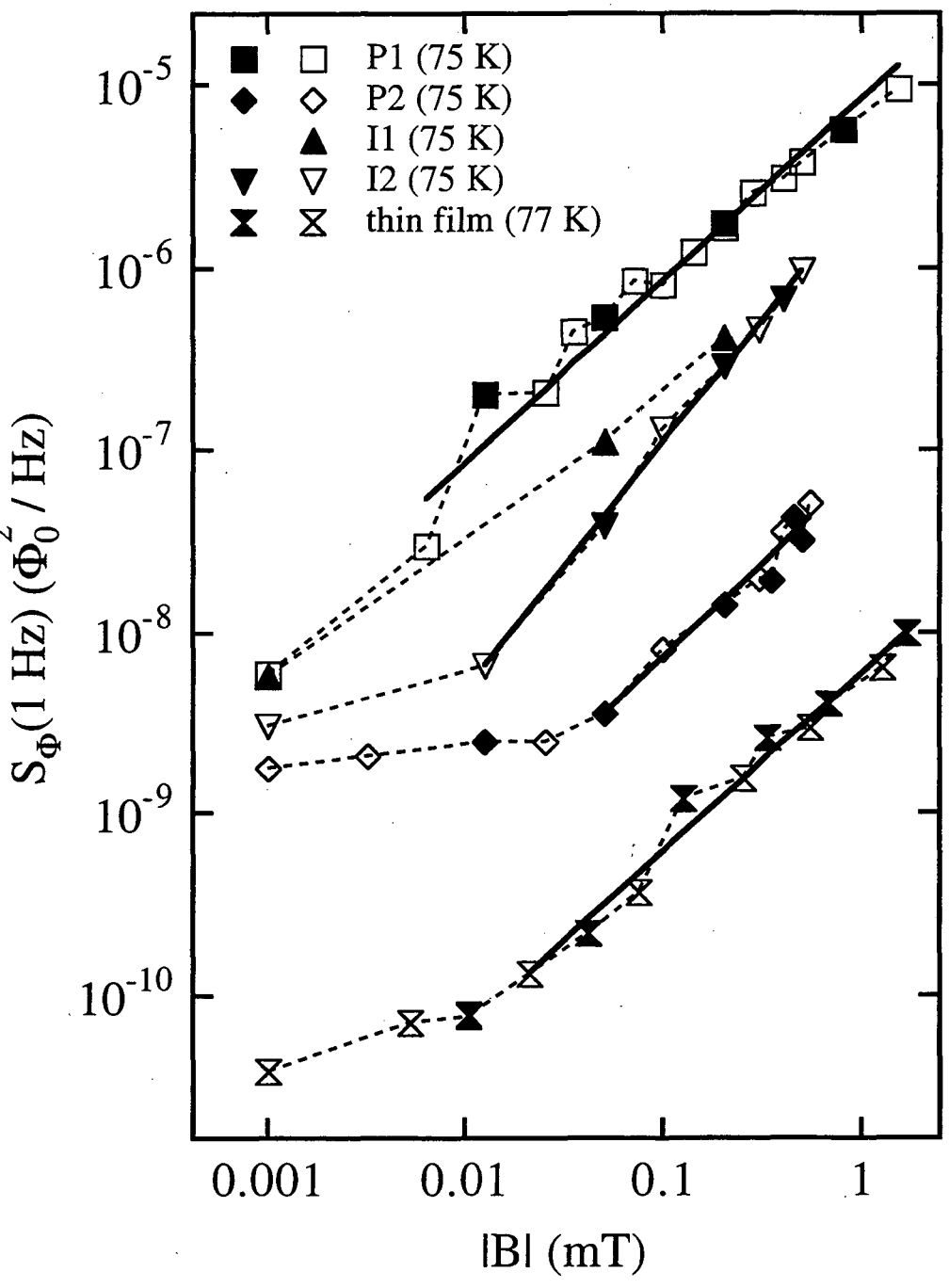

Figure 3.2: $S_\Phi(1\ \mathrm{Hz}, B)$ versus $|B|$ for P1, P2, I1, and I2 at $T = 75$ K and for YBCO thin film at $T = 77$ K. Points shown at 1 μT should be interpreted as taken at $|B| \leq 1$ μT. Open and closed symbols are for opposite signs of B (except at 1 μT). Dotted lines are to guide the eye, solid lines are fits in the linear regime.

3.3.3 Dutta-Dimon-Horn Model

In order to analyze the data quantitatively, we use our extension of the Dutta-Dimon-Horn (DDH) model[16, 27]. In this model, each vortex is confined to a double well potential, that we assume to be symmetric, as shown inset in Fig. 3.3(a). Evidence for the validity of this model has been previously reported[16], and the main point is that at the temperatures at which the noise measurements are made the only vortices which contribute to the flux noise in the measurement bandwidth have relatively small activation energies and are pinned in areas with two relatively closely spaced defects. Within the model, we can immediately identify the important difference between critical current measurements, which are sensitive to pinning *forces*, and noise measurements, which are sensitive to pinning *energies*. The pinning force is proportional to the curvature of the pinning potential whereas the pinning energy is given by the height of the barrier, $U(T)$, between each well as shown in Fig. 3.3(a). If we assume that the wells are parabolic, a vortex hopping from one side to the other moves a distance

$$\ell = CU^{1/2}(T), \tag{3.1}$$

where C is a constant and $U(T)$ is the temperature dependent activation energy.

We assume a temperature dependent activation energy since most pinning interactions for isolated vortices [14] yield pinning energies proportional the the vortex self-energy[28],

$$\varepsilon \propto 1/\lambda^2(T) \propto 1 - (T/T_c)^4, \tag{3.2}$$

where $\lambda(T)$ is the penetration depth, and we take

$$U(T) = U_0[1 - (T/T_c)^4], \tag{3.3}$$

where U_0 is the zero temperature activation energy.

Given the relation [Eq. (3.1)] between the hopping length and the energy barrier height, we next assume the flux coupled through the SQUID decreases linearly from Φ_0 to zero as the vortex moves radially between the inner and outer edges of the washer[16]. In fact, the coupling coefficient between the SQUID and sample is not unity, typically varying between 0.5 and 1, but our simplifying assumption of perfect coupling does not materially affect our conclusions. Therefore, a vortex hopping a distance ℓ at an angle θ with respect

to the radial direction produces a change

$$\Delta\Phi = \Phi_0(\ell/w)\cos\theta \tag{3.4}$$

in the flux threading the SQUID, where w is the width of the SQUID washer. Thermal activation of the vortex between the two wells produces a Lorentzian power spectrum[29]

$$S_\Phi(\omega, T) = (\Delta\Phi)^2\tau/\left[1 + (\omega\tau)^2\right], \tag{3.5}$$

where

$$\tau = \quad \tau_0 \exp\left[U_0\beta(T)\right], \tag{3.6}$$

$$\beta(T) \equiv \quad U(T)/U_0 k_B T = \left[1 - (T/T_c)^4\right]/k_B T, \tag{3.7}$$

and τ_0^{-1} is the attempt frequency. For an ensemble of independent vortices, the total noise power spectrum is the sum of the individual spectra in Eq. (3.5). We assume that there is a distribution of zero temperature activation energies, $D(U_0)$, or equivalently a distribution of hopping distances, so that $D(U_0)dU_0$ represents the number of occupied double wells with zero temperature activation energies between U_0 and $U_0 + dU_0$. If the noise processes are incoherent and randomly distributed over the angle θ, the total flux noise power spectrum is

$$S_\Phi(\omega, T, B) = \frac{1}{2}\int_0^\infty dU_0 D(U_0)\frac{(\Delta\Phi)^2\tau}{1 + (\omega\tau)^2}. \tag{3.8}$$

The kernel of Eq. (3.8) is sharply peaked at an energy

$$\widetilde{U}_0(\omega, T) = \ln(1/\omega\tau_0)/\beta(T). \tag{3.9}$$

Assuming that $D(U_0)$ varies slowly over the width, $1/\beta(T)$, of the kernel, we can take $D(\widetilde{U}_0(\omega, T), B)$ outside the integral in Eq. (3.8), carry out the integration, and substitute for $\Delta\Phi$, τ, $\beta(T)$, and $\widetilde{U}_0(\omega, T)$ using Eqs. (3.4), (3.6), (3.7), and (3.9) to find

$$D(\widetilde{U}_0(\omega, T), B) = \left[\frac{w^2}{\pi \ln(1/\omega\tau_0)}\right]\left[\frac{\beta(T)}{C\Phi_0}\right]^2 \omega S_\Phi(\omega, T, B). \tag{3.10}$$

From Eq. (3.10), we see quantitatively that $S_\Phi(\omega, T, B)$is directly proportional to $D(\widetilde{U}_0(1\text{ Hz}, 75\text{ K}), B)$. Since $D(\widetilde{U}_0(1\text{ Hz}, 75\text{ K}), B)$ is also proportional to $\beta^2(T)$, we restricted the temperature regions over which we measured $S_\Phi(\omega, T, B)$ to temperatures far enough below T_c to ensure that the difference between the measured temperature dependence[30]

of $\lambda(T)$ and the two-fluid result assumed in Eq. (3.2) would not affect our conclusions. Therefore, by measuring $S_\Phi(\omega, T, B)$ we can extract the distribution of pinning energies and its dependence on $\omega, T,$ and B. Since $S_\Phi(\omega) \propto 1/\omega^\alpha$, where $\alpha \approx 1$[16], at all temperatures and fields for the data described in this paper, the distribution of activation energies is nearly frequency independent. We therefore concentrate on the field and temperature dependence of $D(\widetilde{U}_0(\omega, T), B)$.

3.3.4 Magnetic Field Dependence: Quantitative Explanation

The linear field dependence of $S_\Phi(1\text{ Hz})$ in Fig. 3.2 is explained by the intuitive notion that the number of active vortices is proportional to the applied field provided there are more field-created than thermally created vortices. In addition, there must be more equivalent pinning sites than vortices. These pinning sites become populated with increasing field. At low fields, the flattening of $S_\Phi(1\text{ Hz})$ indicates that the number of active vortices is determined by vortices created and pinned as the sample is cooled below T_c.

Even though the field dependence is well described by Eq. (3.10), Fig. 3.2 shows that there is a large sample-to-sample variation. Since the total number of vortices at a given field, in the linear field dependence regime, is identical in each sample, we must account for this variation. Evidently, at least one of the parameters τ_0, $\beta(T)$, C, or $D(\widetilde{U}_0)$ must be sample dependent. It is very unlikely that the substantial variation can be explained by different values of τ_0 since $S_\Phi(\omega)$ is a logarithmic function of τ_0, which ranges typically from 10^{-11} to 10^{-13}s[31, 32, 33]. For example, if we were to take $\tau_0 = 10^{-11}$s for sample P1, Eq. (3.10) would require that $\tau_0 \approx 0.1$ s in sample P2 to account for the 100-fold difference in the noise power in the linear field dependence regime. It is also unlikely that the variation can be explained by different pinning mechanisms since $\beta(T) \propto 1/\lambda^2(T)$ and $\lambda(T)$ should be relatively sample-independent this far below T_c. Even the small factor of 4 difference in $S_\Phi(1\text{ Hz})$ at $T = 75$ K and $B = 50$ μT between P1 and I1, nominally identical samples, would require a factor of 2 different in $\lambda(75\text{ K})$. The third possibility is that C varies from sample to sample. From Eq. (3.1) we see that $1/C^2$ is proportional to the curvature of an individual well. It is possible that different curvatures could explain the smaller differences between $S_\Phi(1\text{ Hz})$ of samples P1, I1, and I2, but is inconceivable that this could vary by the factor of 100 necessary to account for the factor of 100 difference in the noise power of P1 and P2 in the linear field dependence regime. Since different values of τ_0, $\beta(T)$, or C seem most unlikely to explain the noise variation, we assume that τ_0 and C are sample independent constants and use the form of $\beta(T)$ given in Eq. (3.7). We are thus led to the conclusion that the change in $S_\Phi(1\text{ Hz})$ arises from changes in $D(\widetilde{U}_0)$.

3.3.5 Extracting $D(\widetilde{U}_0)$

We now explore which pinning sites the vortices occupy, that is, the dependence of $D(\widetilde{U}_0)$ on $\widetilde{U}_0$. Since $D(\widetilde{U}_0)$ varies only logarithmically with τ_0 [Eq. (3.10)] and typical values of τ_0 range from 10^{-11} to 10^{-13}s, we take $\tau_0 = 10^{-11}$s so that Eq. (3.9) yields $\widetilde{U}_0 \approx 23k_BT[1-(T/T_c)^4]^{-1}$. Therefore, by measuring $S_\Phi(1\text{ Hz})$ versus T, we map out the number of active vortices over the energy interval corresponding to that temperature interval. In order to study this dependence, we have measured $S_\Phi(1\text{ Hz})$ versus T for samples P1, P2, I1, and I2 at $B = +200\ \mu\text{T}, -160\ \mu\text{T}, -160\ \mu\text{T}$, and $+100\ \mu\text{T}$ respectively. To make a comparison, we scaled $S_\Phi(1\text{ Hz})$ to $|B| = 100\ \mu\text{T}$ using the linear field dependence in this regime (see Fig. 3.2). Figures 3.3(a)–(d) show $S_\Phi(1\text{ Hz})$ versus T for P1 and I1, P2 and I2, P1 and P2, and I1 and I2 respectively. The lines through the data are cubic spline fits, and the maximum temperatures represented, corresponding to $\widetilde{U}_0 = 0.6$ eV, are 82.9 K, 80.0 K, 82.5 K, 82.1 K for samples P1, P2, I1, and I2 respectively. Figure 3.3(a) shows that the two nominally identical as-prepared crystals exhibit very different flux noise over almost the entire temperature range, reflecting the fact that low frequency $1/\omega$ noise in HTSCs is very sample dependent as noted in previous measurements[16], in contrast to the nearly identical values of J_c described in Sec. 3.2. The noise of the irradiated samples shown in Fig. 3.3(b) are comparable below $T \approx 45$ K whereas at higher temperatures I2 exhibits considerably higher noise than P2. A comparison of each crystal before and after irradiation in Figs. 3.3(c) and (d) shows that the proton irradiation produced a substantial noise reduction over the entire temperature range, except at $T = 4.2$ K, whereas the ion irradiation produced a reduction only between $T \approx 45$ K and 75 K. Indeed, below about 25 K the irradiation with ions increased the noise.

We can gain a better understanding of this behavior by examining the distribution of activation energies extracted from the noise data of Fig. 3.3. Figure 3.4(a) shows $C^2D(\widetilde{U}_0)$ versus $\widetilde{U}_0$ for all four samples, calculated using Eqs. (3.7) and (3.10), and the cubic spline fits to the data shown in Fig. 3.3. Figure 3.4(b) shows the same information for P2 and I2 with an expanded vertical axis to make the features more visible. We have adjusted the anchor points of the spline fits within the error bars to minimize artificial features in $C^2D(\widetilde{U}_0)$ introduced by scatter in the data.

There are two important features visible in Fig. 3.4. The first is that samples P1 and I1 both show peaks in $C^2D(\widetilde{U}_0)$ near $\widetilde{U}_0 = 0.1$ eV and 0.2 eV, whereas samples P2

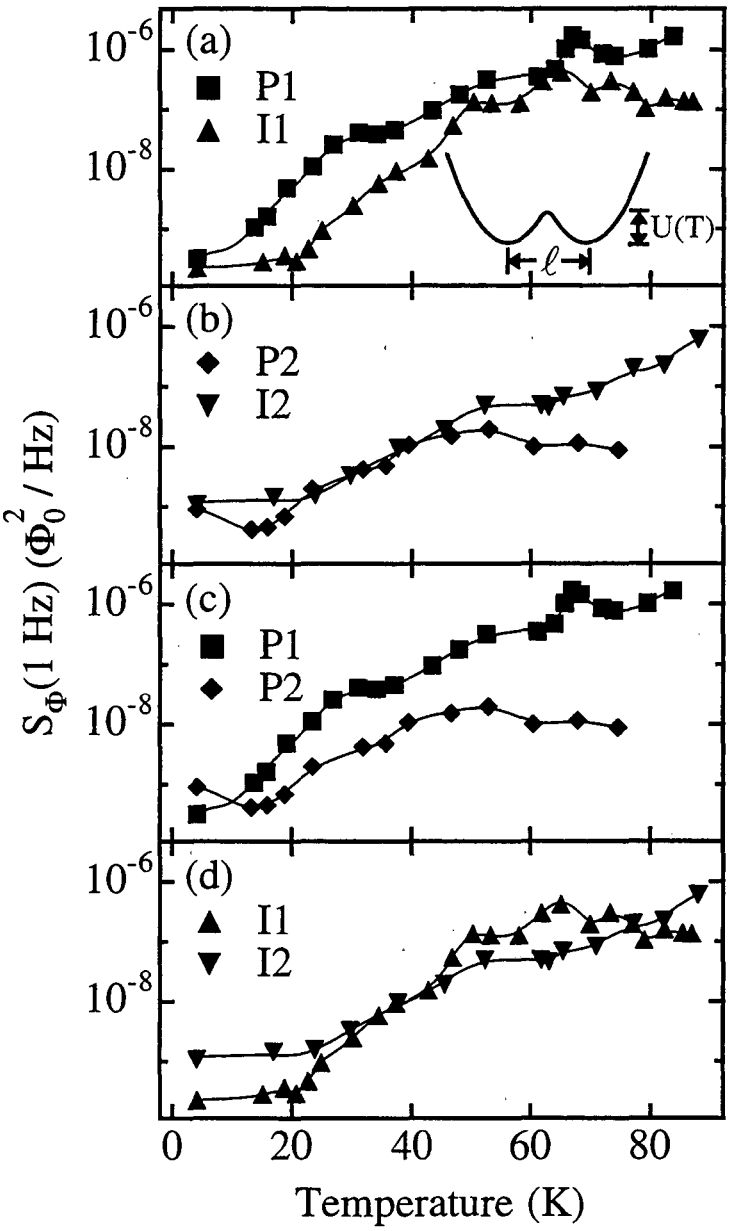

Figure 3.3: $S_\Phi(1\ \mathrm{Hz})$ at $|B| = 100\ \mu\mathrm{T}$ for (a) P1 and I1, (b) P2 and I2, (c) P1 and P2, (d) I1 and I2. Solid lines are cubic spline fits to the data. Inset shows double-well pinning site with energy barrier $U(T)$ between minima of separation ℓ.

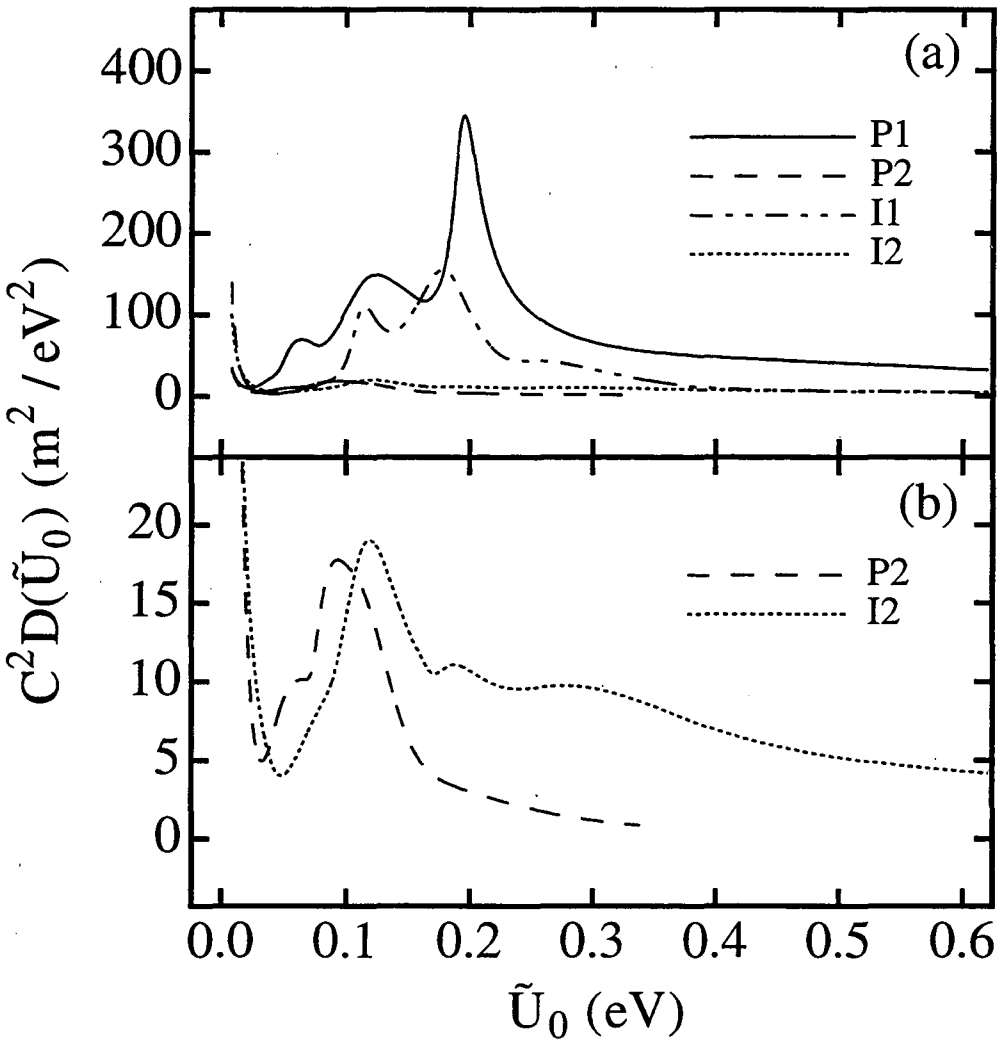

Figure 3.4: $C^2D(\widetilde{U}_0)$ versus $\widetilde{U}_0$ for (a) P1, P2, I1, I2, and (b) P2, I2 with an expanded vertical axis. Calculations are based on Eqs. (3.7), (3.9) with $\tau_0 = 10^{-11}$ s, and (3.10), and the cubic spline fits to the data shown in Fig. 3.3.

and I2 show peaks only near 0.1 eV. We note that the discrepancies between the two-fluid and measured[30] temperature dependences shift the peaks in $C^2D(\widetilde{U}_0)$ only slightly, and do not affect their relative magnitudes. The change in the peak structure implies that both kinds of irradiation largely eliminated the *occupied* sites with pinning energies near 0.2 eV and greatly reduced the number of *occupied* sites with pinning energies near 0.1 eV that we observed in the unirradiated samples. We point out that the energies near 0.1 eV can *not* be those required to hop the *average* distance between defects, ~2 nm for P2 and ~50 nm for I2. If they were, Eq. (3.1) would predict a large difference between P2 and I2. Furthermore, they would be the largest pinning energies present in the crystals. Equations (3.5) through (3.7) would then predict that at temperatures above the value corresponding to $\widetilde{U}_0 = 0.1$ eV, about 50 K, τ would become very long and $S_\Phi(\omega)$ would become vanishingly small. In fact, as shown in Fig. 3.3, $S_\Phi(\omega)$ is certainly non-zero for $T > 50$ K in the irradiated samples. We conclude that the vortices responsible for the observed noise must be pinned at relatively closely spaced defects with a much larger energy barrier against hopping to the next double well, supporting this assumption of our model.

The second important feature is that the area under $C^2D(\widetilde{U}_0)$ prior to irradiation is much greater than after irradiation. Since this area gives the total number of active vortices in that energy range, it is evident from Fig. 3.4 that the number of active vortices in the experimental energy range was drastically reduced by both kinds of irradiation. From the data we are unable to determine if the majority of the vortices that were active in the unirradiated samples near $\widetilde{U}_0 = 0.2$ eV have moved to higher or lower energy after irradiation, but the rapid upturn in $D(\widetilde{U}_0)$ at low energies [Fig. 3.4] indicates that at least some vortices have been pinned in very low energy sites. However, in order for low energy pinning sites to account for the drastically smaller number of active vortices in the irradiated samples, there would need to be an extremely large peak in $D(\widetilde{U}_0)$ in the very narrow energy range 0–10^{-2} eV corresponding to temperatures between 0 K and 4.2 K. To explore this region, we measured $S_\Phi(1\text{ Hz})$ between $T = 1.6$ and 16 K at $|B| = 0$. Between $T = 4.2$ and 16 K, the noise was nearly identical to that measured at $|B| = 100$ μT shown in Fig. 3.3. The resultant $C^2D(\widetilde{U}_0)$ exhibited a peak of magnitude 300 m^2/eV^2 and width $\sim 10^{-2}$ eV. The area under this sharp peak clearly does not account for the area difference under the curves of $C^2D(\widetilde{U}_0)$ of P1 and P2 shown in Fig. 3.4, even when one accounts for the fact that the measurement was made in zero field. Therefore, it is likely that the majority of the vortices that were active near 0.2 eV in the unirradiated samples were pinned at high energy sites

after irradiation, outside the experimental energy range.

Since it is the barrier between different double wells and not the barrier within a given double well that determines where the vortices are pinned as the sample cools through T_c, we would expect some active vortices at low energies even in the presence of high energy pinning sites. However, one might expect that the high energy sites created by the irradiation would trap a large number of the vortices originally responsible for the peaks in $D(\widetilde{U}_0)$ near $\widetilde{U}_0 = 0.1$ eV and 0.2 eV in equal proportion, hence reducing both peaks by the same fraction. Thus, it is surprising that the two very different kinds of irradiation essentially eliminated the peak near 0.2 eV while leaving the peak near 0.1 eV, albeit greatly reduced in height.

3.3.6 Thin Film Sample

Although both kinds of irradiation reduced the $1/\omega$ noise in the crystals substantially, the noise remains higher than that observed in good quality thin films. As an illustration, in Fig. 3.2 we plot $S_\Phi(1\text{ Hz})$ versus $|B|$ at $T = 77$ K for a 300 nm-thick YBCO film laser deposited on a $SrTiO_3$ substrate. We see that the smallest noise power of the crystals, that of P2, is still an order of magnitude larger than that of the thin film in the linear field dependence regime, and a factor of 50 higher in nominally zero field. By the same token, critical currents of thin films are substantially higher than those of irradiated crystals[19, 34, 35], and irradiation has been found to have a negligible effect on the critical current density of typical thin films that have high values of J_c as-prepared[36]. We conjecture that although proton irradiation with the stated fluence reduced the flux noise of a YBCO crystal much more than did ion irradiation, it would be unlikely to reduce the noise of high-J_c thin films. For example, a substantial increase in the fluence would destroy too large a fraction of the material. On the other hand, a lower fluence would create defects that are farther apart, and that might possibly have higher pinning energies. However, as we saw in Sec. 3.3.5, the fluences used to create samples P2 and I2 most likely created high energy pinning sites, but not all of them were occupied by vortices and the noise was not reduced to a value nearly as small as that of a typical thin film. This implies that as-prepared thin films contain such a large number of high energy pinning sites that additional pinning sites created by irradiation with a lower fluence would be unlikely to reduce their $1/\omega$ noise.

3.4 Concluding Remarks

Both proton and heavy ion irradiation reduced $1/\omega$ noise in YBCO crystals. Protons proved much more effective, reducing $S_\Phi(1\text{ Hz})$ at $T = 75$ K by two orders of magnitude at magnetic fields between 0.01 and 2 mT. On the other hand, as is well known[25], both protons and heavy ions with properly chosen fluences produced comparable increases in J_c. The fact that proton and ion irradiation had very different effects on the flux noise and similar effects on J_c reflects the fact that J_c is determined by the pinning *forces* of a large density of defects which collectively pin the vortex lattice present in large magnetic fields. In contrast, the flux noise is determined by the pinning *energies* of sites which trap the small number of vortices present in small magnetic fields as the sample cools below T_c. Thermal activation

of independent vortices over these energy barriers is therefore very sample dependent since it depends on individual pinning sites.

Using the temperature dependence of $S_\Phi(1\text{ Hz})$ and a model based on uncorrelated vortex motion, we showed that the unirradiated samples had peaks in the distribution of activation energies near $\widetilde{U}_0 = 0.1$ and 0.2 eV. After irradiation, there was a single peak near 0.1 eV of much smaller magnitude. The fact that the noise was reduced implies a substantial reduction in the overall magnitude of $D(\widetilde{U}_0)$ which we attributed to the trapping of vortices in high energy sites outside the experimentally accessible energy range. However, the reduced levels of noise in the irradiated crystals were still substantially larger than those that we typically observe in high quality thin films, and we argued that irradiation would therefore probably not further reduce noise in thin films. Thus, we believe that irradiation is unlikely to be a tool for reducing $1/f$ noise in thin film, high-T_c SQUIDs and magnetometers; the increase in this noise when the devices are operated in the earth's magnetic field continues to be a crucial issue. We conclude by stating that further studies are needed to confirm that irradiation, or another method of introducing artificial defects, would not reduce the $1/\omega$ noise in thin films and that even a modest reduction of a factor of two would have important technological implications. However, a recent publication by Dantsker *et al.*[37] demonstrated a novel technique for eliminating vortex motion in thin films of YBCO which could provide a much more effective and less costly alternative to the as yet unproven benefits of irradiation.

3.5 Flux Noise Near the Superconducting Transition in High-Temperature Superconductors

The previous part of this chapter dealt with the flux noise well below the superconducting transition, but the measurement technique has also been used extensively to study the transition itself[16, 38]. Examples of this for two different samples are shown in Figs. 3.5 and 3.6. Figure 3.5(a) shows $S_\Phi(1\text{ Hz})$ versus temperature for a 1500 Å-thick film of $Bi_2Sr_2CaCu_2O_{8+\delta}$ (BSCCO). Approaching the transition from high temperature, $S_\Phi(1\text{ Hz})$ rises sharply and peaks very near the superconducting transition. Evidence that the peak does occur at or near the transition is shown in Fig. 3.5(b), in which is plotted the mutual inductance between the modulation coil and the SQUID, M_f, as a function of temperature. By examining Fig. 2.2(b), one can see that if a superconducting sample is placed near the sensor and a small field is applied with the modulation coil, that screening currents in the sample will counteract this applied field, reducing the net field seen by the sensor and thereby decreasing the mutual inductance between the sensor and the modulation coil. Therefore, by measuring M_f as a function of temperature it is possible to obtain a reasonably accurate estimate of the temperature at which the sample becomes superconducting. A similar measurement on a 3000 Å-thick film of YBCO showing the same general features as Fig. 3.5 is shown in Fig. 3.6. The point which gives $M_f \approx 7$ pH is an artifact of the measurement technique. As described in Section 2.1.3, M_f is determined by resetting the feedback loop which produces a fast step in the magnetic field seen by the sample. Very near, but below, the phase transition vortex pinning is very weak and these field steps can cause vortex hopping which in turn causes anomalies in the measurement of M_f.

The striking feature of Figs. 3.5 and 3.6 is that the magnitude of $S_\Phi(1\text{ Hz})$ at the peak is approximately $10^{-3}\ \Phi_0^2/\text{Hz}$ for both samples. For all the samples measured in our laboratory, the magnitude of the noise peak was relatively sample independent, or at least much less sample dependent than the noise well below the transition. Shown in Table 3.1 is a compilation of the magnitude of $S_\Phi(1\text{ Hz})$ at the peak. One possible explanation for the relatively sample independent value of $S_\Phi(1\text{ Hz})$ at the peak is that near the transition, pinning effects are unimportant and the noise depends only on the fact that the samples are HTSCs. However, the results are not completely sample independent as evidenced by Table 3.1. A possible reason for this can be seen in Fig. 3.7, in which is plotted $S_\Phi(\omega)$ versus frequency for some of the temperatures near the noise peak in Fig. 3.6. Below and

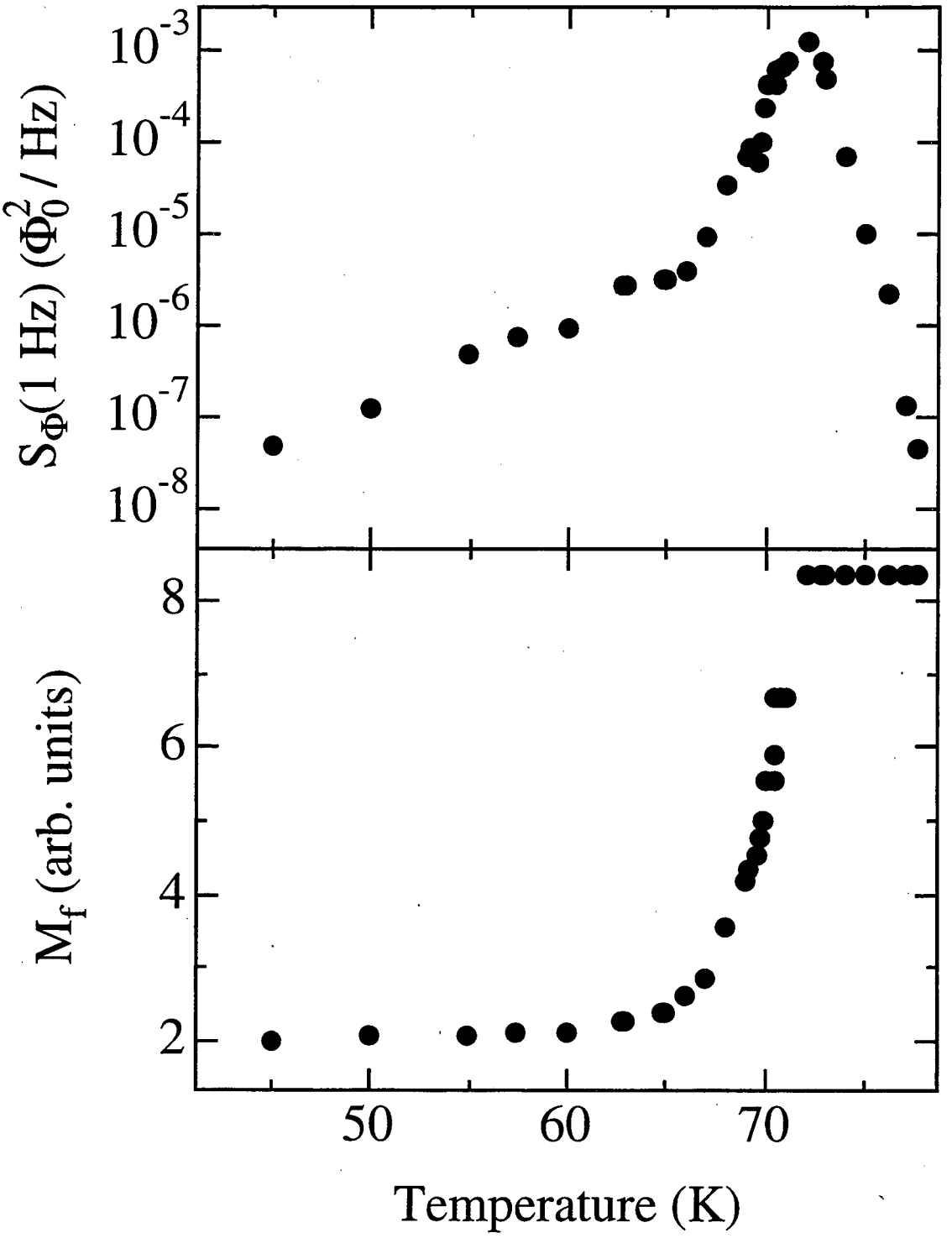

Figure 3.5: (a) $S_\Phi(1\ \mathrm{Hz})$ versus temperature and (b) M_f versus temperature of a 1500 Å-thick film of BSCCO.

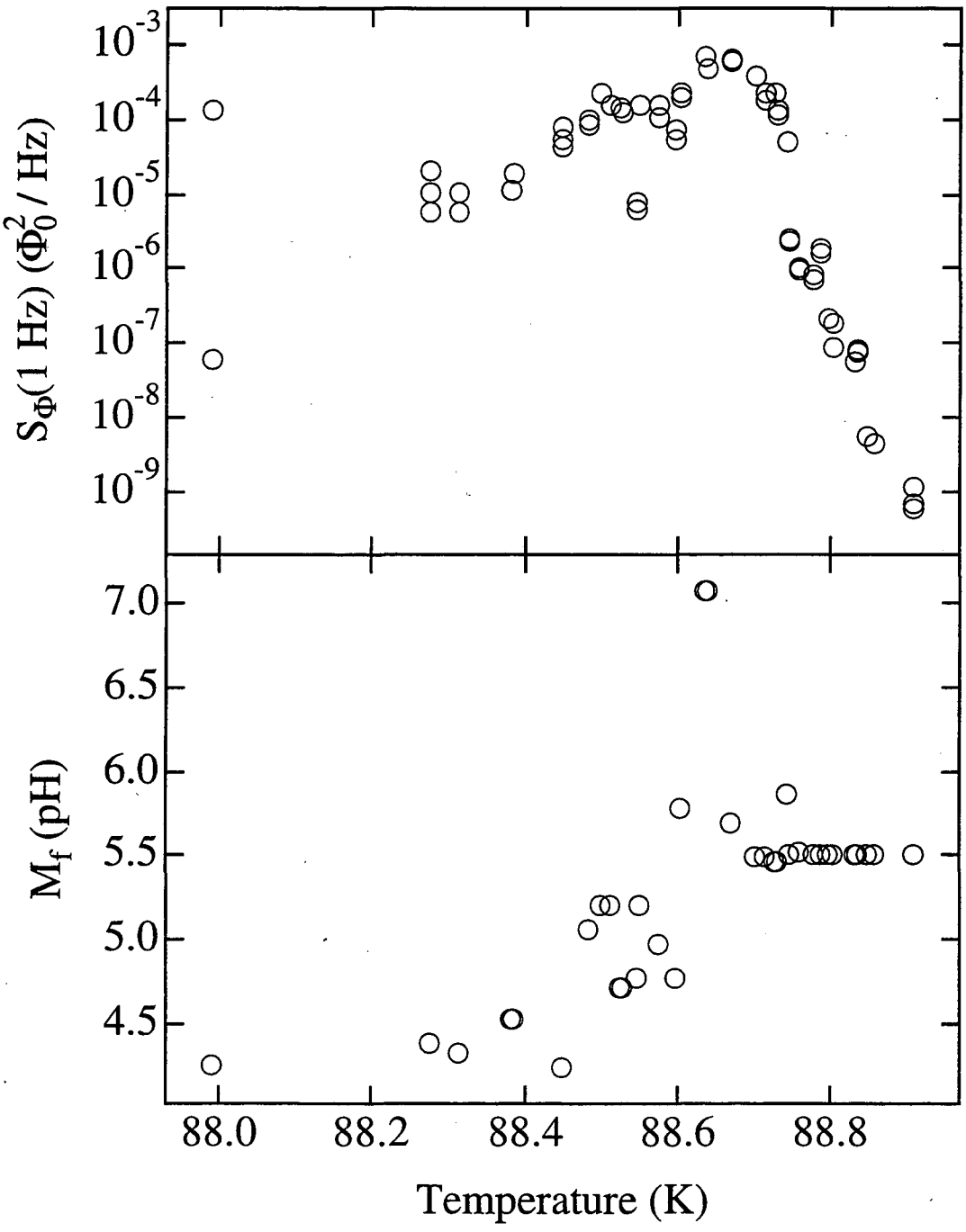

Figure 3.6: (a) $S_\Phi(1\ \mathrm{Hz})$ versus temperature and (b) M_f versus temperature of a 3000 Å-thick film of YBCO.

at the peak, at the temperatures $T = 88.38, 88.60,$ and 88.67 K, the spectra display a $1/\omega^{\alpha}$ behavior, and this behavior occured in every sample that we have measured. However, at temperatures above the peak, the spectra tend to flatten off at low frequencies and have one or two knees or bumps. In some other samples, the behavior of the spectra showed bumps and knees as in Fig. 3.7 and in others just developed a gradually decreasing slope $\alpha \rightarrow 0$. We believe that this is caused by the fact that HTSC materials are never completely uniform and different regions become superconducting at slightly different temperatures. In this way, the regions that are superconducting produce flux noise by vortex motion between pinning centers, and the pinning centers are different in every sample. The Lorentzian spectra of each individual vortex hopping event often add to give a $1/\omega^{\alpha}$-behavior as discussed in Section 3.3.3, but occasional a few dominant hopping events give rise to the bumps as in Fig. 3.7. It is extremely unlikely that the noise near the superconducting transition in HTSCs, at least in the very low-field regime, is caused by the ideal sample behavior, namely fluctuations in the magnitude of the order parameter as mentioned in Section 1. The reasons are one, that the spectra are sample dependent as mentioned above, and two, that the width in temperature for the ideal transition should be very small.

The noise due to the superconducting transition in real, *i.e* non-uniform, HTSC materials has not yet been given a theoretical foundation, although possibilities were suggested by Rogers *et al.*[39, 40] and Foulds *et al.*[41]. Rogers *et al.* suggest that the noise near the transition is caused by Brownian motion of vortex-antivortex excitations which have a variance, $\langle \Phi^2 \rangle$, which is very nearly independent of temperature, and that this leads to a value of $S_{\Phi}(1 \text{ Hz})$ at the peak which depends only on the coupling between the SQUID and the sample. Foulds *et al.*, through measurements of the flux noise of HTSC disks and rings, argue that the data are consistent with a single activation energy for vortex hopping, and similarly to Rogers *et al.* find that the value of $S_{\Phi}(1 \text{ Hz})$ at the peak depends sensitively on the coupling between the SQUID and the sample. However, given the somewhat sample-dependent values of $S_{\Phi}(1 \text{ Hz})$ at the peak as listed in Table 3.1, and the likely role of sample inhomogeneities and SQUID–sample coupling mentioned above, we believe that a universal theory of the flux noise due to the superconducting transtion in HTSCs would be very difficult to verify experimentally. Since we were intrigued by the possibility of studying the superconducting transition, we decided to explore a much more uniform system, namely a two-dimensional Josephson junction array. This will be the topic of the next chapter.

Table 3.1: Compilation of $S_\Phi(1\text{ Hz})$ at the noise peak for all samples measured in our laboratory.

Sample	Material	Thickness	Description	$S_\Phi^{\text{peak}}(1\text{Hz})$
I1	YBCO	30 μm	crystal	1×10^{-4}
I2	YBCO	30 μm	crystal, heavy ion irradiated	6×10^{-4}
P2	YBCO	30 μm	crystal, proton irradiated	1×10^{-3}
HITC812	YBCO	3000 Å	film	4×10^{-3}
holey	YBCO	3000 Å	film	1×10^{-3}
M031589A	YBCO	3000 Å	film	9×10^{-4}
M0497C7	YBCO	4000 Å	a-axis film	8×10^{-4}
df381	YBCO	1500 Å	film	4×10^{-3}
Y2th	YBCO	2000 Å	film	1×10^{-3}
087131B3	YBCO	2000 Å	square-washer-shape film	1×10^{-3}
G8835C5	YBCO	2000 Å	square-washer-shape film	6×10^{-4}
SLITRING	YBCO	2000 Å	square-washer-shape film	7×10^{-5}
P2568C	YBCO	30 μm	crystal	4×10^{-4}
BSCCO1	BSCCO	40 μm	flake	9×10^{-5}
BSCCO2	BSCCO	150 μm	flake	1×10^{-4}, 6×10^{-5}
961	BSCCO	750 Å	film	8×10^{-4}
978	BSCCO	1500 Å	film	1×10^{-3}
LLS1	BSCCO	4 μm	crystal	7×10^{-4}
LLBA	BSCCO	11 μ	crystal	6×10^{-4}
48S	BSCCO	29 μm	crystal	2×10^{-4}
TCBCO1	TCBCO	2 μm	film	4×10^{-4}
TCBCO3	TCBCO	2 μm	film	6×10^{-4}

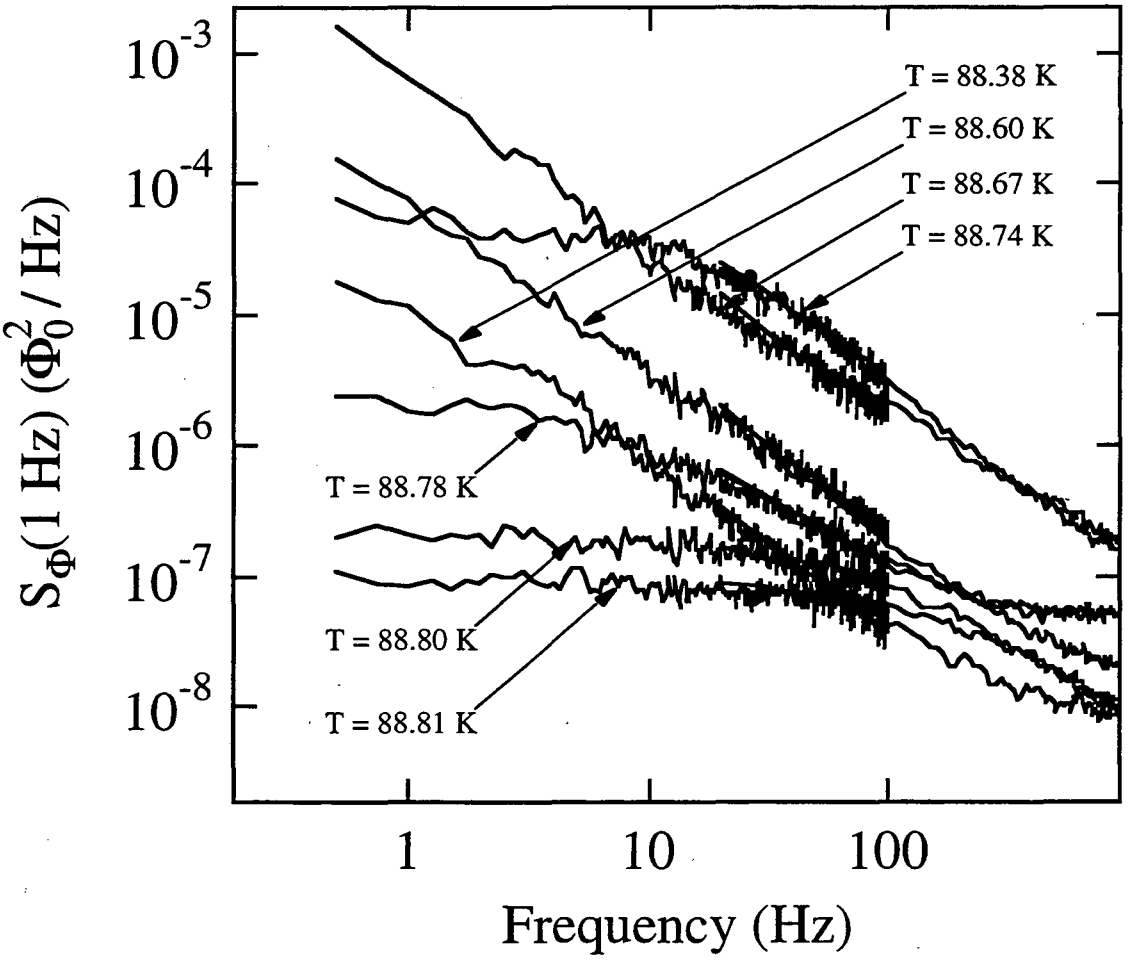

Figure 3.7: $S_\Phi(\omega)$ versus ω at a few selected temperatures near the superconducting transition from the data of Fig. 3.6.

Chapter 4

Two-Dimensional Josephson Junction Arrays

4.1 Introduction

In the previous chapter, vortex motion in high-temperature superconductors (HTSCs) was studied well below the transition temperature with the goal of understanding pinning properties in these materials. The measured spectral density of flux noise, $S_\Phi(\omega)$, was highly sample-dependent because of the varying defect structure, both inherent and artificially produced. The measurements produced insight into the possibility of reducing vortex motion in these materials, but both the fundamental nature of vortex motion and the superconducting phase transition was not addressed. The flux noise associated with the phase transition in HTSC materials has been studied in some detail in our group[16], with the result that the magnitude of $S_\Phi(1\text{ Hz})$ at the transition temperature was relatively sample-independent and approximately $10^{-3}\ \Phi_0^2/\text{Hz}$. However, even a qualitative explanation of this result is lacking.

In order to study the superconducting transition, one would ideally like to have a pinning-free sample. As this is nearly impossible in high-temperature superconductors, we decided to explore a much more uniform system, namely a two-dimensional Josephson junction array (JJA). The two dimensional metal-superconductor transition has been widely studied in two dimensional arrays of Josephson junctions because these systems are very uniform and their relevant parameters are easily determined. It is widely accepted that the zero-field transition is described by the Kosterlitz-Thouless-Berezinskii (KTB) theory [5, 6, 7,

12] and its extension to non-zero frequency [42, 43, 44, 45, 46]. According to this theory, phase coherence is established throughout the sample below a temperature T_{KTB}, and the system is superconducting. For temperatures above T_{KTB} but below the bulk transition temperature, even though individual islands are superconducting the array is not. The thermal excitations, vortices and antivortices, that trigger this phase transition are topological defects of the order parameter. Below T_{KTB} vortices and antivortices bind in pairs to produce a vortex dielectric, while above T_{KTB} the pairs dissociate to form a vortex plasma. In the vortex plasma phase, one can identify a characteristic length, ξ, as the average separation between free vortices; as $T \rightarrow T^{+}_{\mathrm{KTB}}, \xi$ diverges. Thermal fluctuations that perturb the vortex density away from its equilibrium value relax through some local dynamic process. Thus, associated with the characteristic length ξ there is a characteristic frequency, $2\pi\omega_{\xi}$, corresponding to the inverse of the time required for the disturbance to propagate across the distance ξ. As ξ diverges, $\omega_{\xi} \rightarrow 0$, signifying critical slowing down. In general $\omega_{\xi} \propto (\xi/\xi_0)^{-z}$, where the exponent z depends on the dynamics of the relaxation and ξ_0 is a length scale characteristic to the specific sample. For simple diffusion, $z = 2$.

Previous experimental studies had involved both electrical resistance [47, 48, 49, 50, 51, 52, 53, 54, 55, 56, 57] and two-coil mutual inductance [58] techniques, both of which apply an external force to the system and are generally confined to a specific frequency. Because the transition to the resistive state is determined by the dissociation of vortex pairs by thermal fluctuations, these external forces, which also dissociate pairs, affect one's ability to study the intrinsic critical phenomena near the true thermodynamic transition temperature. In addition, measurements confined to a specific frequency do not give information about the dynamics of the phase transition and if the specific frequency is not zero, one can not even be sure that the measurement is measuring the correct behavior of the zero-frequency phase transition. For this reason, we undertook to study the equilibrium dynamics of the KTB transition using the apparatus described in Chapter 2.

4.2 Theory

As mentioned in Section 4.1, for a previous publication [59] [hereafter referred to as (I)] a scaling ansatz was derived to describe the behavior of $S_\Phi(\omega)$ near the KTB transition. In addition, a rather simplistic model was proposed to describe the low-frequency behavior of $S_\Phi(\omega)$ which allowed extraction of the dynamic critical exponent z. Professor Dung-Hai Lee later elaborated on that scaling theory in order to develop a more detailed theory giving concrete predictions for the high- and low-frequency behavior of $S_\Phi(\omega)$[60], and this theory will be explained below.

It will be useful to begin with the schematic illustration of the flux noise measurement shown in Fig. 4.1. A square flux sensor of area $\ell_{\rm eff}^2$ is placed a distance d above the array of area A. The cartesian coordinate system is defined by the components (x, y, z) so that the array lies in the plane of $z = 0$. Three-dimensional vectors will be denoted by $(\vec{x}, z)$, where $\vec{x}$ is the vector component in the plane of the array and sensor, and primed coordinates designate the plane of the array while unprimed coordinates denote the plane of the sensor. The fluctuating vortex density in the array, $\rho_v(\vec{x}', 0; t)$, generates a magnetic field at the point $(\vec{x}, d)$, $B_z(\vec{x}, d; t)$, with an instantaneous z-component

$$B_z(\vec{x}, d; t) = \Phi_0 \int d^2x' \mathcal{M}(\vec{x} - \vec{x}', d)\rho_v(\vec{x}', 0; t). \tag{4.1}$$

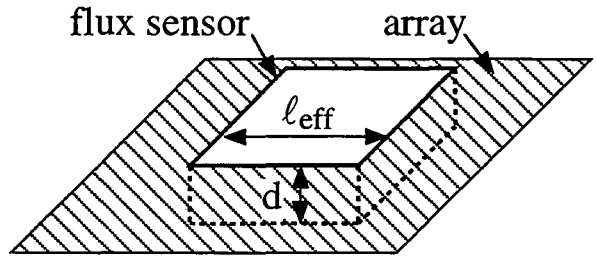

Figure 4.1: Configuration of flux noise measurement showing a square flux sensor of width $\ell_{\rm eff}$ a distance d away from an array.

In the above, $\Phi_0 = h/2e$ is the superconducting flux quantum and

$$\mathcal{M}(\vec{x} - \vec{x}', d) = d/(|\vec{x} - \vec{x}'|^2 + d^2)^{3/2} \tag{4.2}$$

is the array-sensor coupling function.[60] Equations (4.1) and (4.2) ignore the distortion of the magnetic field due to the sensor. Since the sensors are superconducting, it is possible that the field produced by the vortices in the array might be affected by the sensor, but calculation of these effects would be very difficult and time consuming. Instead, taking a more practical approach, the experiment was carried out with sensors with the three different geometries shown in Fig. 2.3. The results will be discussed in detail in the following section, but the conclusion was that sensor geometry did not affect the measurements. Therefore, it will be assumed for the following theoretical calculations that the sensors have no effect on the field generated by the vortices in the array.

Next, $B_z(\vec{x}, d; t)$ is integrated over $\vec{x}$ enclosed by the area ℓ_{eff}^2 of the sensor so that the instantaneous total flux, $\Phi(t)$, through the sensor is

$$\Phi(t) = \int d^2x B_z(\vec{x}, d; t). \tag{4.3}$$

From Eqs. (4.1) and (4.3) the flux-flux autocorrelation function is given by

$$\langle \Phi(t)\Phi(t') \rangle = \Phi_0^2 \int d^2x d^2y d^2x' d^2y' \mathcal{M}(\vec{x} - \vec{x}', d)\mathcal{M}(\vec{y} - \vec{y}', d)\langle \rho_v(\vec{x}', 0; t)\rho_v(\vec{y}', 0; t') \rangle, \tag{4.4}$$

where $\langle\rangle$ denotes the thermodynamic average and the primed (unprimed) integrals are taken over the area of the array (sensor). The spectral density of magnetic flux noise is defined as $S_\Phi(\omega) \equiv \int dt e^{i\omega t}\langle \Phi(t)\Phi(0) \rangle$, so that substituting Eq. (4.4) in to this definition gives the general expression

$$S_\Phi(\omega) = \Phi_0^2 \int d^2x d^2y d^2x' d^2y' dt e^{i\omega t} \mathcal{M}(\vec{x} - \vec{x}', d)\mathcal{M}(\vec{y} - \vec{y}', d)\langle \rho_v(\vec{x}', 0; t)\rho_v(\vec{y}', 0; t') \rangle. \tag{4.5}$$

In general, $\langle \rho_v(\vec{x}', 0; t)\rho_v(\vec{y}', 0; t') \rangle$ depends on $t - t'$, and ignoring boundary effects it depends on $\vec{x}' - \vec{y}'$. For the subsequent analysis it is convenient to go to the Fourier representation of Eq. (4.5) by substituting

$$\mathcal{M}(\vec{x} - \vec{x}'; d) = (2\pi)^{-2} \int d^2q \mathcal{M}(q, d) e^{i\vec{q}\cdot(\vec{x} - \vec{x}')} \tag{4.6a}$$

and

$$\langle \rho_v(\vec{x}', 0; t)\rho_v(\vec{y}', 0; 0) \rangle = (2\pi)^{-3} \int d^2q d\omega \Lambda_{vv}(\vec{q}, \omega) e^{i\vec{q}\cdot(\vec{x}' - \vec{y}') - i\omega t}. \tag{4.6b}$$

In addition, to simplify the calculation a cutoff is defined for the integration over the area of the sensor via a form factor, $\Upsilon(q, \ell_{\text{eff}})$, as

$$\int_{\vec{x}\in\text{sensor}} d^2x e^{i\vec{q}\cdot\vec{x}} \rightarrow \Upsilon(q, \ell_{\text{eff}}) \equiv \int d^2x e^{-|x|/\ell_{\text{eff}}} e^{i\vec{q}\cdot\vec{x}} = \frac{4\pi\ell_{\text{eff}}^2}{[1+(q\ell_{\text{eff}})^2]^{3/2}}. \tag{4.7}$$

Since vortices outside of the area under the sensor contribute negligibly to the flux threading it, this particular cutoff procedure should not influence the results. Next, substituting Eqs. (4.6) and (4.7) into Eq. (4.4) yields

$$S_\Phi(\omega) = \Phi_0^2 \int (d^2q/4\pi^2)\Upsilon^2(q, \ell_{\text{eff}})\mathcal{M}^2(q, d)\Lambda_{vv}(\vec{q}, \omega), \tag{4.8}$$

where

$$\mathcal{M}(q, d) = e^{-qd}. \tag{4.9}$$

In order to proceed further, one can draw on the work of Houlrik *et al.*[61] who showed that $\Lambda_{vv}(\vec{q}, \omega)$ is related to the imaginary part of the inverse Coulomb gas dielectric function, $\epsilon(\vec{q}, \omega)$, via

$$\Lambda_{vv}(\vec{q}, \omega) = \frac{T'}{\pi\omega} q^2 \left| Im[\epsilon^{-1}(\vec{q}, \omega)] \right|. \tag{4.10}$$

In Eq. (4.10), T' is the dimensionless Coulomb gas temperature and $Im(x)$ is the imaginary part of x. Thus, substituting Eq. (4.10) into Eq. (4.8) gives

$$S_\Phi(\omega) = \frac{\Phi_0^2 T'}{4\pi^3} \frac{1}{\omega} \int d^2q q^2 \Upsilon^2(q, \ell_{\text{eff}})\mathcal{M}^2(q, d) \left| Im[\epsilon^{-1}(q, \omega)] \right|. \tag{4.11}$$

Up to this point, the calculation been very general in the sense that it did not involve any assumptions about the nature of the vortex dynamics or the phase transition. The next step will be to elucidate the predicted scaling behavior of $S_\Phi(\omega)$ as well its frequency dependence, beginning with Eq. (4.11). The first assumption is that $S_\Phi(\omega)$ is caused by vortex dynamics associated with the KTB transition. As mentioned in Section 4.1, for the KTB transition there is a diverging correlation length, ξ, and an associated frequency, ω_ξ, which is defined as

$$\omega_\xi \equiv \omega_0(\xi_0/\xi)^z, \tag{4.12}$$

where ω_0 is a characteristic frequency, ξ_0 is a characteristic length, and z is the dynamic critical exponent.

Now, the scaling behavior of $S_\Phi(\omega)$ can be calculated by noting that $\epsilon(q,\omega)$ is dimensionless and that the only relevant length and frequency scales are ξ and ω_ξ respectively. In other words, the dynamic scaling form for the vortex dielectric function is given by expressing it in terms of dimensionless lengths and frequencies scaled by powers of ξ and ω_ξ respectively. Therefore, near the KTB transition

$$|Im[\epsilon^{-1}(q,\omega)]| = \mathcal{F}_1(q\xi, \omega/\omega_\xi, A/\xi^2), \tag{4.13}$$

where $\mathcal{F}_1$ is a scaling function and the term A/ξ^2 has been added to account for possible finite-size effects. Substituting Eq. (4.13) for the dielectric function and Eqs. (4.7) and (4.9) for the form factor and coupling function respectively into Eq. (4.11) gives

$$\begin{aligned} S_\Phi(\omega) &= \frac{4\Phi_0^2 T'}{\pi}\frac{1}{\omega}\int d^2(q\xi)(q\xi)^2 \frac{(\ell_{\text{eff}}/\xi)^4}{\{1+[(q\xi)(\ell_{\text{eff}}/\xi)]^2\}^3} e^{-2(q\xi)(d/\xi)} \mathcal{F}_1(q\xi, \omega/\omega_\xi, A/\xi^2) \\ &\equiv (1/\omega)\mathcal{F}_2(\omega/\omega_\xi, \ell_{\text{eff}}/\xi, d/\xi, A/\xi^2), \end{aligned} \tag{4.14}$$

where $\mathcal{F}_2$ is another scaling function. Equation (4.14) is the result for the scaling behavior of $S_\Phi(\omega)$ and agrees with the result of (I).

Next, in order to predict the behaviors of $S_\Phi(\omega)$ in the limit of both high and low frequencies let's return to Eq. (4.11). Since the product of the SQUID form factor [Eq. (4.7)] and the array-SQUID coupling function [Eq. (4.9)] restricts the region in $\vec{q}$ space that dominates the integral to be that of $q \cdot min(d, \ell_{\text{eff}}) \lesssim 1$; to a good approximation the q in $\epsilon(q,\omega)$ of Eq. (4.11) can be replaced by zero.[1] In this case, provided that finite-size effects are unimportant and therefore ϵ is independent of the array size, A, $S_\Phi(\omega)$ is given by

$$\begin{aligned} S_\Phi(\omega) &= \frac{\Phi_0^2 T'}{4\pi^3}\frac{1}{\omega}\left|Im[\epsilon^{-1}(0,\omega)]\right| \int d^2q q^2 \Upsilon^2(q, \ell_{\text{eff}}) \mathcal{M}^2(q,d) \\ &\equiv \frac{\Phi_0^2 T'}{4\pi^3}\frac{1}{\omega}\left|Im[\epsilon^{-1}(0,\omega)]\right| \mathcal{F}_3(\ell_{\text{eff}}, d), \end{aligned} \tag{4.15}$$

where $\mathcal{F}_3$ is a function which is determined by the geometry of the measurement apparatus. This is an important prediction of the calculation which justifies the assumption in (I) that the function $\mathcal{F}_2$ in the scaling prediction of Eq. (4.14) is independent of $(\ell_{\text{eff}}/\xi, d/\xi,$ and $A/\xi^2)$. It depends only on two factors: first, that the sensor selects the long-wavelength excitations so that only the zero-wavevector limit of $\epsilon(q,\omega)$ is relevant, and second, that finite-size effects

[1] This approximation is valid provided that $q\xi \lesssim 1$, or equivalently $\xi/\min(d, \ell_{\text{eff}}) \lesssim 1$, which is likely to be true as will be discussed in Section 4.4

are unimportant. Therefore, a constant $F \equiv \mathcal{F}_3(\ell_{\text{eff}}, d)$ can be substituted in to Eq. (4.15) to give

$$S_\Phi(\omega) = \frac{F\Phi_0^2 T'}{4\pi^3}\frac{1}{\omega}\left|Im[\epsilon^{-1}(0,\omega)]\right|. \tag{4.16}$$

From Eq. (4.16), we see that the frequency dependence of $S_\Phi(\omega)$ is determined solely by the zero-wavevector dielectric function, $\epsilon(\omega) \equiv \epsilon(q \to 0, \omega)$. This quantity was calculated by Ambegaokar *et al.*[43, 44, 45] in the context of superfluid films, and it will be useful to draw on their calculations here.

An important first assumption is that the vortices diffuse with a diffusion constant D. Next, the vortex dielectric function is decomposed into two parts, one representing the contribution of bound vortex-antivortex pairs and the second due to the contribution of free vortices:

$$\epsilon(\omega) = \epsilon_b(\omega) + \epsilon_f(\omega). \tag{4.17}$$

Let's concentrate on the bound pair contribution first. Via a Fokker-Planck equation, the bound pair contribution was shown[43] to be given by the equation

$$\epsilon_b(\omega) = 1 + \int_{r_0}^{\infty} dr \frac{d\tilde{\epsilon}(r)}{dr} g(r,\omega), \tag{4.18}$$

where $\tilde{\epsilon}(r)$ is the length-dependent dielectric constant, $g(r,\omega)$ is the response function for pairs of separation r, and r_0 is small-length-scale cutoff. In the region of temperatures which are relevant to the measurements to be described in the following section, $\epsilon(r)$ can be well described by the approximation[43]

$$\tilde{\epsilon}(r) \approx \frac{\epsilon_c}{1 + [2\ell n(r/r_0)]^{-1}}, \tag{4.19}$$

where ϵ_c is a constant defined by the length- and temperature-dependent dielectric constant, $\epsilon(r,T)$, as $\epsilon_c = \tilde{\epsilon}(r \to \infty, T = T_{\text{KTB}})$ and r_0 is the minimum vortex separation. The response function $g(r,\omega)$ can be well approximated by[44]

$$g(r,\omega) \approx \frac{14Dr^{-2}}{14Dr^{-2} - i\omega}. \tag{4.20}$$

Since the dielectric constant in Eq. (4.19) is a slowly varying function of r over the region where $g(r,\omega)$ crosses between its low- and high-frequency behaviors, the real and imaginary parts of the response function can be approximated by

$$Re[g(r,\omega)] \approx \Theta(14Dr^{-2} - \omega) \tag{4.21a}$$

and

$$Im[g(r,\omega)] \approx (\pi/4) r \delta(r - \sqrt{14D/\omega}), \tag{4.21b}$$

respectively, where $\Theta(x)$ and $\delta(x)$ are the standard Heavyside and delta functions. From Eqs. (4.21), it is apparent that the behavior of the bound pair contribution to the dielectric constant is determined by a characteristic vortex-antivortex pair separation

$$r_\omega \equiv \sqrt{14D/\omega}. \tag{4.22}$$

The physical interpretation of Eqs. (4.21) and (4.22) is that if an electric field of frequency ω is applied to the vortices, only those pairs which have a separation smaller than r_ω have sufficient time to follow the applied field and thus determine the real, or inductive, response. Similarly, the imaginary, or dissipative, response is dominated by those vortices which move the largest distance in one cycle, those with separation r_ω.

The next step is to substitute Eqs. (4.21) for the response function in to Eq. (4.18) and use the definition of r_ω given by Eq. (4.22) to find

$$Re[\epsilon_b(\omega)] = \tilde{\epsilon}(r = r_\omega) \tag{4.23a}$$

and

$$Im[\epsilon_b(\omega)] = \frac{\pi}{4}\left[r\left(\frac{d\tilde{\epsilon}(r)}{dr}\right)\right]_{r=r_\omega}. \tag{4.23b}$$

Using the formula for $\tilde{\epsilon}(r)$ given by Eq. (4.19) in Eqs. (4.23) gives

$$\begin{aligned} Re[\epsilon_b(\omega)] &= \frac{\epsilon_c}{1 + [2\ell n(r_\omega/r_0)]^{-1}} \\ &\approx \epsilon_c \end{aligned} \tag{4.24a}$$

and

$$\begin{aligned} Im[\epsilon_b(\omega)] &= \frac{\pi}{8} \frac{\epsilon_c}{\{1 + [2\ell n(r_\omega/r_0)]^{-1}\}^2} \frac{1}{\ell n^2(r_\omega/r_0)} \\ &\approx \frac{\pi \epsilon_c}{8\ell n^2(r_\omega/r_0)}. \end{aligned} \tag{4.24b}$$

The approximations in Eqs. (4.24) are due to the fact that $r_\omega \gg r_0$ in order for the calculation to be physically meaningful.

Having calculated the bound pair contribution to the dielectric constant, let's turn to the free vortex contribution. The free vortices give rise to a Drude-like contribution to the dielectric constant,

$$\epsilon_f(\omega) = \frac{4\pi i}{\omega}\left(\frac{\pi E_J D\langle\rho_v\rangle}{k_B T}\right). \tag{4.25}$$

The results of Eqs. (4.24) and (4.25) will now allow the determination of the flux noise via Eq. (4.16). First, an important distinction must be made regarding whether the free or bound vortices dominate the system response at a given frequency. The two relevant length scales determining which contribution dominates are the correlation length ξ and the diffusion length $r_D \equiv \sqrt{D/\pi\omega}$. From these two lengths, one can define a crossover frequency as the frequency at which $r_D = \xi$, so that

$$\omega_\xi = D/\pi\xi^2. \tag{4.26}$$

Defining the crossover frequency as identical to ω_ξ follows from the logical assumption that since it is determined by the correlation length in this model, it is natural to equate it with the generic characteristic frequency defined in Eq. (4.12). In doing so, Eqs. (4.12) and (4.26) give $z = 2$, as expected for diffusive dynamics, and

$$\omega_0 = D/\pi\xi_0^2. \tag{4.27}$$

Equation (4.26) implies that measurements at frequencies lower than ω_ξ probe fluctuations in the equilibrium vortex density which have diffused a distance larger than ξ. To these measurements, the system appears disordered in the sense that the free vortices destroy any coherence of the fluctuations. On the other hand, measurements at frequencies larger than ω_ξ probe fluctuations on length scales smaller than ξ. In other words, high-frequency measurements probe the critical behavior even though the temperature is higher than the true thermodynamic transition temperature. For frequencies $\omega > \omega_\xi$, Ambegaokar *et al.*[45] found that bound vortex-antivortex pairs dominate the system response. Therefore, the flux noise in this regime can be found by first calculating $1/\epsilon(\omega) = 1/\epsilon_b(\omega)$ from Eqs.

(4.24) to find

$$\begin{aligned}\left|Im[\epsilon^{-1}(0,\omega)]\right| &= \frac{Im[\epsilon_b(\omega)]}{Re[\epsilon_b^2(\omega)] + Im[\epsilon_b^2(\omega)]} \\ &= \frac{\frac{\pi\epsilon_c}{8\ell n^2(r_\omega/r_0)}}{\epsilon_c^2 + \frac{\pi^2\epsilon_c^2}{64\ell n^4(r_\omega/r_0)}} \\ &\approx \frac{\pi}{8\epsilon_c \ell n^2(r_\omega/r_0)},\end{aligned} \tag{4.28}$$

and then substituting this result in to Eq. (4.16), with the result

$$S_\Phi(\omega \gg \omega_\xi) = \frac{F\Phi_0^2 T'}{32\pi^2\epsilon_c}\frac{1}{\omega\ell n^2(r_\omega/r_0)}. \tag{4.29}$$

Equation (4.29) predicts that $S_\Phi(\omega) \propto [\omega\ell n^2(r_\omega/r_0)]^{-1}$. Thus, the dominant frequency dependence is $1/\omega$ with a logarithmic correction. In the opposite regime, when $\omega < \omega_\xi$, Ambegaokar *et al.*[45] found that free vortices dominate the system response. The flux noise is then given by substituting the free vortex contribution to $\epsilon(\omega)$ given by Eq. (4.25) into Eq. (4.16) for $S_\Phi(\omega)$ with the result

$$S_\Phi(\omega \ll \omega_\xi) = \frac{\kappa F\Phi_0^2 T'^2}{16\pi^5 D}\xi^2, \tag{4.30}$$

where $\langle\rho_v\rangle$ has been replaced by defining a proportionality constant κ such that $\langle\rho_v\rangle^{-1} = \kappa\xi^2$.

Equation (4.30) has an qualitative intuitive explanation in terms of the fluctuation-dissipation theorem. At low frequencies, the array can be viewed as a system with a resistance R which, via the fluctuation-dissipation theorem, produces incoherent current fluctuations with a frequency-independent spectral density $S_I \propto T'/R$, where the effective temperature of the vortices, T', replaces the usual $k_B T$. Since a current fluctuation in the sample produces a magnetic flux fluctuation through the sensor, the flux noise is then $S_\Phi \propto S_I \propto T'/R$. One can then make the simple argument that the sample's low-frequency resistance is proportional to the average density of free vortices, $R \propto \langle\rho_v\rangle \propto 1/\xi^2$, and therefore $S_\Phi \propto T'\xi^2$. Aside from an extra factor of T', the prediction of Eq. (4.30) agrees with this qualitative argument, thus lending support to the more rigorous calculation.

Now that predictions for the scaling behavior [Eq. (4.35)], high-frequency behavior [Eq. (4.29)], and low-frequency behavior [Eq. (4.30)] of $S_\Phi(\omega)$ have been developed, let's turn to a description of the measurements.

4.3 Measurements

4.3.1 Current-Voltage Measurements

In order to make a quality check of arrays A and B, the temperature dependence of the differential resistance at zero bias current, $(dV/dI)_{I=0}$, was measured as a function of temperature, T, with an rms current of 10 μA at a frequency of 47 Hz as described in Section 2.1.3. Figures 4.2(a) and 4.2(b) show $(dV/dI)_{I=0}$ versus T for arrays A and B respectively. The drop in resistance near $T = 8$ K marks the transition temperature of the niobium islands. As the temperature is lowered, a resistive plateau develops and is followed by a second precipitous drop, which is the standard signature for the phase transition as seen in previous experiments [47, 48, 49, 50, 51, 52, 53, 54, 55, 56, 57]. Since both arrays A and B qualitatively exhibited the expected behavior, $(dV/dI)_{I=0}$ was not measured for array C.

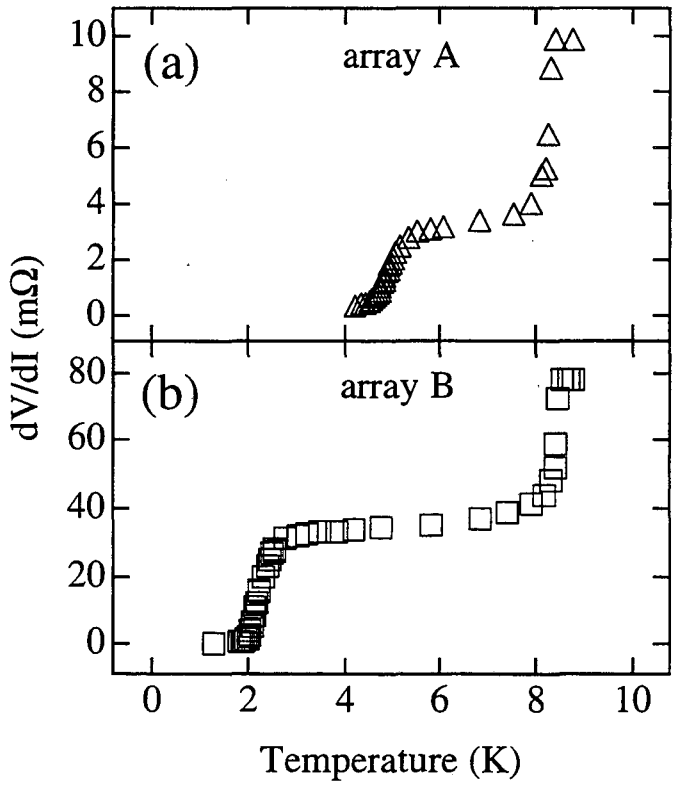

Figure 4.2: dV/dI versus temperature of (a) array A and (b) array B, measured with zero static bias current and an rms current of 10 μA at a frequency of 47 Hz.

For the measurements described here, a more important property than $(dV/dI)_{I=0}$ of the arrays is the temperature dependent critical current per junction, $i_c(T)$. This quantity determines the dimensionless Coulomb gas temperature, T', introduced in Section 4.2 via

$$T' = k_B T/E_J(T) = 2ek_B T/\hbar i_c(T). \tag{4.31}$$

In order to determine $i_c(T)$, dV/dI was measured as a function of the static bias current. The critical current was defined by setting the current at which dV/dI was a maximum as $Ni_c(T)$, where N is the number of junctions across the width of the array[62, 63]. A representative example of this is shown in Fig. 4.3(a), as measured on array B at $T = 1.29$ K.

Well below the transition temperature of the individual islands, the critical current of SNS junctions in the dirty limit are expected to have the temperature dependence[64]

$$i_c(T) = i_c(0)\exp(-\gamma\sqrt{T}). \tag{4.32}$$

Shown in Figs. 4.3(b) and 4.3(c) are $\ell n[i_c(T)]$ versus $\sqrt{T}$ data for all three arrays from which we extract the values for $i_c(0)$ and γ shown in Table 4.1. As will be describe later, four separate measurements were made on array B, which will be denoted as B(1) through B(4) in chronological order. As evident from Fig. 4.3(b), the critical current of array B did decrease as a function of time. In addition, the arrays had very different critical current behaviors, and this will allow the determination of the effects this had on the magnetic flux noise measurements.

Table 4.1: Single junction parameters for arrays during measurements shown in Fig. 4.4

Array	$i_c(0)$ (A)	γ	r_n (mΩ)
A	1.6×10^{1}	8.2	1
B(1)	1.4×10^{-1}	9.1	3
B(2)	1.7×10^{-1}	9.7	3
B(3)	9.1×10^{-2}	9.3	3
B(4)	9.1×10^{-2}	9.3	3
C	2.7×10^{-2}	5.8	30

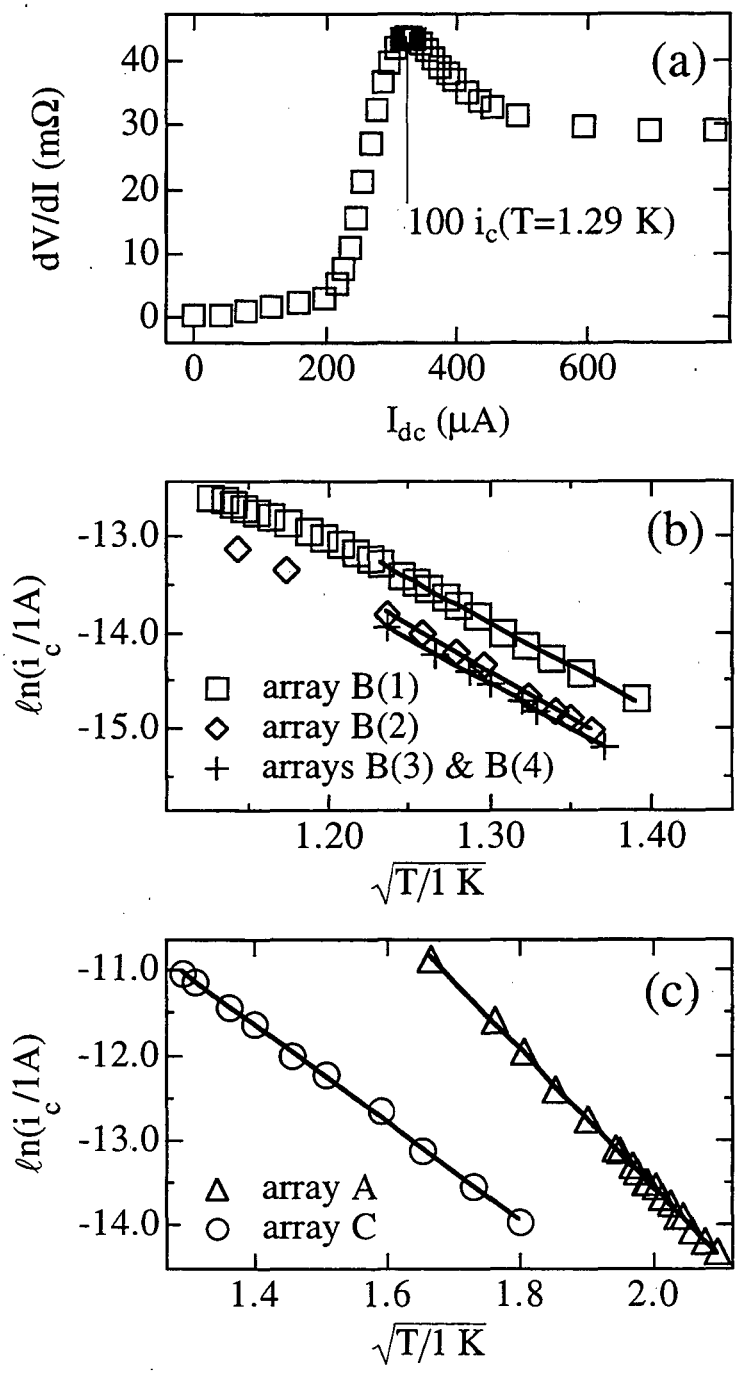

Figure 4.3: (a) dV/dI versus I_{dc} for array B(1), showing $N(=100)i_c(T = 1.29\ \text{K})$. (b) and (c) $\ell n(i_c)$ versus $\sqrt{T}$ measured during the experimental runs shown in Fig. 4.4. Values of the slopes and intercepts extracted from the straight line fits shown are given in Table 4.1.

4.3.2 Noise Measurements

To carry out magnetic flux noise measurements of the KTB transition in the absence of an applied magnetic field,the apparatus was cooled in the ambient field inside the mu-metal shield surrounding the dewar, which was measured to be less than 1 μT. This field therefore produced a frustration, f, of less than 4% for array A and less than 5% for arrays B and C. Frustration is defined as the fraction of a superconducting flux quantum, $\Phi_0 = h/2e$, per unit cell of the array generated by the magnetic field perpendicular to the array. Because the phase transitions for all three arrays occurred at temperatures below 4.2 K, it was necessary lower the helium pressure with a mechanical pump to reduce the bath temperature to approximately $1.2 - 1.3$ K. A current was then applied to the resistive heater to bring the array to the desired temperature and the spectral density of magnetic flux noise, $S_\Phi(\omega)$, was measured.

Shown in Fig. 4.4 are the resultant noise spectra for six different measurements, and the array-SQUID combinations used for each figure are listed in Table 4.2 along with the SQUIDs' effective diameters, ℓ_{eff}. All the figures in Fig. 4.4 show $S_\Phi(\omega)$ versus frequency measured at a number of different temperatures above T_{KTB}. The spectra at each temperature are compilations of two or three spectra measured with different bandwidths, and the larger scatter seen in the low-frequency segments is caused by averaging fewer times than in the higher frequency segments. Lower temperatures correspond to larger values of the low-frequency noise. The letters correspond to the chronological order in which the measurements were made. Figure 4.4(a) shows $S_\Phi(\omega)$ of array A measured with SQUID 1. Figure 4.4(b) shows $S_\Phi(\omega)$ of array B(1), again measured with SQUID 1, allowing the comparison of the results from arrays of different geometry [Figs. 4.4(a) and 4.4(b)]. The scatter in

Table 4.2: Experimental parameters for data shown in Fig. 4.4.

Array	Figure	SQUID	ℓ_{eff} (μm)
A	4.4(a)	1	400
B(1)	4.4(b)	1	400
B(2)	4.4(c)	2	250
B(3)	4.4(d)	3	100
B(4)	4.4(e)	1	400
C	4.4(f)	1	400

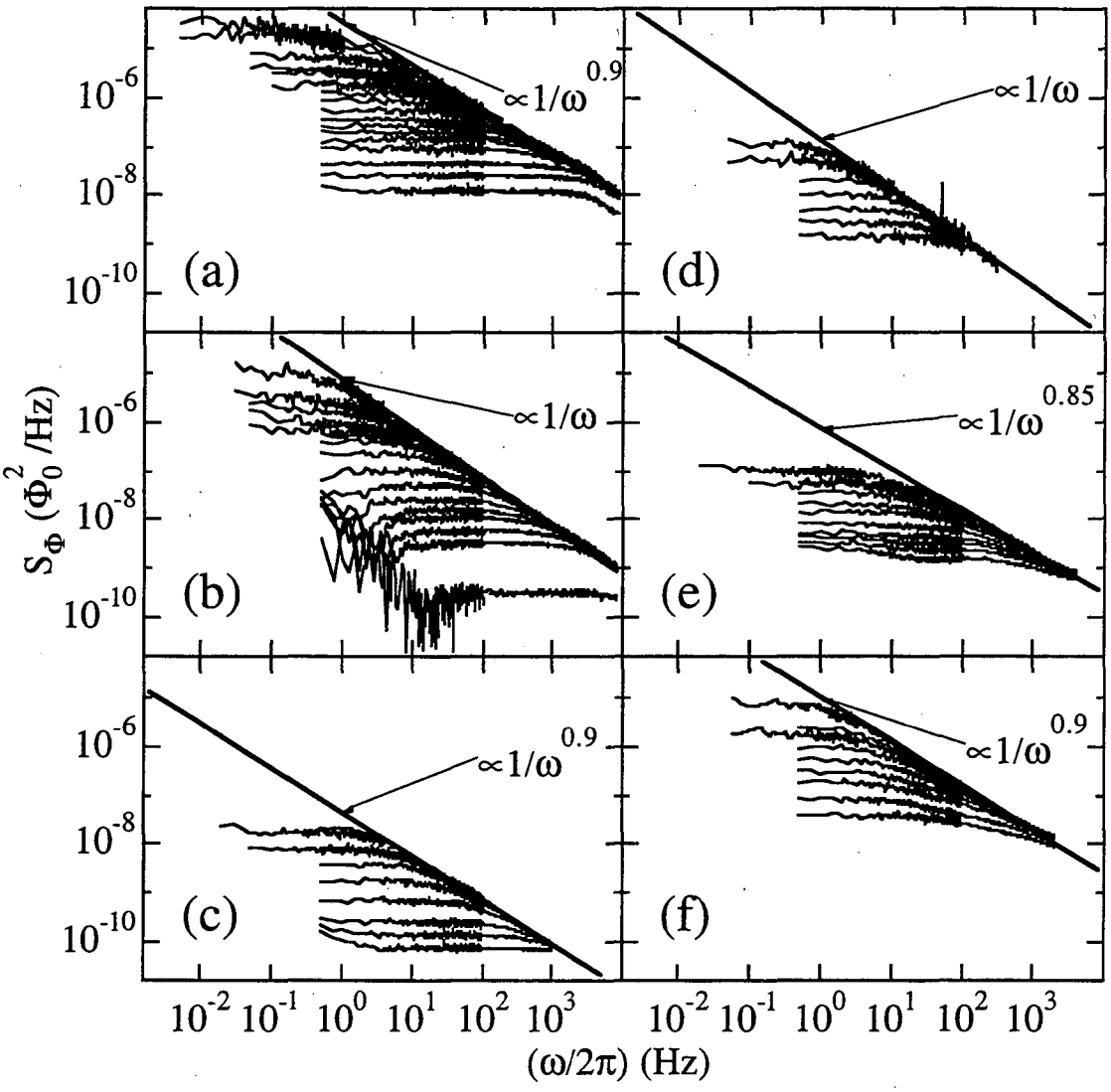

Figure 4.4: Spectral density of magnetic flux noise, $S_\Phi(\omega)$, versus frequency resulting from six measurements. The array and SQUID used, and the temperatures at which spectra were measured, are (a) array A using SQUID 1, T(K)=3.881, 3.901, 3.924, 3.954, 3.965, 3.980, 4.002, 4.025, 4.052, 4.089, 4.115, 4.151, 4.185, 4.249, 4.385, 4.499, and 4.721, (b) array B(1) using SQUID 1, T(K)=1.825, 1.857, 1.869, 1.885, 1.899, 1.906, 1.924, 1.956, 1.978, 2.010, 2.033, 2.054, 2.098, 2.146, and 2.379, (c) array B(2) using SQUID 2, T(K)=1.685, 1.698, 1.71, 1.725, 1.751, 1.783,1.810, and 1.848, (d) array B(3) using SQUID 3, T(K)=1.741, 1.758, 1.779, 1.797, 1.817, 1.837, and 1.857, (e) array B(4) using SQUID 1, T(K)=1.748, 1.767, 1.782, 1.801, 1.813, 1.841, 1.866, 1.884, 1.903, and 1.934, and (f) array C using SQUID 1, T(K)=3.158, 3.221, 3.246, 3.293, 3.349, 3.404, 3.467, 3.591, and 3.726. Smaller temperature corresponds to larger low frequency noise.

the low frequency portions of the higher temperature data are a result of subtraction of the SQUID noise. Figures 4.4(c) and 4.4(d) show $S_\Phi(\omega)$ of arrays B(2) and B(3), respectively, measured with SQUIDs 2 and 3 respectively, allowing the comparison of $S_\Phi(\omega)$ from array B measured with SQUIDs of three different geometries [Figs. 4.4(b) through 4.4(d)]. The sharp spikes in Fig. 4.4(d) are due to unusually large external noise sources, primarily at 60 Hz. In order to investigate the effects of array aging and/or different background magnetic fields, $S_\Phi(\omega)$ of array B [denoted as B(4) for this measurement] was remeasured with SQUID 1. The bumps in the low frequency portions of the highest temperature data are due to SQUID noise. Lastly, Fig. 4.4(f) shows $S_\Phi(\omega)$ of array C measured with SQUID 1 in order to allow the comparison of the results from two arrays with identical geometries, measured with the same SQUID, but with very different critical currents [Figs. 4.4(e) and 4.4(f)].

In general, the data have two similar features. First, at a given temperature the low-frequency noise is white and the high-frequency noise for different temperatures approaches or falls on the same curve, which has a frequency dependence of $1/\omega^\alpha$, where the exponent $\alpha \approx 1$. Second, in a given measurement, or equivalently figure, as temperature drops the white noise increases and the crossover frequency between the white and $1/\omega^\alpha$ behavior moves towards smaller frequency. used to make all the measurements In addition to the similarities mentioned above, there are some differences between the data from different measurements. First of all, the high frequency portion of the spectra does not have the same slope in the different measurements. Drawing a straight line through the $1/\omega^\alpha$ portion of the spectra for each set of data in Fig. 4.4 gives the slopes $\alpha = 0.9, 1, 0.9, 1, 0.85,$ and 0.9 for Figs. 4.4(a) through 4.4(f) respectively. Secondly, the data from different measurements are shifted vertically with respect to each other. In other words, at the temperature at which the crossover frequency reaches a specific value, the value of $S_\Phi(\omega = \omega_\xi)$ is different for different measurements.

4.3.3 Additional Evidence for a Phase Transition

Although the noise data presented above exhibited the characteristics of a phase transition via a characteristic frequency diverging towards zero for lowering temperatures, and the resistance dropped rapidly towards zero, there was additional evidence that the noise is indeed due to a superconducting phase transition. In addition to having zero resistance, one of the distinguishing characteristics of a superconductor is the ability to expel applied magnetic fields. One of the procedures in the noise measurements, as discussed in Section 2.1.1, was to measure the mutual inductance between the modulation coil and the SQUID, M_f, at each temperature before $S_\Phi(\omega)$ was measured. As discussed in Section 3.5, as the sample goes superconducting it decreases the mutual inductance between the sensor and the modulation coil. Therefore, by measuring M_f as a function of temperature it is possible to obtain a rough estimate of the temperature at which the sample becomes superconducting.

An example of this measurement is shown in Fig. 4.5, where M_f, normalized to the high-temperature value, is shown plotted versus temperature for arrays A and B(1). The solid symbols correspond to the results obtained from the technique for measuring R_f/M_f described in Section 2.1.3. The open symbols correspond to the results obtained by applying an external current to the modulation coil, with the feedback loop open, and monitoring the voltage output from the SQUID at the preamplifier output. The difference obviously means that the sample responds differently to pulsed than to slow changes in applied field, but we do not yet have an explanation for this behavior. From this figure, it is obvious that the array A starts to become superconducting somewhere between 3.6 and 3.8 K, and similarly array B(1) somewhere between 1.6 and 1.7 K. Therefore, it is reasonable to assume that the noise data of Figs. 4.4(a) and 4.4(b) are at temperatures above the superconducting transition (and by similarity that this is true for all the data of Fig. 4.4), and then turn to quantitative comparisons of the data with the theory of Section 4.2.

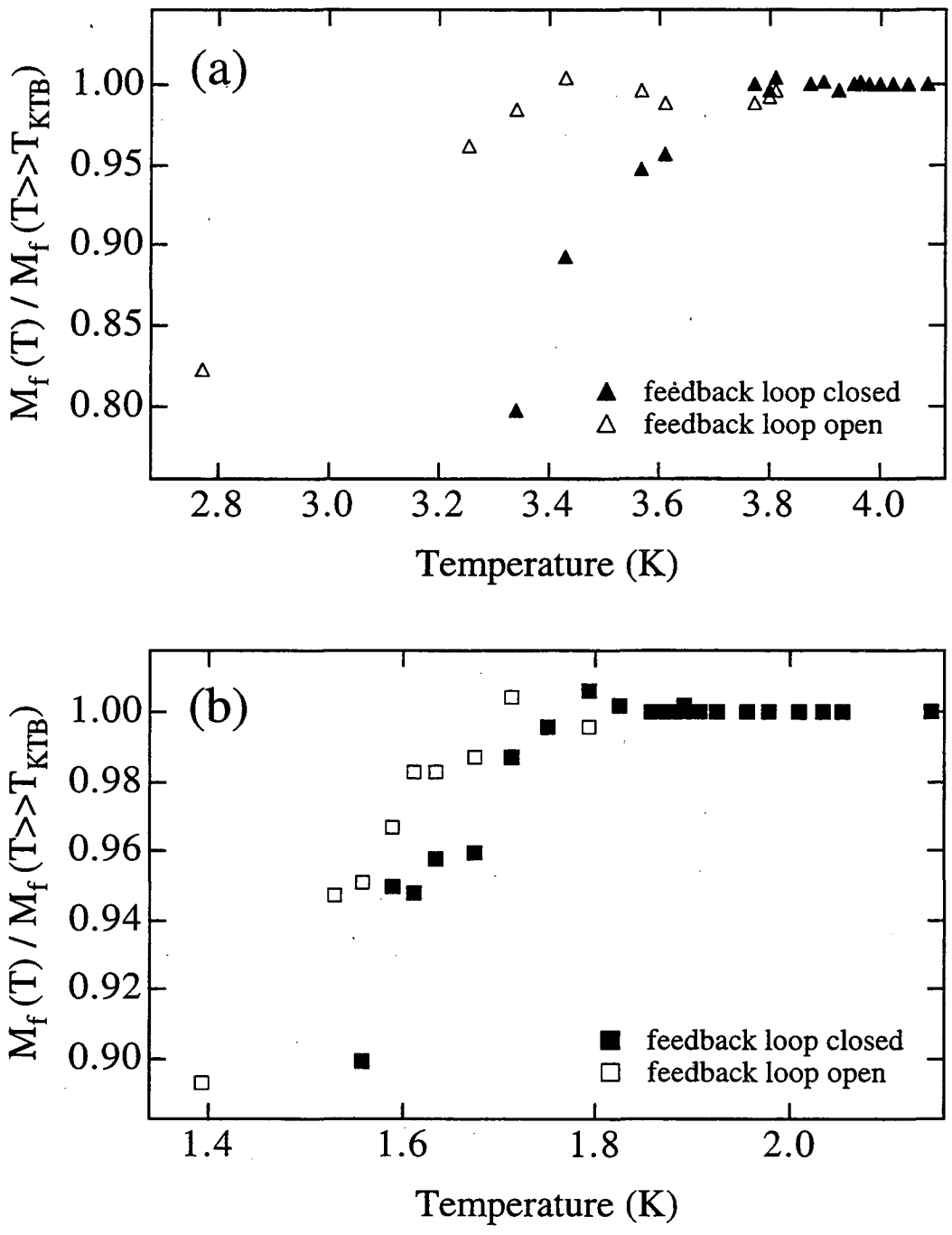

Figure 4.5: M_f, normalized to its high-temperature value, versus temperature for array for (a) array A and (b) array B(1).

4.4 Comparison of Data with Theory

Now that the features of the measured $S_\Phi(\omega)$ have been explained, let's compare these results to the predictions of Section 4.2, beginning by testing the general scaling behavior predicted by Eq. (4.14). As mentioned in Section 4.2, within this model there is good reason to believe that the scaling behavior is independent of any geometric parameters. However, to test this prediction it will suffice to first neglect the dependence on $\ell_{\rm eff}/\xi, d/\xi,$ and A/ξ^2 and then check if the measurements are consistent with this assumption. Therefore, ignoring for now any dependence on geometrical parameters, Eq. (4.14) predicts

$$\begin{aligned} \omega S_\Phi(\omega) &= \mathcal{F}_2(\omega/\omega_\xi) \\ &= \mathcal{F}_2\left(\frac{\omega}{\omega_0}\left(\frac{\xi}{\xi_0}\right)^z\right), \end{aligned} \tag{4.33}$$

where the second step follows from substituting for ω_ξ using the definition given in Eq. (4.12). Now, making use of the form of ξ relevant for Josephson junction arrays[12],

$$\xi = \xi_0 \exp\left(b/\sqrt{T' - T'_{\rm KTB}}\right), \tag{4.34}$$

where b is a constant, we substitute it in Eq. (4.33) to predict the scaling behavior

$$\omega S_\Phi(\omega) = \mathcal{F}_2\left(\frac{\omega}{\omega_0}\exp\left(bz/\sqrt{T' - T'_{\rm KTB}}\right)\right). \tag{4.35}$$

Equation (4.35) implies that, by choosing the correct values for $T_{\rm KTB}$ and bz and plotting $\omega S_\Phi(\omega)$ versus the scaled frequency $\omega \exp\left(bz/\sqrt{T' - T'_{\rm KTB}}\right)$, the raw data should collapse on to a single curve. To do so, T' was determined using Eqs. (4.31) for T' and (4.32) for $i_c(T)$ along with the parameters given in Table 4.1. Shown in Fig. 4.6 are the results of this procedure for the data shown in Fig. 4.4, and the fitting parameters bz and $T_{\rm KTB}$ used for each of the figures in Fig. 4.4 are given in Table 4.3. The letters correspond to those of Fig. 4.4. Recall that the scatter in the low frequency portion of Fig. 4.6(b) is due to subtraction of SQUID noise and the sharp spikes in Fig. 4.6(d) are due to spurious external noise. Overall, the data collapse fairly well, especially that of Figs. 4.4(b) and 4.4(d), justifying the prediction in Section 4.2 that $\mathcal{F}_2$ is independent of $\ell_{\rm eff}/\xi, d/\xi,$ and A/ξ^2.

For all of the arrays except for array B(3), for which the data did not span a large enough region of temperature, the quality of the data collapse is highly dependent on the choice of $T_{\rm KTB}$ but relatively weakly on the choice of bz. Increases (decreases) in bz for some

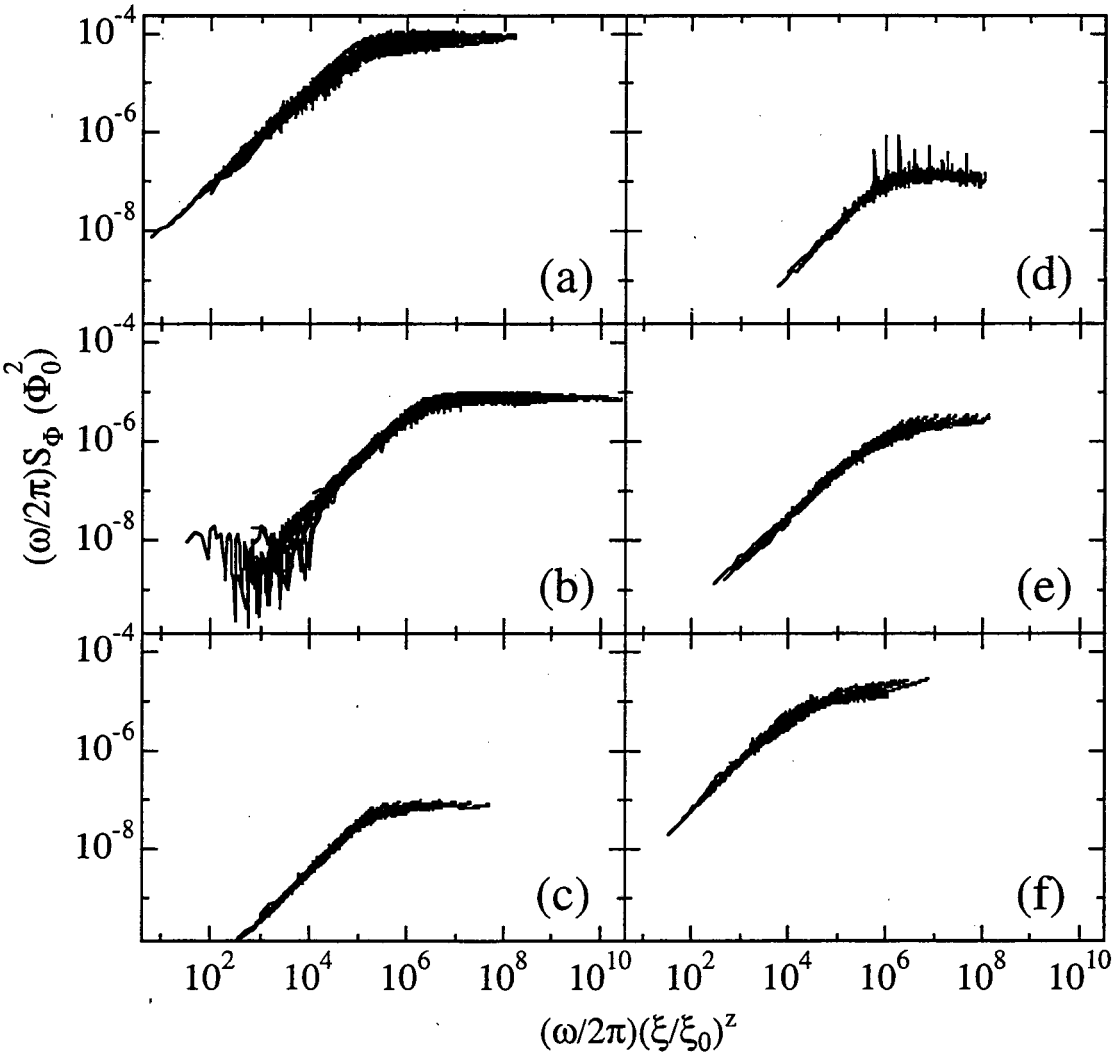

Figure 4.6: $(\omega/2\pi)S_\Phi(\omega)$ versus $(\omega/2\pi)(\xi/\xi_0)^z$; letters correspond to the raw data shown in Fig. 4.4. Extracted values of T_{KTB} and bz are given in Table 4.3.

Table 4.3: Results from data collapse of data shown in Fig. 4.4.

Array	Figure	T_{KTB} (K)	bz
A	4.6(a)	3.72 (3.68, 3.76)	1.7 (2.1, 1.6)
B(1)	4.6(b)	1.63 (1.56, 1.68)	3.8 (4.3, 3.3)
B(2)	4.6(c)	1.60 (1.58, 1.62)	2.1 (2.5, 1.7)
B(3)	4.6(d)	1.57 (0, 1.65)	4.1 (8.5, 2.5)
B(4)	4.6(e)	1.52 (1.46, 1.65)	3.4 (4.0, 2.0)
C	4.6(f)	2.85 (2.60, 2.96)	2.5 (3.5, 2.0)

range around the values listed in Table 4.3 could be compensated for by decreases (increases) of $T_{\rm KTB}$ to obtain a collapse of comparable quantity. However, changes in bz outside of this range could not be compensated for by changes in $T_{\rm KTB}$ and resulted in a lower quality data collapse. The spread in both bz and $T_{\rm KTB}$ that produced data collapses of comparable quality to those shown in Fig. 4.6 are given in Table 4.3 next to the optimal values. Smaller values of $T_{\rm KTB}$ required larger values of bz and the spreads in each are listed next to the optimal values as (min,max) and (max,min) pairs for $T_{\rm KTB}$ and bz respectively.

Although the data collapsed reasonably well, in agreement with the predicted KTB behavior, the high frequency portions of collapsed spectra at different temperatures in Figs. 4.6(a), 4.6(c), 4.6(e), and 4.6(f) do not lie on top of each other. On the other hand, all the spectra in Figs. 4.6(b) and 4.6(d) do lie on top of each other and the scatter is due to averaging only 200 times for the lowest frequency segments as mentioned above. The lack of a perfect collapse at high frequencies therefore resulted from the fact that $\alpha \neq 1$ for all the data.

Before dealing with the high-frequency behavior, let's compare the low-frequency predictions to the data. Beginning with Eq. (4.30) and substituting for ξ using Eq. (4.34) gives the predicted low-frequency behavior

$$S_\Phi(\omega \ll \omega_\xi) \equiv S_\Phi^w = \frac{\kappa F \Phi_0^2 T'^2}{16\pi^5 D}\xi_0^2 \exp\Big(2b/\sqrt{T' - T'_{\rm KTB}}\Big). \tag{4.36}$$

In order to test Eq. (4.36), the low-frequency noise, S_Φ^w, is defined as a horizontal line drawn through the frequency independent part of the noise spectra at each temperature in Fig. 4.4. Equation (4.36) then predicts that plotting $\ell{\rm n}(S_\Phi^w/T'^2)$ versus $1/\sqrt{T' - T'_{\rm KTB}}$, using $T_{\rm KTB}$ found from the data collapse, should produce a straight line of slope $2b$. Figures 4.7(a) and 4.7(b) show the results of this procedure for the data of Fig. 4.4, as well as straight line fits from which the values of $2b$ shown in Table 4.4 were extracted.

By comparing the values of bz from the data collapse, given in Table 4.3, with the extracted values of $2b$ in Table 4.4, it is evident that there is a large scatter in the value z and that the all the measurements would indicate that $z < 2$. However, since the data collapse did not determine bz very precisely, in order to provide a better estimate it can be extracted by using the temperature dependence of the characteristic frequency ω_ξ,

$$\omega_\xi = (D/\pi\xi_0^2)\exp\Big(-bz/\sqrt{T' - T'_{\rm KTB}}\Big), \tag{4.37}$$

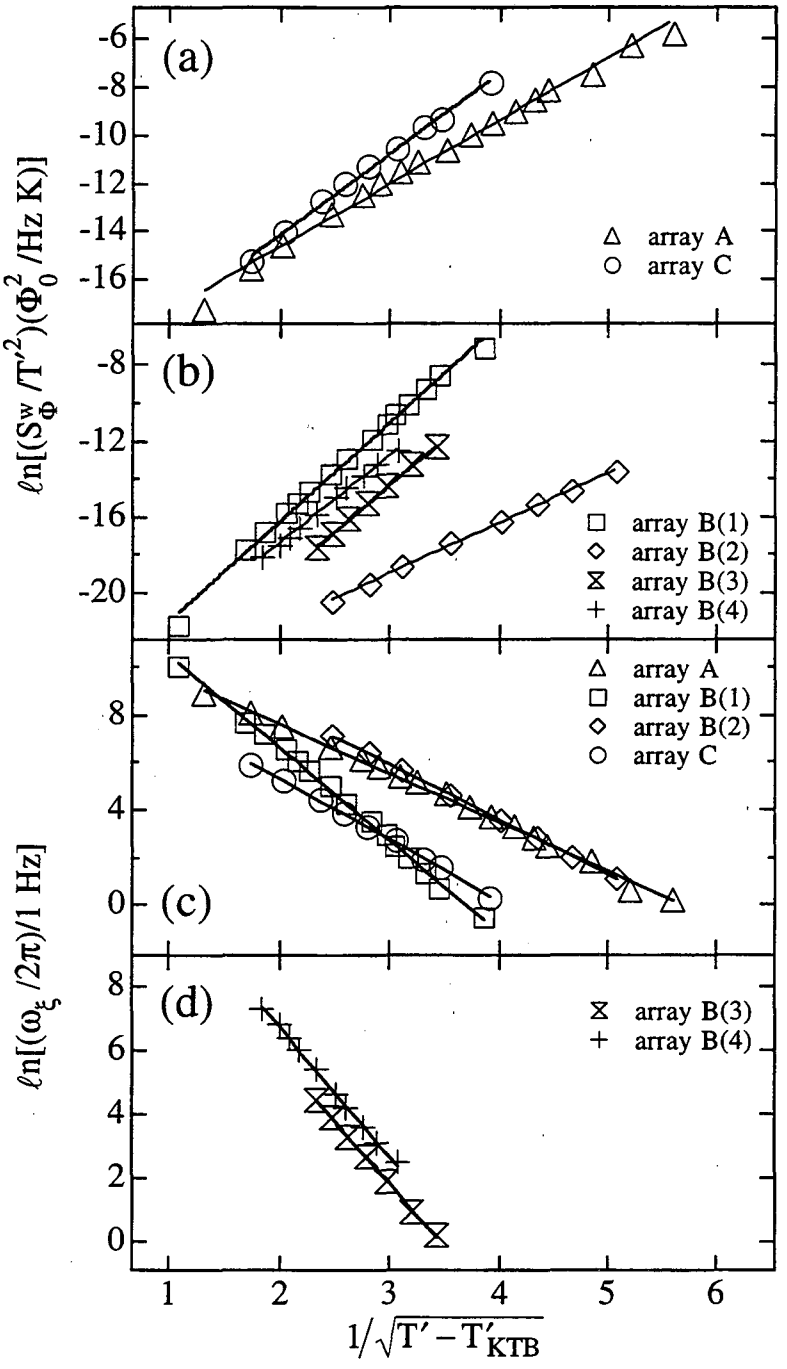

Figure 4.7: (a) and (b) $\ell n(S_\Phi^w/T'^2)$ versus $1/\sqrt{T'-T'_{KTB}}$ of the noise data shown in Fig. 4.4. Values of $2b$ extracted from the straight line fits shown are listed in Table 4.4. (c) and (d) $\ell n(\omega_\xi/2\pi)$ versus $1/\sqrt{T'-T'_{KTB}}$ of the noise data shown in Fig. 4.4. Values of bz extracted from the straight line fits shown are listed in Table 4.4

where ξ has been replaced using Eq. (4.34) and ω_0 using Eq. (4.27) in the definition of ω_ξ given by Eq. (4.12). The theory presented in Section 4.2 does not give an analytic formula for $S_\Phi(\omega)$ at all frequencies, so that ω_ξ cannot be determined by fitting to a specific functional form. However, since ω_ξ is the only characteristic frequency associated with the KTB transition, it is logical to define it as the frequency which separates the white and $1/\omega^\alpha$ behavior of the $S_\Phi(\omega)$ data shown in Fig. 4.4. To be more specific, ω_ξ will be defined as the intersection of the line defining S_Φ^w and the line proportional to $1/\omega^\alpha$ shown in each of the figures of Fig. 4.4. Equation (4.37) then predicts that plotting $\ell n(\omega_\xi/2\pi)$ versus $1/\sqrt{T' - T'_{\rm KTB}}$, using $T_{\rm KTB}$ obtained from the data collapse, should produce a straight line of slope $-bz$ and intercept $D/\pi\xi_0^2$. Figures 4.7(c) and 4.7(d) show the result of this procedure, and the extracted values of bz and $D/\pi\xi_0^2$ are shown in Table 4.4. These values of bz fall within the range of values that produced comparable data collapses given in Table 4.3. Also shown in Table 4.4 are the values of the dynamic critical exponent, z, calculated from the values of $2b$ and bz obtained from the temperature dependences of S_Φ^w and ω_ξ respectively.

There was a reasonably large spread in z over the six measurements, and all gave $z < 2$. However, the spread in z cannot be due to incorrectly chosen values of $T_{\rm KTB}$ or to inaccurate determinations of T' because the same scaling parameter, $1/\sqrt{T' - T'_{\rm KTB}}$, was used to extract both bz and $2b$. There are many possible explanations for the scatter in z as well as the fact that $z \neq 2$ as predicted by the model. The first is that the model is incorrect. This possibility will be dealt with in Section 4.5, but let's assume for now that the model is correct and look for explanations within the model.

Table 4.4: Parameters extracted from the KTB predictions for the scaling behavior of S_Φ^w and ω_ξ determined from the data shown in Fig. 4.4.

Array	$2b^a$	bz^b	z^c	$D/\pi\xi_0^2$ (Hz)
A	2.6(2)	2.1	1.6	8×10^5
B(1)	5.2	3.9	1.5	1×10^7
B(2)	2.6	2.3	1.8	3×10^6
B(3)	4.9	4.0	1.6	6×10^6
B(4)	4.7	4.0	1.7	2×10^7
C	3.4	2.6	1.5	2×10^5

[a] extracted from the temperature dependence of S_Φ^w
[b] extracted from temperature dependence of ω_ξ
[c] calculated using the values for $2b$ and bz shown here

One possible explanation is that the characteristic frequency, ω_ξ, was not defined correctly. As mentioned above, ω_ξ cannot be determined by fitting $S_\Phi(\omega)$ to a specific functional form and the definition as the intersection of the $1/\omega^\alpha$ line and the line defining S_Φ^w might not be correct. However, since ω_ξ in the theory marks a separation between two different types of vortex dynamics and the only such observable feature in $S_\Phi(\omega)$ is the crossover between white and $1/\omega^\alpha$ behavior, this definition is likely a good one. Another possibility can be seen by returning to the scaling behavior prediction of Eq. (4.33). The low-frequency noise is frequency independent, which means that the function $\mathcal{F}_2(\omega/\omega_\xi)$ must have the form

$$\lim_{\omega \to 0} \mathcal{F}_2(\omega/\omega_\xi) \propto (\omega/\omega_\xi)$$

or

$$S_\Phi^w \propto \xi^z, \tag{4.38}$$

where the last step follows from the definition of $\mathcal{F}_2(\omega/\omega_\xi)$ in Eq. (4.33). Therefore, comparing Eq. (4.38) to the low-frequency prediction of Eq. (4.30) indicates that the dynamic critical exponent is determined by the equation

$$\xi^z \propto T'^2 \xi^2. \tag{4.39}$$

This is clearly incorrect because z cannot depend explicitly on T'. The discrepancy arises because an implicit assumption in scaling theory is that, close enough to the phase transition, the temperature dependence of the correlation length is so strong that, as far as any explicit dependence of the system's properties on T' [such as T'^2 in Eq. (4.30)] is concerned, T' is essentially a constant. However, for the measurements presented above, due to the strong temperature dependence of the Josephson coupling energy [see Eq. (4.31)], T' varies reasonably strongly over the temperature range for which the data in Fig. 4.4 were measured, as shown in Fig. 4.8. This leads to the question of whether the scaling theory predictions, and more generally the KTB theory, are valid for the measurements presented in Section 4.3. This will be covered in more detail in Section 4.5, but first let's return to the high-frequency behavior of the measured noise in order to address the issue that $\alpha \neq 1$ as mentioned earlier.

In order to examine the high-frequency behavior in more detail, let's return to the prediction of Eq. (4.29) and examine only the frequency dependence. Substituting Eq. (4.22)

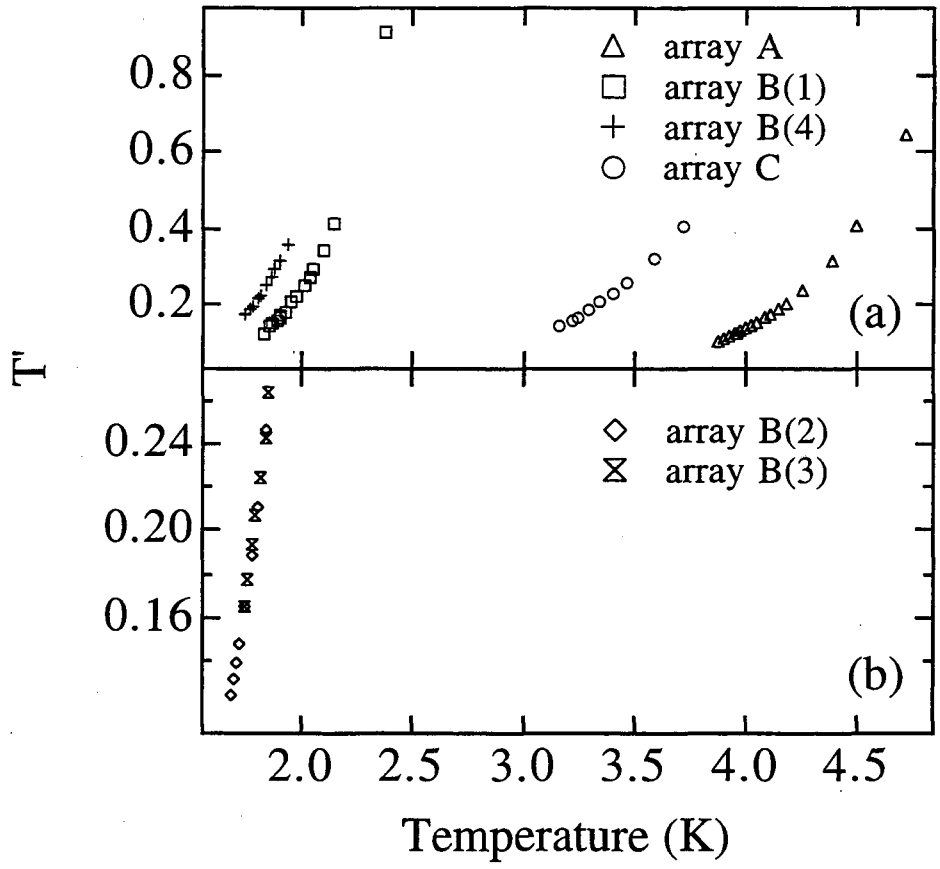

Figure 4.8: T' versus temperature, calculated for the temperatures at which $S_\Phi(\omega)$ was measured in Fig. 4.4, using Eq. (4.31) and the parameters for $i_c(T)$ given in Table 4.1.

for r_ω in to Eq. (4.29) predicts the frequency dependence

$$S_\Phi(\omega \gg \omega_\xi) \propto \left[\omega \ell n^2 \left(\frac{14D}{\omega r_0^2}\right)\right]^{-1}$$
$$= \left[\omega \ell n^2 \left(\frac{14\pi\xi_0^2}{r_0^2}\frac{\omega_0}{\omega}\right)\right]^{-1}, \qquad (4.40)$$

where the last step follows from expressing the diffusion constant D in terms of the definition of ω_0 given in Eq. (4.27). To illustrate this, shown in Fig. 4.9(a) is a plot of $S_\Phi(\omega \gg \omega_\xi)$ versus $\omega/C\omega_0$, where the constant $C \equiv 14\pi\xi_0^2/r_0^2$ and for concreteness the value has been set such that $C\omega_0 = 10^6$ rad/s. For the present purposes, the relevant aspect of Eq. (4.40) is the slope on a log-log plot, $\partial \log[S_\Phi(\omega)]/\partial \log(\omega)$, which is shown in Fig. 4.9(b) as a function of $\omega/C\omega_0$. It is evident that the slope approaches -1 only for frequencies $\omega \ll C\omega_0$. In fact, the slope does not reach -0.9 until $\omega/C\omega_0 \approx 4\times10^{-12}$. Since the values of ω_0 extracted from the temperature dependence of ω_ξ shown in Table 4.3 ranged from approximately 2×10^5 to 2×10^7, the theoretical prediction of Eq. (4.40) demands physically unlikely values of ξ_0 and/or r_0. For example, choosing $\omega/C\omega_0 \approx 4 \times 10^{-12}$ (the value where $S_\Phi(\omega) \propto 1/\omega^{0.9}$, and letting $\omega_0 = 2 \times 10^6$, in the middle of the values extracted from the data, Eq. (4.9) then demands that $r_0/\xi_0 \lesssim 2 \times 10^{-4}$.

Values for r_0 and ξ_0 satisfying $r_0/\xi_0 \lesssim 2 \times 10^{-4}$ are unlikely, but not impossible. It is important to note that there is no reason to believe that r_0 is of order of the lattice spacing. The reason is that r_0 is probably best pictured as the smallest allowable separation of a vortex-antivortex pair, and in a Josephson junction array it is possible to have a pair with a separation of less than one lattice spacing. Lobb *et al.*[12] showed by numerical calculation that, at low temperatures (much below $T_{\rm KTB}$), a vortex centered at a point in between two neighboring superconducting islands has a different (higher) energy state than a vortex centered between the islands forming a unit cell. This is shown schematically in Fig. 4.10, where a vortex which moves from position A to position C has to cross an energy barrier at position B, $E_{\rm barrier} \equiv E_B - E_A \approx 0.2E_J$. A similar calculation for a triangular lattice found an energy barrier $E_{\rm barrier} \approx 0.043E_J$. Now, when dealing with vortices on length scales smaller than the lattice spacing it is, in principle, necessary to take into account these energy barriers which form what is commonly called the egg-carton potential of the array. However, since at the temperatures where $S_\Phi(\omega)$ was measured $k_BT \gtrsim E_{\rm barrier}$ (or equivalently $T' \gtrsim E_{\rm barrier}/E_J(T)$ as shown in Fig. 4.8), the egg-carton potential is washed out and it is reasonable to treat the array as a flat potential. Then, the important point is

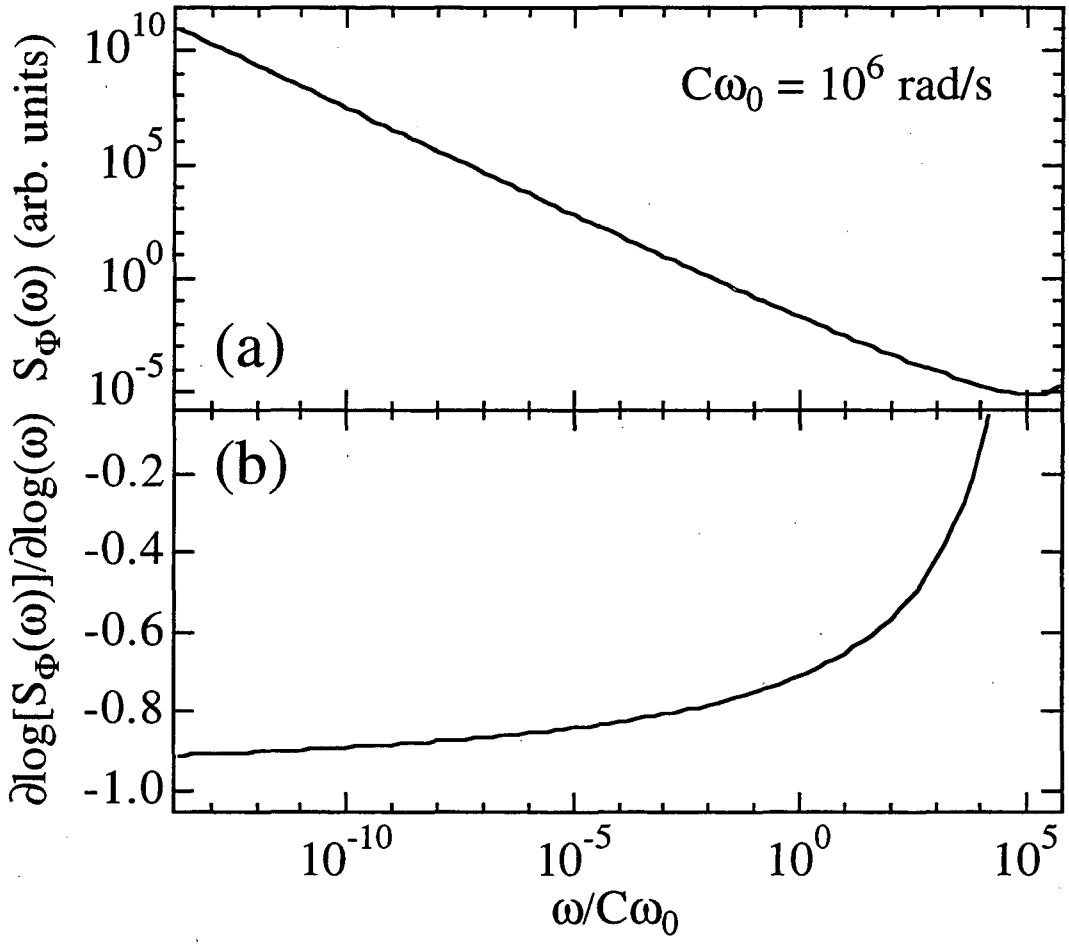

Figure 4.9: (a) $S_\Phi(\omega)$ versus frequency according to Eq. (4.40) with the assumption $C\omega_0 = 10^6$ rad/s. (b) Slope of $S_\Phi(\omega)$ from part (a) as a function of frequency.

that a vortex with a center away from the cell center is a well-defined object and therefore it is possible that r_0 is much smaller than the lattice spacing.

On the other hand, it is generally accepted that ξ_0 is of order of the lattice spacing because ξ should never be smaller than the lattice spacing. In other words, an average of one free vortex per unit cell gives an average phase shift of 2π integrated around the cell, which for a square lattice gives an average phase shift between neighboring islands of $\pi/2$ and via the Josephson relation, $i = i_c \sin(\theta = \pi/2)$, an average current equal to the critical current. Since it is energetically unfavorable to have a current between neighboring islands which is greater than the critical current, one concludes that ξ must always be larger than the lattice spacing.

In the measurements presented in Section 4.3, there was no direct measurement of ξ. However, it is possible to determine the range over which ξ varied. Shown in Fig. 4.11(a) is a plot of ξ/ξ_0 versus temperature for each of the measurements shown in Fig. 4.4, calculated using the values of T_{KTB} and $2b$ given in Table 4.4. For some of the measurements, ξ varied by as much as two orders of magnitude. In general one would expect that ξ is smaller than the smallest dimension of the array and larger than the lattice size. Shown in Fig. 4.11(b)

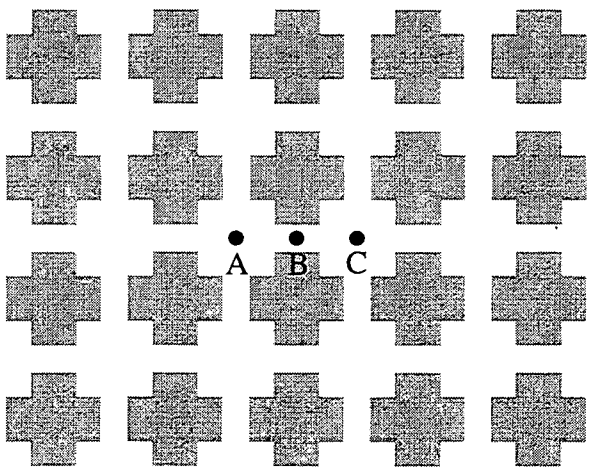

Figure 4.10: Illustration of a vortex moving from the center of an array cell at position A to the center of the adjacent cell at position C while crossing the energy barrier at position B.

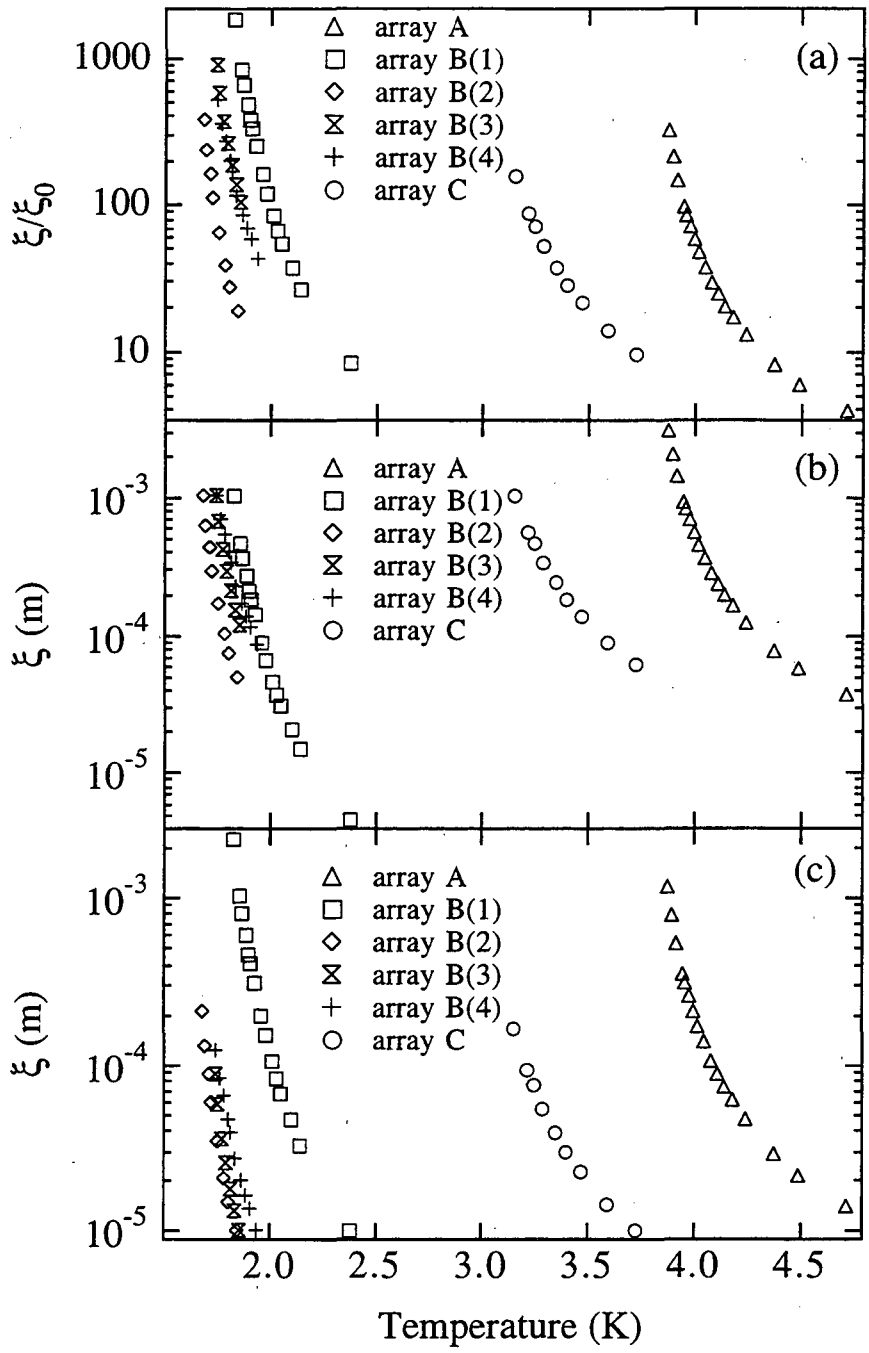

Figure 4.11: (a) ξ/ξ_0 versus temperature for each of the experimental runs for which data are shown in Fig. 4.4, calculated from Eq. (4.34) and using the parameters given in Table 4.4 for $2b$ and the parameters for $i_c(T)$ given in Table 4.1. (b) ξ versus temperature calculated from part (a) above and assuming that ξ was equal to the smallest dimension of the array at the lowest temperature. (c) ξ versus temperature calculated from part (a) above and assuming that $\xi = a$ at the highest temperature.

is a plot of ξ versus temperature assuming that, at the lowest temperature for which $S_\Phi(\omega)$ was measured, ξ was equal to the smaller dimension of the array, and Fig. 4.11(c) shows a similar plot under the assumption that, at the highest temperature for which $S_\Phi(\omega)$ was measured, ξ was equal to the lattice size. Listed in Table 4.5 are the values of ξ_0 resulting from the assumptions associated with Fig. 4.11. For all the measurements except for those on array B(1), ξ remained within the bounds stated above, and even for array B(1) ξ did not span such a large range that it would have been much larger than the smaller dimension of the array or much smaller than the lattice size.

Further evidence that the correlation length fell in the range $a \lesssim \xi \lesssim$(smallest array dimension) can be seen by examining Figs. 4.12 and 4.13. Figure 4.12(a) shows four spectra measured on array B(1) at $T = 1.750$ K. First, a measurement from $0.4 - 100$ Hz was made, followed by one from $10 - 4000$ Hz, and then this was repeated. Each of the two measurements with the same bandwidth are identical within the scatter, indicating that the measurements provided a true thermodynamic average [note that this temperature is above T_{KTB} for array B(1)]. However, shown in Fig. 4.13(b) are four individual time traces of the data used to calculate the $0.4-100$ Hz spectra, two taken from the first spectra and two from the second. A close examination reveals that there are sharp jumps in the flux threading the sensor as a function of time $\Phi(t)$, reminiscent of random telegraph signals often seen in high-temperature superconductors[16]. These sharp jumps can be understood by realizing that when ξ is of order of the width of the sensor, there is an average of only one free vortex under it so that at times only one vortex moves from (or to) the area under the sensor and causes a sudden jump in $\Phi(t)$.

Table 4.5: Values of ξ_0 resulting from the assumptions leading to Figs. 4.11 and 4.20

Array	ξ_0 μm[a]	ξ_0 μm[b]	ξ_0 μm[c]
A	10	4	100
B(1)	0.6	1	50
B(2)	3	0.5	10
B(3)	1	0.1	1
B(4)	2	0.2	9
C	6	1	40

[a] assuming that $\xi \leq$ smallest array dimension
[b] assuming that $\xi \geq a$
[c] assuming that $\xi \geq \ell_{\mathrm{eff}}$

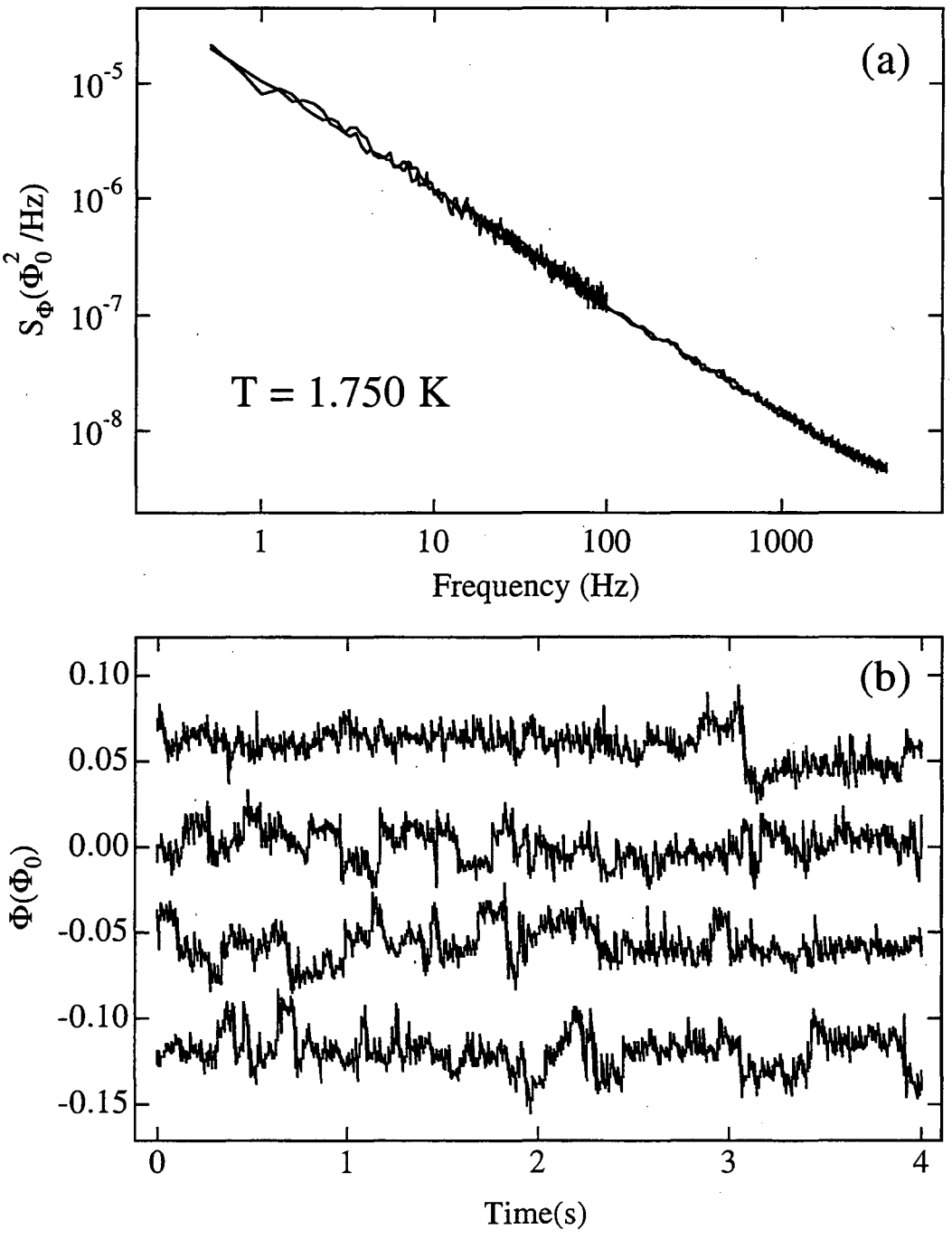

Figure 4.12: (a) Four sets of noise spectra measured at $T = 1.750$ K on array B(1), measured in the chronological order $0.4 - 100$ Hz, $10 - 4000$ Hz, $0.4 - 100$ Hz, and $10 - 4000$ Hz. (b) Flux versus time traces taken during the $0.4 - 100$ Hz measurements of (a). The traces are offset vertically for clarity and the top two were from the first measurement and the bottom two from the second.

These sudden jumps in $\Phi(t)$ could also be interpreted as caused by vortices hopping within the egg-carton potential of the array if the sample were at a temperature below T_{KTB}. However, the mutual inductance measurement presented in Section 4.3 indicated that 1.75 K $> T_{\mathrm{KTB}}$. Further evidence that this is the case, and that the transition temperature $T_{\mathrm{KTB}} = 1.63$ K extracted from the data collapse is reasonably accurate is provided in Fig. 4.13, which shows the identical set of measurements as described for Fig. 4.12. The time traces shown in Fig. 4.13(b) show similar jumps in $\Phi(t)$ as those of Fig. 4.12(b). However, the top two time traces, taken during the first $0.4 - 100$ Hz measurement are distinctly different than the bottom two, taken during the second. The likely cause for this behavior is that below T_{KTB} the array is superconducting, but there are still vortex-antivortex pairs of finite separation created which can be pinned in the egg-carton potential of the array. In this way, at some time there is a configuration of vortices and antivortices hopping in the array which changes on a reasonably slow time scale so that the noise measurements do not provide a true thermodynamic average of the system, as evidenced by the spectra shown in Fig. 4.13 where the $10 - 4000$ Hz spectra taken at different times are distinctly different. Presumably, if one averaged for a long enough time, spectra measured at different times would be identical because all possible system states would be probed. For obvious practical considerations, and to ensure a finite time until my graduation, this was not done.

Given the above arguments, it is likely that ξ_0 is of the order of the lattice size and likely that r_0 is considerably smaller than the lattice size. However, a more important point is that according to Fig. 4.9(b) and Eq. (4.40), the slope of $S_\Phi(\omega)$ approaches -1 very slowly as a function of decreasing $\omega/C\omega_0$. Even allowing for very small values of r_0, it is extremely unlikely that the experimental data shown in Fig. 4.4 for which $\alpha = -1$ can be described by the predictions of Eq. (4.29).

Now that it has been established that the theoretical predictions of Section 4.2 cannot explain the high-frequency part of the measured data and also that there is a question of whether the KTB scaling theory predictions are valid when T' varies reasonably strongly over the temperature range where data was measured, it is necessary to ask whether it is valid to apply the KTB predictions to the data.

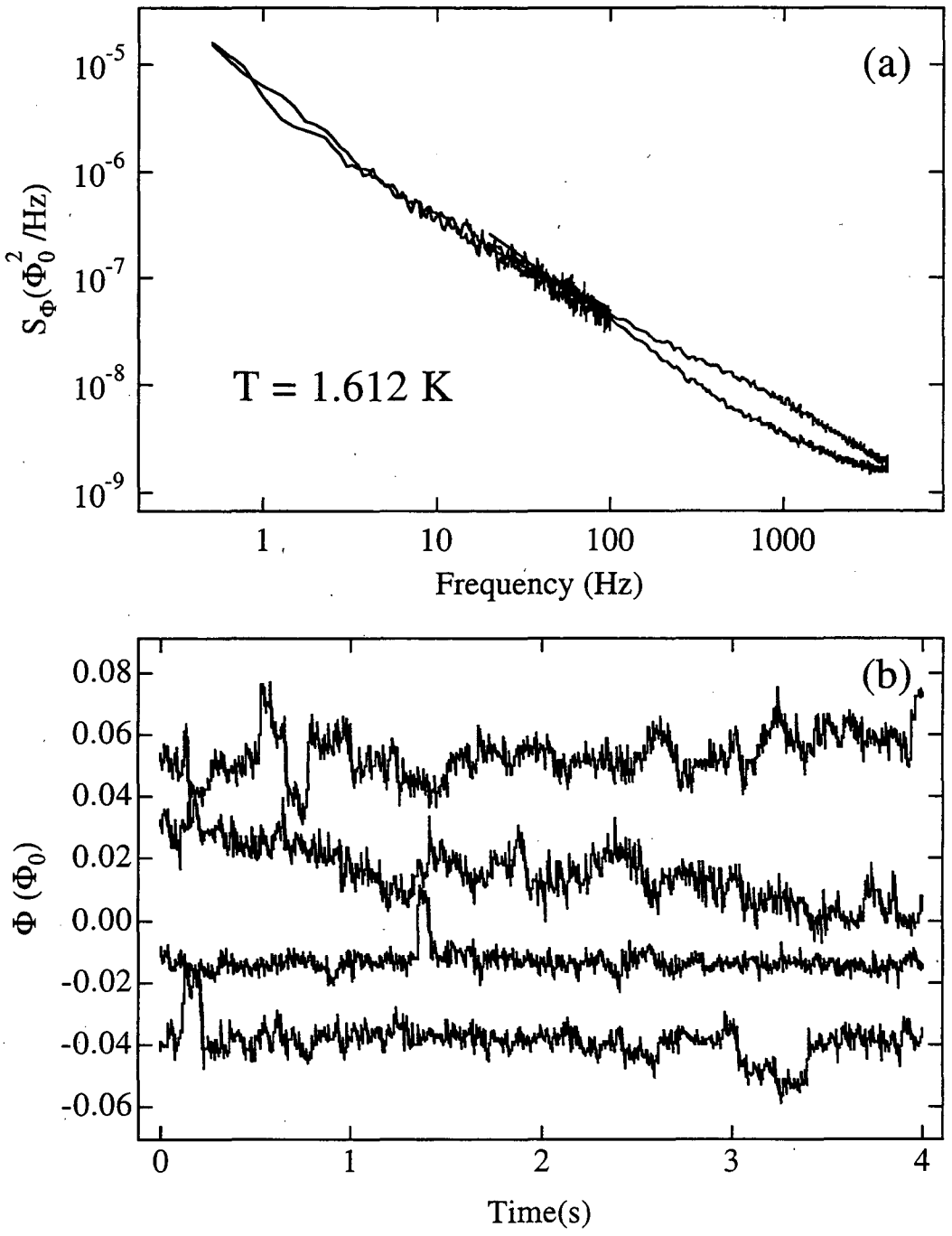

Figure 4.13: (a) Four sets of noise spectra measured at $T = 1.612$ K on array B(1), measured in the chronological order $0.4 - 100$ Hz, $10 - 4000$ Hz, $0.4 - 100$ Hz, and $10 - 4000$ Hz. (b) Flux versus time traces taken during the $0.4 - 100$ Hz measurements of (a). The traces are offset vertically for clarity and the top two were from the first measurement and the bottom two from the second.

4.5 Applicability of the KTB Predictions

According to the KTB theory, the value of T' at the transition temperature is determined by the equation

$$T'_{\mathrm{KTB}} = \frac{k_B T_{\mathrm{KTB}}}{E_J(T_{\mathrm{KTB}})} = \frac{\pi}{2\epsilon_c}. \tag{4.41}$$

The precise value of ϵ_c is not known because it depends on the chemical potential, or energy needed to create a vortex-antivortex pair of the minimum allowable separation, of the system. Smaller chemical potentials make pair creation more favorable and thereby a larger vortex density near the transition, which translates to a smaller value of T'_{KTB} and a larger value of ϵ_c. Several authors have argued[65, 66, 67, 68, 69] that for small enough chemical potential the transition becomes first order while others[70, 68] found no evidence of a first-order transition even at very small chemical potential, and to date there has been no experimental evidence for a first-order transition.

As mentioned in Section 4.4, the minimum possible vortex pair separation, r_0, in these arrays might be much smaller than the lattice spacing, and this would give a smaller value of the chemical potential and thereby a larger value of ϵ_c. The value of ϵ_c for the measurements presented in Section 4.3 can be inferred by solving Eq. (4.41) for ϵ_c and then using the values for T_{KTB} given in Table 4.4 to calculate T'_{KTB} using Eq. (4.31) and the parameters for $i_c(T)$ given in Table 4.1. The results are shown in Table 4.6, along with the (min,max) values calculated from the spreads in T_{KTB} from Table 4.3. The values ranged from 19 to 29 (excluding the ∞ for array B(3) which resulted from the noise data not covering a large enough range of temperature to determine T_{KTB} accurately), which is consistent with having a small value of r_0 and therefore a small chemical potential.

However, this determination of ϵ_c relies on the measurements of i_c as discussed in Section 4.3, which might not have been the best method. The reason can be seen by examining Fig. 4.14, which shows $\ell n(i_c)$ versus temperature, where the temperatures at which $S_\Phi(\omega)$ was measured are indicated by vertical lines with arrows to the right indicating the lowest temperature at which $S_\Phi(\omega)$ was measured and vice-versa for arrows to the left. In other words, the critical current measurements indicated that $i_c \neq 0$ at some of the temperatures above T_{KTB}. One must keep in mind that the critical current was measured at a frequency of 47 Hz, so that one would expect a non-zero critical current at temperatures above the zero frequency T_{KTB}. Since the true transition temperature is determined by the

Table 4.6: Values of T'_{KTB} and ϵ_c for the measurements presented in Section 4.3. T'_{KTB} was calculated using Eq. (4.31) and the value of T_{KTB} from Table 4.3, and from these ϵ_c was calculated using Eq. (4.41). The spreads in T'_{KTB} and ϵ_c due to the spreads in T_{KTB} listed in Table 4.3 are given in parentheses.

Array	T'_{KTB}	ϵ_c
A	$7 \times 10^{-2}(7 \times 10^{-2}, 8 \times 10^{-2})$	$22(23, 20)$
B(1)	$5 \times 10^{-2}(4 \times 10^{-2}, 7 \times 10^{-2})$	$29(23, 39)$
B(2)	$8 \times 10^{-2}(7 \times 10^{-2}, 8 \times 10^{-2})$	$19(20, 17)$
B(3)	$8 \times 10^{-2}(0, 1 \times 10^{-1})$	$19(\infty, 13)$
B(4)	$7 \times 10^{-2}(5 \times 10^{-2}, 1 \times 10^{-1})$	$23(31, 13)$
A	$8 \times 10^{-2}(7 \times 10^{-2}, 8 \times 10^{-2})$	$20(23, 20)$

condition $\omega_\xi = 0$, one can similarly define a finite-frequency transition temperature $T_{\mathrm{KTB}}(\omega)$ by the condition $\omega_\xi = \omega$. Shown in Fig. 4.14 by solid symbols (note that these are not measured values of i_c) are the temperatures at which $\omega_\xi = 2\pi 47$ rad sec^{-1} for each of the noise measurements of Fig. 4.4. At least for arrays A and B(2), there was a measurable critical current at temperature well above $T_{\mathrm{KTB}}(47\ \mathrm{Hz})$ when one would have expected the critical current to approach zero rapidly above this temperature. However, other measurements have shown a critical current above T_{KTB}[48, 55] and the majority of measurements of the non-linear current-voltage characteristics exhibited an exponent $V \propto I^{a(T)}$ at low currents, where $a(T) = 3$ was used to define T_{KTB}. Above T_{KTB}, $a(T)$ gradually decreased from 3 to 1[47, 52, 53, 54, 57], and $a(T) > 1$ implies a maximum in dV/dI at a non-zero current since the arrays must become ohmic at high currents. Therefore, the non-zero critical currents at temperatures above $T_{\mathrm{KTB}}(47\ \mathrm{Hz})$ shown in Fig. 4.14 are consistent with previous studies and likely reflect the rounding of the arrays' current-voltage characteristics due to fluctuations.

More troubling than the large values of ϵ_c is the general assumption of the KTB theory that that the scaling parameter $(T' - T'_{\mathrm{KTB}})/T'_{\mathrm{KTB}} \ll 1$ in order for the renormalization group calculations to be valid. However, most experimental measurements observed behavior consistent with the KTB predictions over a much wider temperature range[48, 58, 55, 57]. In the measurements presented in Section 4.3, $(T' - T'_{\mathrm{KTB}})/T'_{\mathrm{KTB}} \gtrsim 1$ as shown in Fig. 4.15. As far as the measurements presented here are concerned, it is not possible to determine exactly why the data obeyed the KTB scaling predictions in this temperature range. Nevertheless, this is the experimental result and the challenge is then to develop a theoretical model to

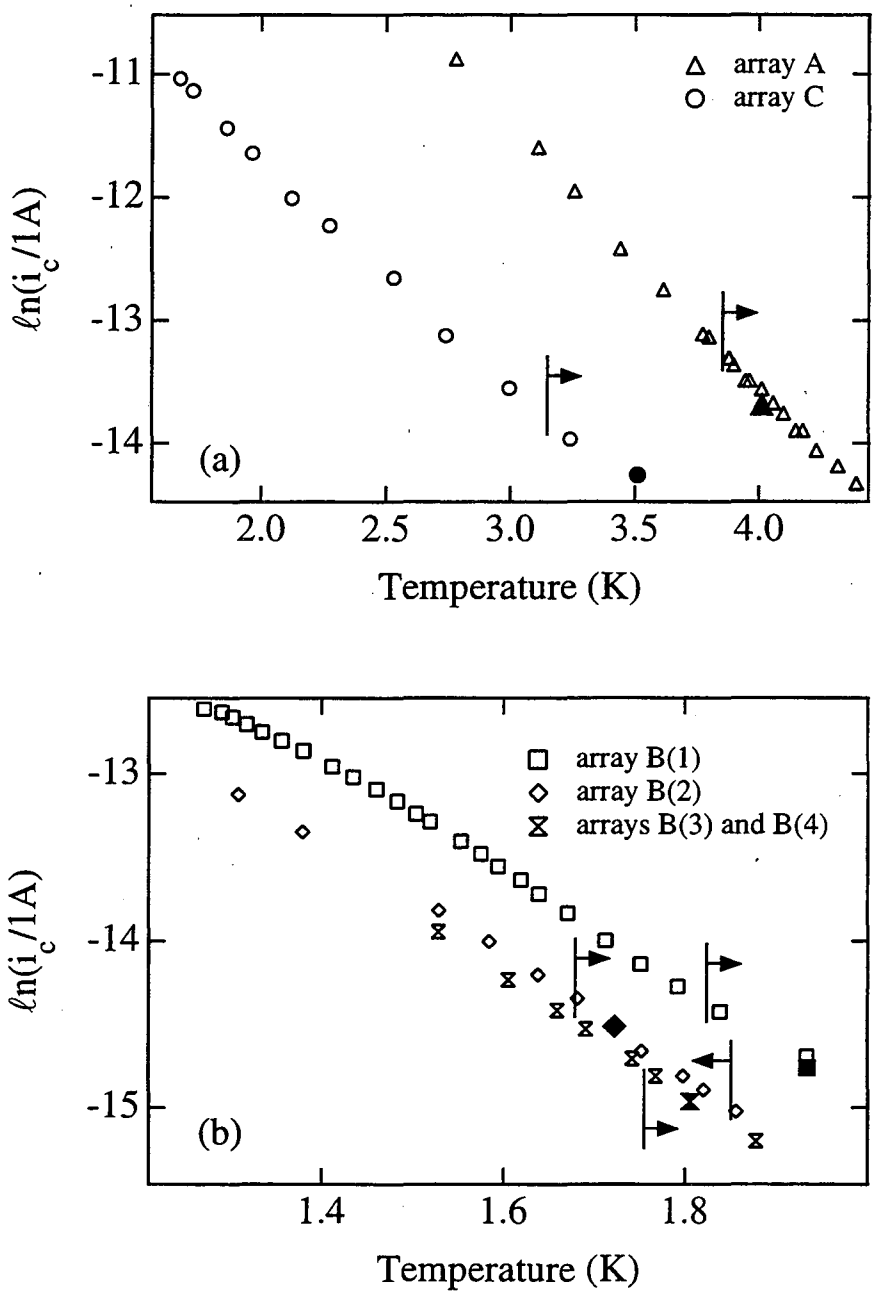

Figure 4.14: i_c versus temperature for the measurements shown in Fig. 4.4, showing the temperatures at which $S_\Phi(\omega)$ was measured as well as the temperature at which $\omega_\xi = 2\pi 47$ rad sec^{-1}. See text for detailed description.

account for this behavior. Minnhagen[67] proposed that scaling behavior observed over this large temperature range is due to a more general Coulomb gas scaling than to the KTB predictions. In addition, one could argue that in this temperature range it is difficult to distinguish between the KTB behavior and that of other models, and these possibilities will be discussed in the following section.

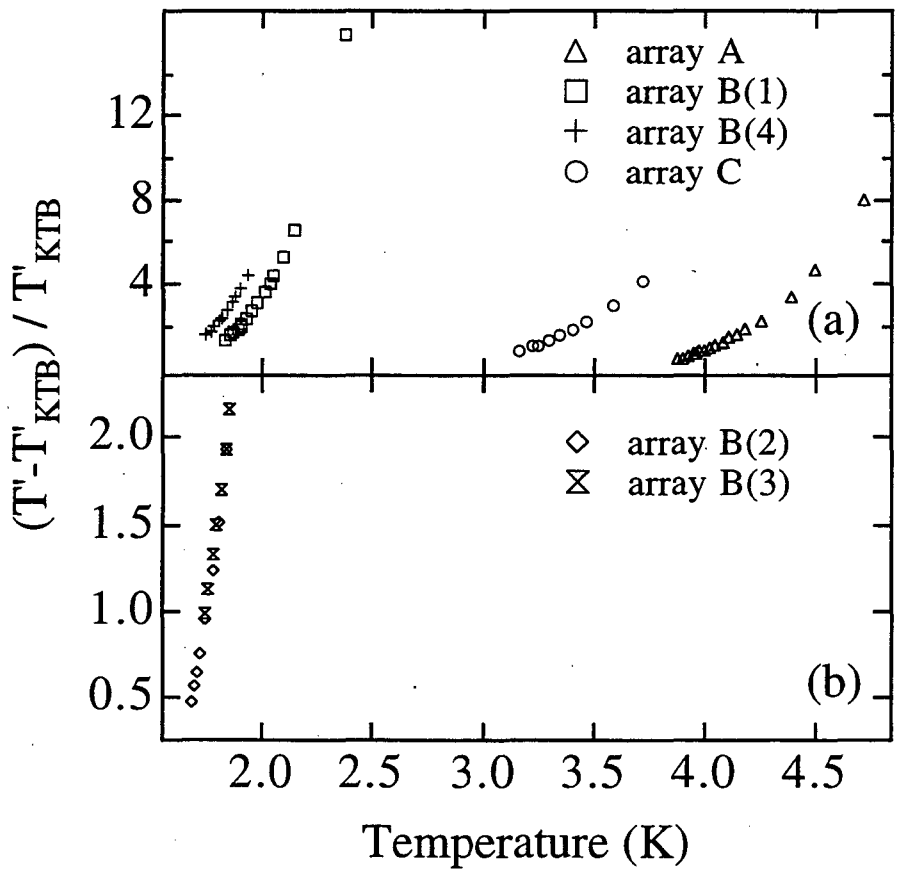

Figure 4.15: $(T'-T'_{\mathrm{KTB}})/T'_{\mathrm{KTB}}$ versus temperature, calculated for the temperatures at which $S_\Phi(\omega)$ was measured in Fig. 4.4, using Eq. (4.31) and the parameters for $i_c(T)$ given in Table 4.1

4.6 Other Explanations for the Noise Data

There have been many attempts to describe the vortex dynamics associated with the two-dimensional superfluid/superfluid transition as mentioned in Section 4.1. For the purpose of this thesis, only a small number which are possible candidates to explain the measurements presented in Section 4.3 will be discussed. Those theories and simulations which predict only a $1/\omega^{3/2}$ or $1/\omega^2$ noise behavior at high frequencies[46, 71, 72], with no intermediate $1/\omega$ region, are cited merely for completeness. However, it is important to point out that theories which predict a $1/\omega$ region and a crossover to $1/\omega^{3/2}$- or $1/\omega^2$-behavior are not inconsistent with the measurements (as will be discussed below). The reason is that the arrays must have a crossover to $1/\omega^{\alpha>1}$-behavior at some frequency so that the noise integrated over all frequencies is finite.

This section will first discuss the possibility that the flux noise was caused by vortex hopping within the egg-carton potential of the array, not because it is a likely explanation of the measurements but rather to demonstrate that it is not. Next, two analytic theories will be discussed, one of which gave results nearly identical to those of Section 4.4. Lastly, the results of two numerical simulations will be presented.

4.6.1 Vortex Hopping

The small values of $T'_{\rm KTB}$, and therefore large values of ϵ_c, discussed in the previous section leads us to ask the important question of whether, for all the measurements presented in Section 4.3, $T' < T'_{\rm KTB}$. If indeed this were the case, one could argue that the vortices were hopping around within the egg-carton potential of the array via thermal activation which would have given a characteristic frequency with the thermally-activated behavior[73]

$$\begin{aligned} \omega_{\rm hop} &\equiv \omega_{0,\rm hop} \exp[-C_J E_J(T)/k_B T] = \omega_\xi \\ &= \omega_{0,\rm hop} \exp[-C_J/T'], \end{aligned} \tag{4.42}$$

where the constant C_J depends on the array geometry. Recall from Section 4.4 that for an array with uniform E_J's, $C_J \approx 0.2$ for square arrays and $C_J \approx 0.043$ for triangular arrays. However, it is likely that there was some variation in E_J across the array and therefore C_J was determined by the largest energy barrier. To examine this possibility, shown in Figs. 4.16(a) and 4.16(b) are plots of the same data of Fig. 4.7, with ω_ξ renamed $\omega_{\rm hop}$, except that the horizontal axis is $1/T'$. The fits to $\ell n(\omega_\xi/2\pi)$ versus $1/T'$ shown as straight lines in

the figure gave the values for $\omega_{0,\mathrm{hop}}$ and C_J listed in Table 4.6.1. As is evident, the values for $\omega_{0,\mathrm{hop}}$ are not unreasonable and the values for C_J are larger than one would expect, but as mentioned above the arrays were likely somewhat non-uniform. What is more striking is that, within the scatter, the values of C_J for the triangular and square arrays are comparable. Since, as mentioned above, the energy barrier is approximately 47 times larger in a square array than in a triangular array (for a given E_J of course), it is extremely unlikely that thermally-activated vortex hopping could explain the temperature dependence of ω_ξ.

Table 4.7: Parameters extracted from the data of Fig. 4.16 using Eq. 4.42

Array	$\omega_{0,\mathrm{hop}}$ (rad/s)	C_J
A	9×10^3	1.0
B(1)	2×10^4	1.5
B(2)	1×10^5	1.5
B(3)	2×104	1.9
B(4)	2×10^4	1.6
A	1×10^3	1.2

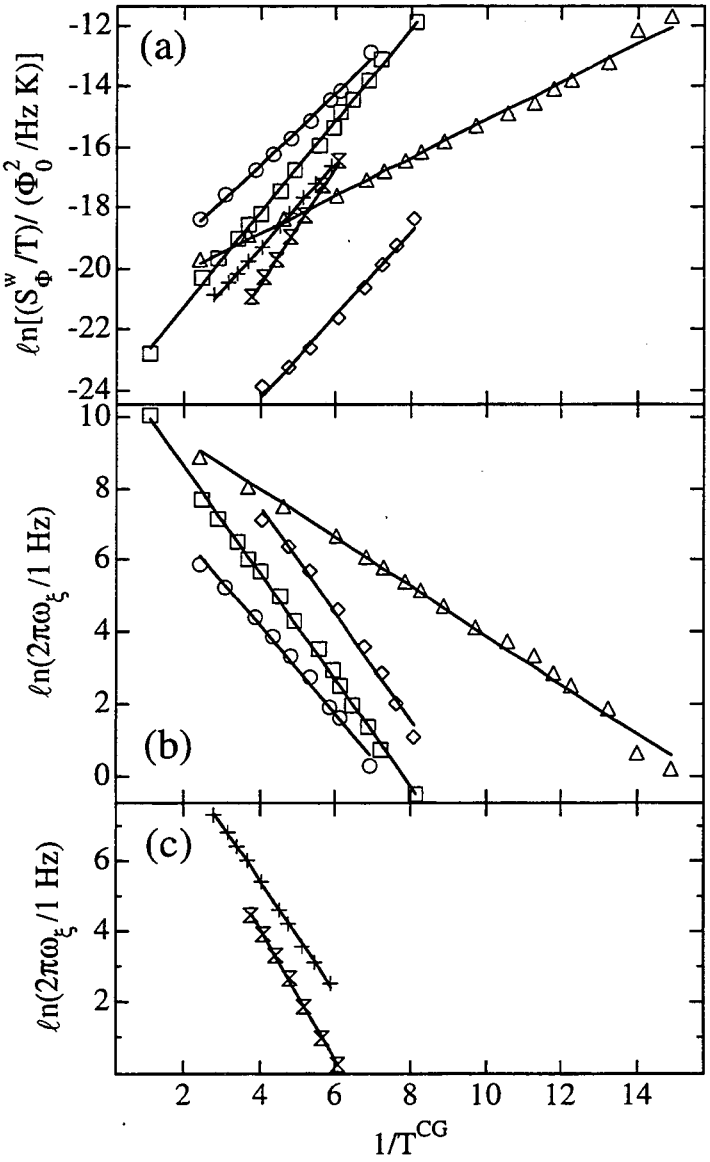

Figure 4.16: (a) $\ell n(S_\Phi^w/T)$ versus $1/T'$ for the noise data of Fig. 4.4. (b) and (c) $\ell n(\omega_\xi/2\pi)$ versus $1/T'$ for the noise data shown in Fig. 4.4.

4.6.2 Regime Interpretation

In a recent publication[74], a model was proposed to explain vortex dynamics in two-dimensional superconductors in terms of a regime interpretation based on the ratio $Y = (r_\omega/\xi)^2 \equiv \Gamma_0/\omega\xi^2$, where r_ω is identical to the definition of Eq. (4.22) with $14D$ replaced by a junction-determined phase diffusion rate, Γ_0. The calculation is rather detailed, so only an outline of the relevant ideas and the results will be quoted here.

Beginning with a Langevin equation essentially identical to Eq. (4.65), the authors calculated the complex vortex conductivity $\sigma(\omega) = \sigma_1(\omega) + i\sigma_2(\omega)$. The most important steps were that the Hamiltonian was decomposed into spin wave and vortex parts and a gaussian approximation was made so that the Josephson sinusoidal coupling was replaced with $(\theta_i - \theta_j)^2$. This approximation amounts to a long-wavelength approximation. In addition, it was assumed that the dynamic critical exponent $z = 2$.

Before giving the results, it will useful to relate the complex conductivity to $S_\Phi(\omega)$ via the relation[61]

$$S_\Phi(\omega) = \frac{2\Phi_0^2 T'}{\omega} \left| Im\left(\frac{1}{\epsilon(\omega)}\right)\right|, \tag{4.43}$$

as well as the relation between the dielectric constant and the complex conductivity[67],

$$\frac{1}{\sigma(\omega)} = -i\omega L_k \epsilon(\omega), \tag{4.44}$$

where $L_k = \Phi_0^2/4\pi^2 E_J$ is the kinetic inductance[12]. The result is

$$S_\Phi(\omega) = \frac{\Phi_0^4 T'}{2\pi^2 E_J}\sigma_1(\omega), \tag{4.45}$$

so that only the dissipative part of $\sigma(\omega)$ is needed to calculate the flux noise as expected.

Capezzali *et al.* found three different results for $\sigma_1(\omega)$ which depended on the value of Y, which were

$$\frac{\sigma_1(\omega)}{\sigma_0\xi^2} = \frac{T'_{\ell_\xi}}{[1 + (\Gamma_0^2/\omega^2\xi^4)^{-1}]} \qquad Y \gg 1 \tag{4.46a}$$

$$= \frac{2T'_{\ell_\omega}\ell n(\Gamma_0/\omega\xi^2)}{\pi[1 - (\Gamma_0^2/\omega^2\xi^4)^{-1}]} \qquad Y \lesssim 1 \tag{4.46b}$$

$$= -\frac{dT'_{\ell_\omega}}{d\ell_\omega}\frac{\arctan(\omega\xi^2/\Gamma_0)}{2(\omega\xi^2/\Gamma_0)} \qquad Y \ll 1, \tag{4.46c}$$

where σ_0 is a conductivity scale, $\ell_\xi \equiv \ell n(\xi/r_0)$, $\ell_\omega \equiv \ell n(r_\omega/r_0)$, and T'_ℓ is the renormalized KTB coupling strength E_J/k_BT evaluated at the length ℓ. In the regime $Y \ll 1$, $T'_{\ell_\omega} \approx$

$T'_\infty + \ell^{-1}$ and for $Y \lesssim 1$, Cappezali *et al.* claim that $T'_{\ell_\omega} \approx T'_0$, so that Eqs. (4.46a) and (4.46b) are easily evaluated. In the regime $Y \gg 1$, in order to achieve the correct result $\sigma_1 \propto \xi^2$ it is necessary that T'_{ℓ_ξ} be independent of ξ in contrast to the result of Waganblast and Fazio quoted in Section 4.6.3 who claimed that $T'_{\ell_\xi} \propto \xi^4$. Therefore, using these results in Eqs. (4.46) and then substituting for $\sigma_1(\omega)$ in Eq. (4.45) one finds the final results for $S_\Phi(\omega)$

$$S_\Phi(\omega) = \frac{\Phi_0^4 T' \sigma_0}{2\pi^2 E_J} \frac{K_{\ell_\xi} \ell n(\Gamma_0/\omega\xi^2)\xi^2}{[1 + (\Gamma_0^2/\omega^2\xi^4)^{-1}]} \qquad Y \gg 1 \qquad (4.47a)$$

$$= \frac{\Phi_0^4 T' \sigma_0}{\pi^3 E_J} \frac{K_{\ell_\omega} \ell n(\Gamma_0/\omega\xi^2)\xi^2}{[1 - (\Gamma_0^2/\omega^2\xi^4)^{-1}]} \qquad Y \lesssim 1 \qquad (4.47b)$$

$$= \frac{\Phi_0^4 T' \sigma_0 \Gamma_0}{4\pi^2 E_J} \frac{\arctan(\omega\xi^2/\Gamma_0)}{\omega \ell n^2(r_\omega/r_0)} \qquad Y \ll 1. \qquad (4.47c)$$

Note that Eqs. (4.47a) and (4.47c) predict essentially the same behavior for $S_\Phi(\omega)$ as the calculations presented in Section 4.2, including the logarithmic correction to $1/\omega$ behavior at high frequency. It is difficult to determine if the data of Section 4.3 exhibit the behavior predicted by Eq. (4.47b) in the intermediate frequency regime because it is likely that this regime is very narrow. It is somewhat surprising that two very different calculations give similar results for the flux noise, but this agreement lends support to each. Since the weaknesses of these predictions were discussed in detail in Section 4.4, they will not be repeated here.

4.6.3 XY Model with Local Damping

Wagenblast and Fazio[2] developed a model for the vortex dynamics based on the two-dimensional XY model with the additional assumption that, at each site, the phase fluctuations are damped. They speculated that this damping is ohmic and due to coupling of the superconducting islands to the normal metal underneath. Then, in order to calculate the flux noise, they used a two-step procedure by first calculating the contribution due to free vortices using a Debye-Hückel approximation and then taking into account the physics at length scales smaller than ξ by means of a renormalization of the coupling constants. The method was similar to that used by Berker and Nelson[75] to calculate the specific heat and superfluid density above T'_{KTB}. For details of the calculation, see Ref. [2], as only the results and underlying assumptions will be discussed here.

Beginning with the Euclidean action for the system with ohmic damping and performing a Villain transformation to obtain the dynamic action for the vortices, the authors arrived at the expression for the flux noise due to the free vortices

$$S_{\Phi}^{\mathrm{DH}} = K\Phi_0^2 \frac{T'}{8\pi^3}\left(\frac{\ell_{\mathrm{eff}}}{\xi}\right)^4 \frac{1}{\omega}\mathcal{F}_4\left(\frac{\omega}{\omega_\xi}\frac{4\pi\xi^2}{\ell_{\mathrm{eff}}^2}\right), \tag{4.48}$$

where K is a constant determined by the geometry of the measurement apparatus and F_4 is a scaling function given by

$$\mathcal{F}_4\left(x=\frac{\omega}{\omega_\xi}, y=\frac{4\pi\xi^2}{\ell_{\mathrm{eff}}^2}\right) = -Im\int_0^y dw\left(1+w\frac{w-ix}{w-2ix}\right)^{-1}. \tag{4.49}$$

In these expressions, $\omega_\xi = \omega_{\mathrm{ld}}(\xi_0/\xi)^2$, $\omega_{\mathrm{ld}} = 2\pi E_J/(\xi_0^2\hbar\alpha_R)$, and $\alpha_R = R_Q/R$ where $R_Q = h/4e^2$ is the resistance quantum and R is the shunt resistance between each island and the underlying copper. Shown in Fig. 4.17 is a plot of the scaling function $\mathcal{F}_4$ versus ω/ω_ξ with $4\pi\xi^2/\ell_{\mathrm{eff}}^2 = 10^7$. Since the flux noise is proportional to $\omega\mathcal{F}_4$, it is evident that the prediction gives white noise for $\omega/\omega_\xi < 1$, a crossover to $1/\omega$ behavior for $1 < \omega/\omega_\xi < 4\pi\xi^2/\ell_{\mathrm{eff}}^2$, and finally a crossover to $1/\omega^2$ behavior for $\omega/\omega_\xi > 4\pi\xi^2/\ell_{\mathrm{eff}}^2$.

In order to take into account the effect of bound pairs up to separations of order of the the correlation length, the authors used the scaling relation

$$S_\Phi(\omega, \ell_{\mathrm{eff}}, T') = \mathrm{e}^{z\zeta} S_\Phi(\omega \mathrm{e}^{z\zeta}, \ell_{\mathrm{eff}}\mathrm{e}^{-\zeta}, T'(\zeta)). \tag{4.50}$$

The scaling was then carried out to $\zeta^* = \ell n(\xi/\xi_0)$ and substituted in to Eq. (4.49) to give

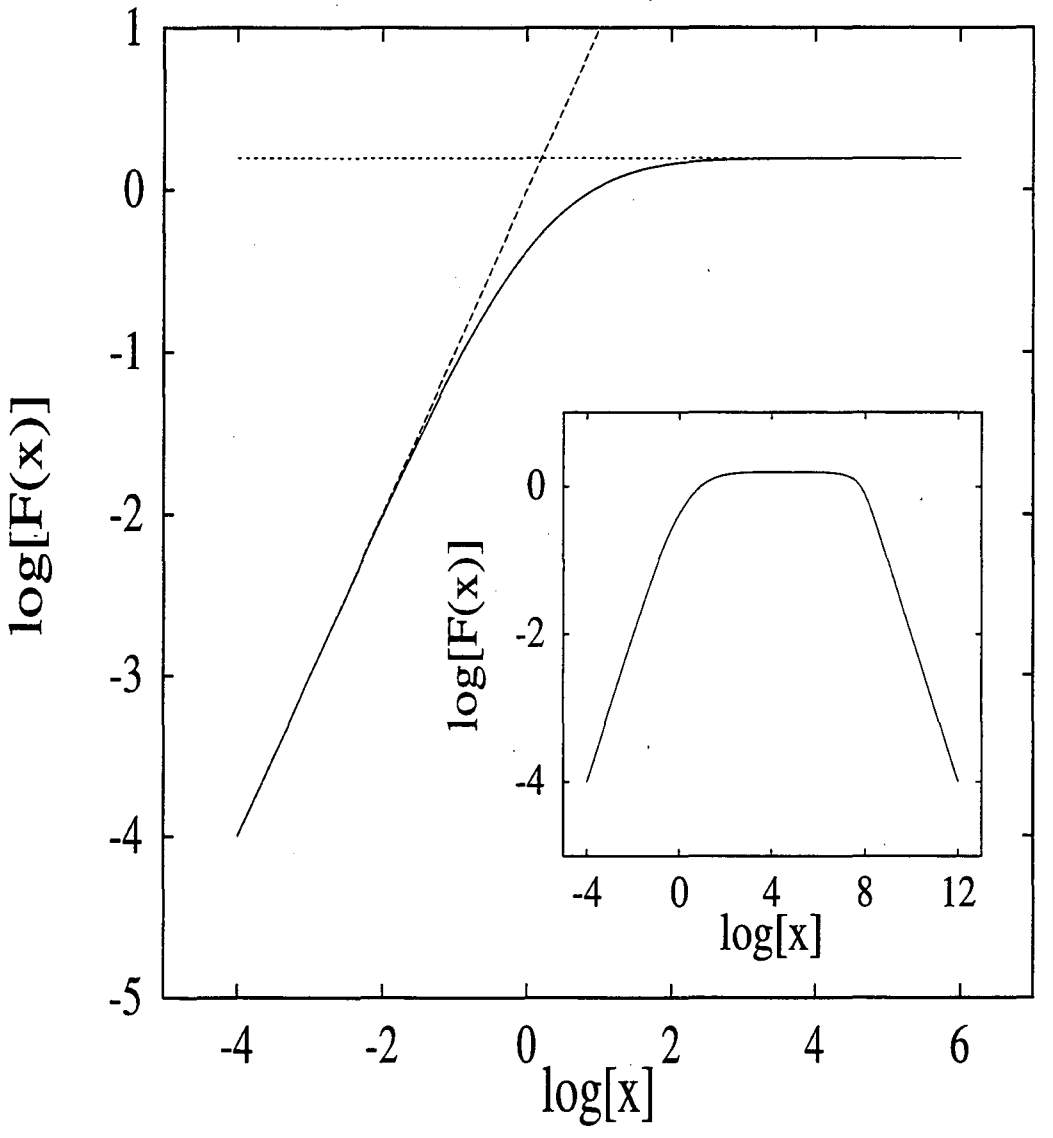

Figure 4.17: Scaling function $\mathcal{F}_4$ of Eq. (4.49) as a function of $x \equiv \omega/\omega_\xi$ for $4\pi\xi^2/\ell_{\text{eff}}^2 = 10^7$, illustrating the crossover at $x = 1$. The inset shows the same scaling function with an expanded horizontal axis in order to show a second crossover at $x = 4\pi\xi^2/\ell_{\text{eff}}^2$. Figure taken with permission from Ref. [2]

the final expression

$$S_\Phi(\omega) = K\Phi_0^2 \frac{\ell_{\text{eff}}^4}{8\pi^3} \frac{T'(\zeta^*)}{\xi^4} \frac{1}{\omega} \mathcal{F}_4 \left(x = \frac{\omega}{\omega_\xi}, y = \frac{4\pi\xi^2}{\ell_{\text{eff}}^2} \right). \tag{4.51}$$

As can be seen by examining Eq. (4.51) and Fig. 4.17, a necessary condition for the prediction to agree with the measured noise is that $T'(\zeta^*)/\xi^4$ is temperature independent. As an attempt to justify this, the authors begin with the Kosterlitz renormalization group equations

$$\frac{dT'(\zeta)}{d\zeta} = 4\pi^3 y^2(\zeta) + \mathcal{O}(y^4) \tag{4.52a}$$

and

$$\frac{dy(\zeta)}{d\zeta} = \left[2 - \frac{\pi}{T'}\right] y(\zeta) + \mathcal{O}(y^4). \tag{4.52b}$$

A numerical iteration of Eqs. (4.52) with the initial conditions $T'(0) = \pi/0.9$ (10% above the transition temperature) and $y(0) = \mathrm{e}^{-2/T'(0)}$ is shown in Fig. 4.18, from which it can be seen that the scaling behavior of T' approaches the behavior $T'(\zeta) \propto \mathrm{e}^{4\zeta}$. Since the scaling is carried out to $\zeta^* = \ell n(\xi/\xi_0)$, the result is that $T'(\zeta^*)/\xi^4$ is indeed temperature independent. However, as shown in Fig. 4.18(b), even at $\zeta = 2$ the fugacity $y(2) \gg 1$ so that higher order terms in y for the RG equations will become important and Eqs. (4.52) are no longer valid. In fact, the ξ/ξ_0 plot of Fig. 4.11(a) indicates that $1.5 \lesssim \zeta \lesssim 7$. However, if it is assumed that $T'(\zeta^*)/\xi^4$ is temperature independent, the results for the behavior of $S_\Phi(\omega)$ are as shown in Fig. 4.19. The similarity to the noise data of Fig. 4.4 is striking, but the requirement that $T'(\zeta^*)/\xi^4$ be temperature independent is only a hypothesis and has not been rigorously justified.

Also, as is evident from Fig. 4.17 and as mentioned earlier, the theory predicts $1/\omega$-behavior only for $\omega_{\text{ld}}(\xi_0^2/\xi^2) < \omega < 4\pi\omega_{\text{ld}}(\xi_0^2/\ell_{\text{eff}}^2)$ and a crossover to $1/\omega^2$-behavior for $\omega > 4\pi\omega_{\text{ld}}(\xi_0^2/\ell_{\text{eff}}^2)$. This means that to have an appreciable region of $1/\omega$-behavior, the correlation length must be much larger than the effective diameter of the sensor. Shown in Fig. 4.20 is a plot similar to that of Fig. 4.11, using Fig. 4.11(a) for the temperature dependence of ξ/ξ_0 and with the assumption that $\xi > \ell_{\text{eff}}$ at the highest temperature for each of the curves. The values of ξ_0 resulting from this assumption are listed in Table 4.5. Since ξ_0 is expected to be of order of the lattice size as mentioned in Section 4.4, the values shown in Table 4.5 are not unreasonable. What is more surprising is that for all of the data

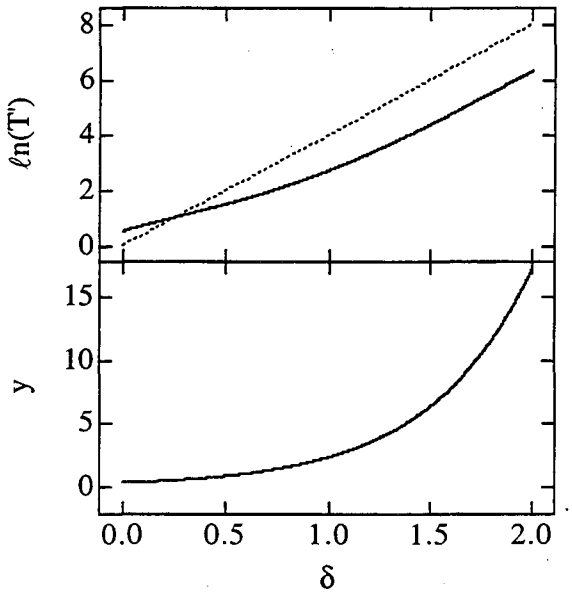

Figure 4.18: Results for the numerical integration of the KT scaling relations given by Eqs. (4.52).

sets, except that for array B(3), ξ exceeded the smaller dimension of the array and for some of the measurements even exceeded the larger dimension of the array. Although it is not impossible that ξ follows the KTB scaling form when is is larger than one or both dimensions of the array, in general one would expect to see finite size effects in this case.

A feature of this theory which does not appear in the measurements is a crossover to $1/\omega^2$-behavior. However, it is possible that this frequency,

$$\begin{aligned} \omega_{\text{cut,ld}} \equiv & 4\pi\omega_{\text{ld}}(\xi_0^2/\ell_{\text{eff}}^2) \\ = & \frac{16\pi e^2 E_J R}{\hbar^2}\frac{a^2}{\ell_{\text{eff}}^2}, \end{aligned} \tag{4.53}$$

lies outside of the experimental bandwidth. Since all the parameters of Eq. (4.53) are known except for the shunt resistance R, is is possible to make an upper bound on $\omega_{\text{cut,ld}}$ by letting $R = r_n$. Shown in Fig. 4.21(a) is a plot of $\omega_{\text{cut,ld}}$ versus temperature calculated from Eq. (4.53) and using the values of E_J calculated from the measured critical currents just as was done in Section 4.4. By comparing the values of $\omega_{\text{cut,ld}}$ to the highest measurement frequencies in Fig. 4.4, one would expect that for arrays A and B(1) the crossover to $1/\omega^2$-behavior should have appeared. Also, the values of $\omega_{\text{cut,ld}}$ in Fig. 4.21(a) are an overestimate

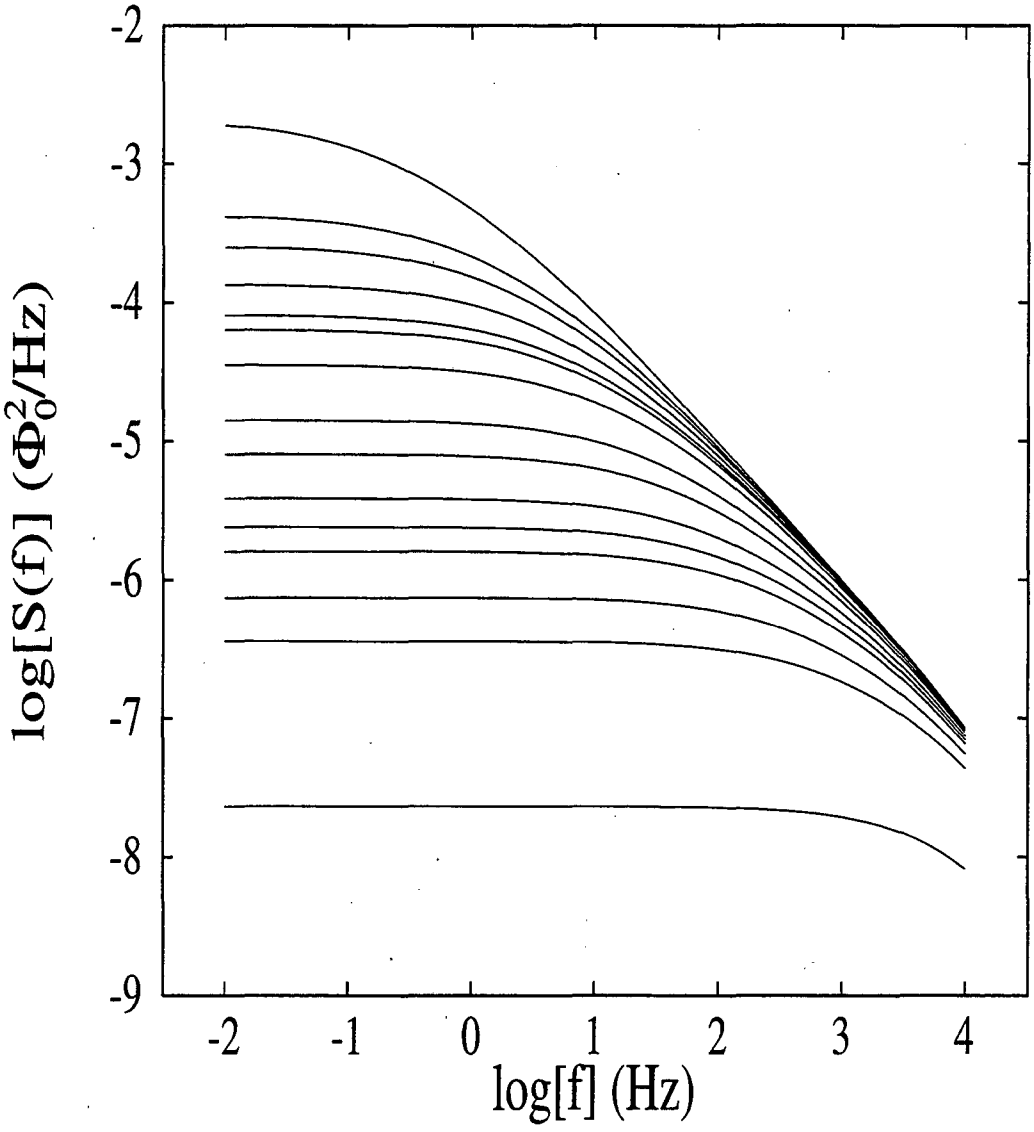

Figure 4.19: Spectral density of magnetic flux noise according to Eq. (4.51) with the additional assumption that the renormalized coupling $T'(\zeta^*) \propto \xi^4$. The parameters used were $b = 2.06$, $T_{\mathrm{KTB}} = 1.63$ K, $\omega_2 = 1.3 \times 10^7$, and for temperatures of the data shown in Fig. 4.4. T' was calculated using Eq. (4.31) and the parameters given in Table 4.1. Figure taken with permission from Ref. [2].

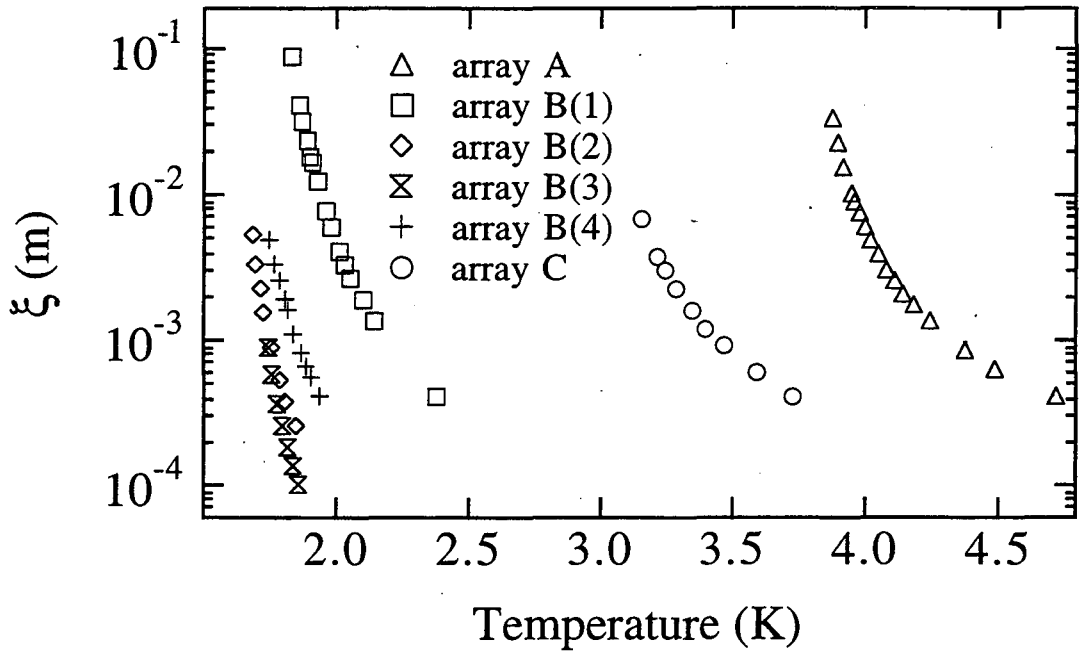

Figure 4.20: ξ versus temperature using ξ/ξ_0 from Fig. 4.11(a) and under the assumption that $\xi > \ell_{\text{eff}}$ at the highest temperature for each data set.

because the shunt resistance R is expected to be smaller than the single junction resistance[2, 76].

Although the resemblance between the predictions of this model shown in Fig. 4.19 and the data of Fig. 4.4(b) is compelling, the fact that (1) $(T'/\xi)^4$ has not been convincingly shown to be temperature independent, (2) ξ must be much larger than the array dimensions for some of the data, and (3) a crossover to $1/\omega^2$-behavior was not observed lead to the conclusion that, at present, the local damping model is not a satisfactory description of the measurements.

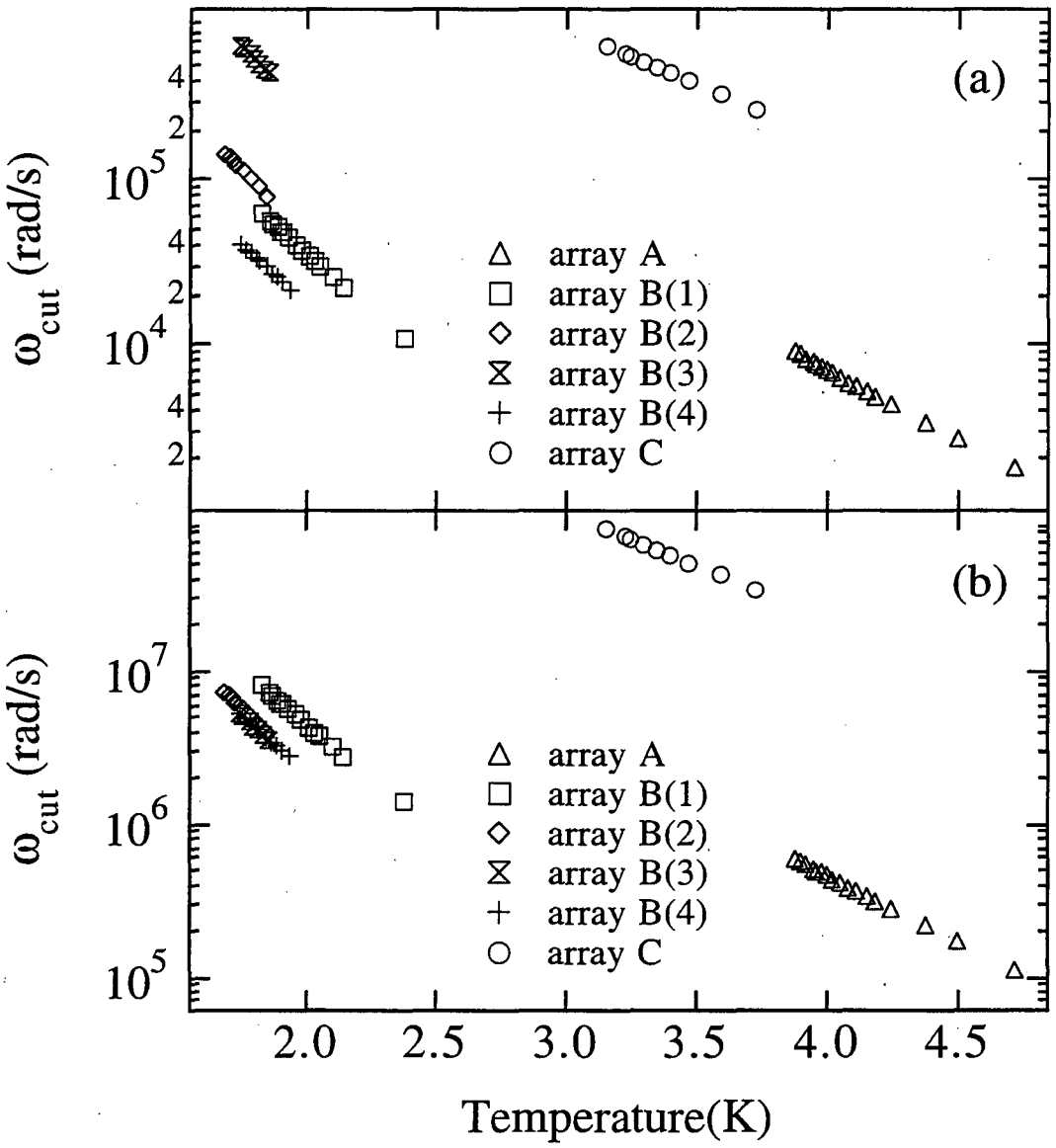

Figure 4.21: (a) $\omega_{cut,ld}$ versus temperature calculated using Eq. 4.53. (b) $\omega_{cut,ld}$ versus temperature calculated using Eq. (4.64).

4.6.4 Coulomb Gas Scaling

The two-dimensional Coulomb gas (2DCG) model has been studied intensely by Petter Minnhagen and co-workers[67] as a model for the two-dimensional superconducting/superfluid transition. In a recently published article[3], this model was used to describe vortex dynamics near the KTB transition temperature and to compare to numerical simulations of the two-dimensional XY model. The interested reader should consult Refs. [3] and [67] which contain much more detailed information about the 2DCG model, but the regime relevant to the measurements presented in Section 4.3 will be described here.

The numerical simulations began with the Hamiltonian (for zero frustration)

$$H = \sum_{\langle ij \rangle} 2E_J \left\{ 1 - \cos^{2p^2}[(\theta_i - \theta_j)/2] \right\}, \tag{4.54}$$

where θ_i is the order parameter phase at site i, $\langle ij \rangle$ denotes a sum over nearest neighbors, and the parameter p allows for increased vortex densities near the phase transition. The case $p = 1$ gives the usual 2D XY model, but the authors concentrated on $p = 2$ in order to ensure a large enough vortex density near the phase transition so that the vortex fluctuations dominated the system's response. In addition to the static Hamiltonian given by Eq. (4.54), Ginzburg-Landau dynamics were introduced into the problem through the Langevin equation,

$$\hbar \frac{d\theta_i(t)}{dt} = -\Gamma \frac{\partial H}{\partial \theta_i} + \eta_i(t), \tag{4.55}$$

where Γ is a diffusion rate and $\eta_i(t)$ is a fluctuating noise source satisfying the condition

$$\langle \eta_i(t) \eta_j(t') \rangle = 2\Gamma k_B T \delta_{ij} \delta(t - t'). \tag{4.56}$$

In order to compare the results of the numerical simulations to analytic predictions, the authors use the Minnhagen phenomenology (MP) description. In the MP description, and in the long-wavelength limit, the imaginary part of the vortex dielectric constant is given by

$$Im\left[\frac{1}{\epsilon(\omega)}\right] = -\frac{2}{\pi \tilde{\epsilon}_{cg}} \frac{\omega \omega_{cg}}{\omega^2 - \omega_{cg}^2} \ell n \left(\frac{\omega}{\omega_{cg}}\right), \tag{4.57}$$

where

$$\omega_{cg} \propto \sqrt{T' - T'_{KTB}}\, e^{-const/\sqrt{T' - T'_{KTB}}}. \tag{4.58}$$

Equations (4.57) and (4.58) are valid in the regime where $n\lambda_{cg}^2 \gg 1$, where n is the total vortex density and λ_{cg} is the Coulomb gas screening length and is related to the correlation length via

$$\lambda_{cg}^2 = \frac{\tilde{\epsilon}_{cg} T' \xi^2}{2\pi}. \tag{4.59}$$

Next, the flux noise was related to the imaginary part of the dielectric constant via $S_\Phi(\omega) \propto (T'/\omega)|Im[1/\epsilon(\omega)]|$, which, using Eq. (4.57), gave

$$S_\Phi(\omega) \propto \frac{T'}{\tilde{\epsilon}_{cg}} \frac{\omega\omega_{cg}}{\omega^2 - \omega_{cg}^2} \ell n(\omega/\omega_{cg}). \tag{4.60}$$

Shown in Fig. 4.22 is a plot of $(\tilde{\epsilon}_{cg}/T')S_\Phi^{cg}(\omega)$ versus ω, from the simulations and using $p = 2$. There is a narrow frequency region where the noise has a $1/\omega$-behavior, but far too narrow a region to agree with the many decades of $1/\omega^\alpha$-behavior observed in the data of Fig. 4.4. However, using the value $p = 1$ appropriate for the pure XY model, the authors observed the noise spectrum shown in Fig. 4.23 in which there is a much larger region of $1/\omega$-behavior. and an approach to $1/\omega^{3/2}$ above a cutoff frequency ω_{cut}.

A few comments about the simulations are necessary here. First, they do not show a crossover to white noise at low frequencies, most likely because they were interested in probing the critical dynamics and did not extend the frequency range to low enough frequency to probe the dynamics outside of the critical region. This can be seen explicitly by examining Figs. 4.22 and 4.23, where the lowest frequencies studied were about two orders of magnitude below $\Gamma E_J/\hbar$ which, as discussed below, is a very high frequency. Second, the crossover to $1/\omega^{3/2}$-behavior, not present in the data of Section 4.3, is not necessarily inconsistent with the data. The reason for this can be seen by making a rough estimate for the cutoff frequency ω_{cut}. Setting $p = 1$ in the Hamiltonian of Eq. (4.54) and substituting in to the Langevin equation, Eq. (4.55), gives (ignoring the fluctuating noise term)

$$\frac{d\theta_i}{dt} = -\Gamma E_J \sum_{ij} \sin(\theta_i - \theta_j). \tag{4.61}$$

Equation (4.61) is remarkably similar to the Josephson equation for the time derivative of the phase difference between sites i and j,

$$\frac{d(\theta_i - \theta_j)}{dt} = \frac{4r_n E_J}{\hbar^2} \sin(\theta_i - \theta_j). \tag{4.62}$$

Essentially, the phase diffusion equation, Eq. 4.61, indicates a local rate of phase change at site i based on the phase of it's nearest neighbors but ignores the long-range interaction

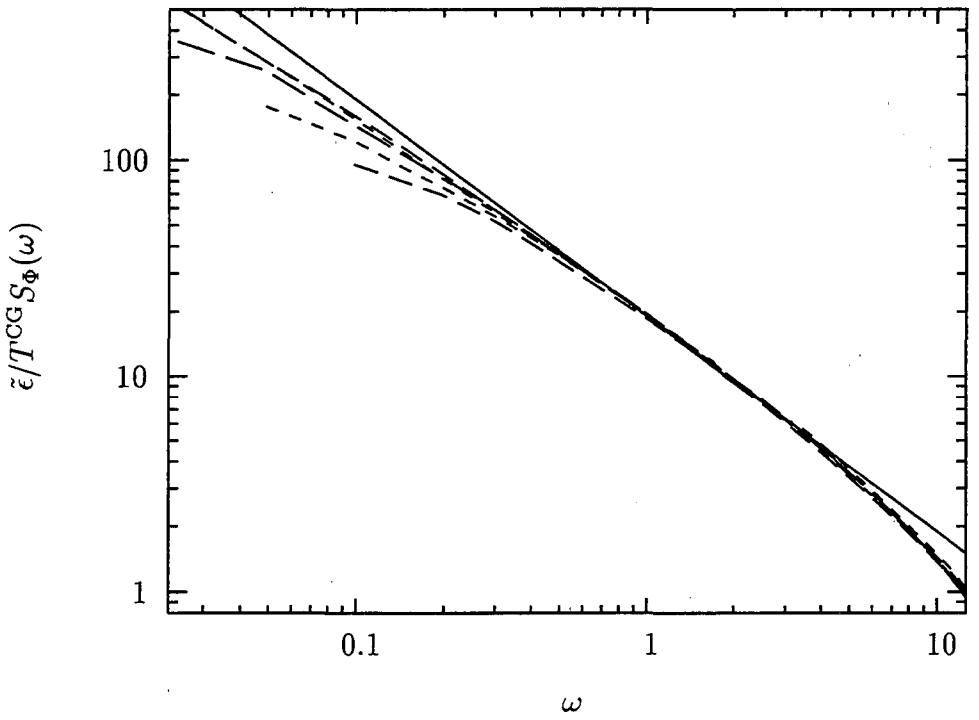

Figure 4.22: $S_\Phi^{cg}(\omega)$ versus ω on a log-log plot, for five temperatures above T'_{KTB} ($T^{CG} \equiv T'$). The upper short dashed, upper medium dashed, long dashed, lower short dashed, and lower medium dashed curves correspond to $T'/T'_{KTB} \approx 1.1, 1.3, 1.4, 1.6,$ and 1.75 respectively. The full line has slope -1. Figure taken with permission from Ref. [3].

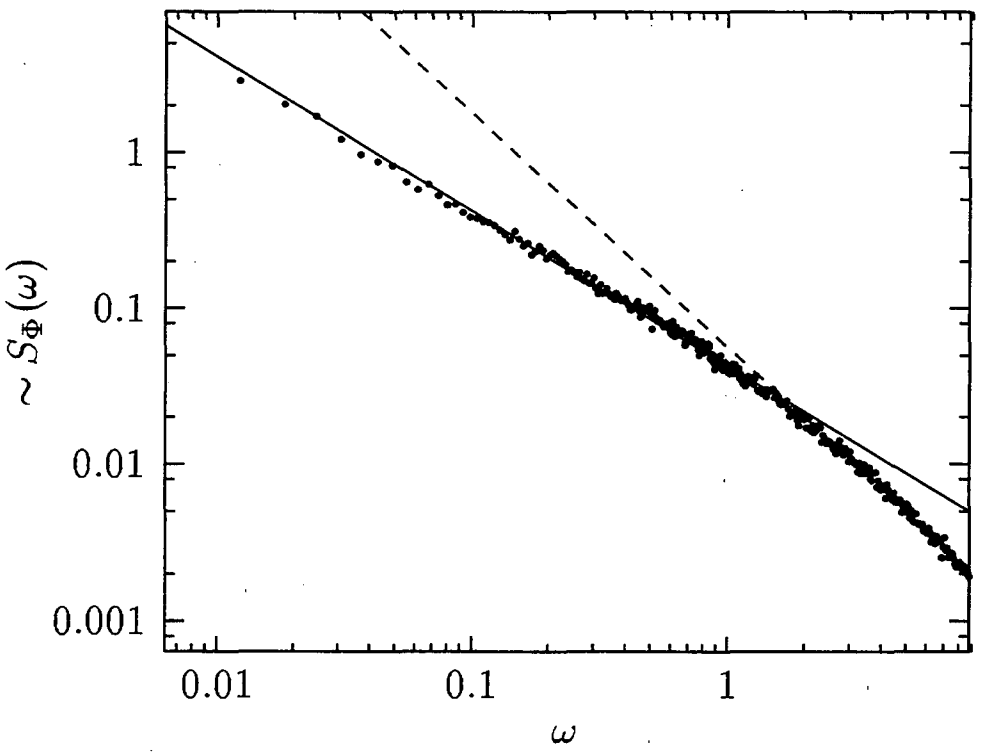

Figure 4.23: $S_\Phi^{cg}(\omega)$ versus ω on a log-log plot, for a temperature very near T'_{KTB} from numerical simulations of Section 4.6.4 with $p = 1$. The solid line has slope -1 and the dashed line has slope $-3/2$. Figure courtesy of A. Jonsson.

of the Josephson relation, Eq. (4.62), resulting from the fact that site j is coupled to its neighbors, which are in turn coupled to their neighbors, and so on. Nevertheless, making a crude comparison of Eqs. (4.61) and (4.62) indicates that

$$\Gamma = \frac{4e^2 r_n}{\hbar^2}. \tag{4.63}$$

Since the simulations indicate that the cutoff frequency, above which the noise has a $1/\omega^{3/2}$-behavior, occurs at $\omega_{\rm cut} \approx \Gamma E_J/\hbar$, Eq. (4.59) predicts that

$$\omega_{\rm cut} \approx \frac{4e^2 r_n E_J}{\hbar^2}. \tag{4.64}$$

Shown in Fig. 4.21 is a plot of $\omega_{\rm cut}$ versus temperature calculated from Eq. (4.64) using the values of E_J calculated from the measured critical currents just as was done in Section 4.4. For all of the arrays, $\omega_{\rm cut}$ is far above the experimental bandwidth and it is therefore not surprising that the measurements in Fig. 4.4 do not display $1/\omega^{3/2}$-behavior at high frequencies.

Given that the numerical simulations presented above, for the $p = 1$ case, exhibit a $1/\omega$ noise region and also that the lack of a crossover to $1/\omega^{3/2}$ in the measurements is understandable, it is reasonable to conclude that the XY model with Ginzburg-Landau dynamics is at least a possible explanation of the measurements. However, one aspect of the simulations which is clearly inconsistent with the measurements is the range of temperatures above $T_{\rm KTB}$ for which the simulations agreed with the data. Even for the $p = 2$ case, shown in Fig. 4.23, which exhibited critical dynamics over a larger temperature range than for the $p = 1$ case, the $1/\omega$ region extended at most two orders of magnitude below $\omega_{\rm cut}$ at a temperature $T'/T'_{\rm KTB} \approx 1.1$. As described in relation to Fig. 4.21(b), $\omega_{\rm cut}$ lies outside of the experimental bandwidth and the noise data exhibited $1/\omega$-like behavior over many decades in frequency, even for temperatures $T'/T'_{\rm KTB} \gg 1$ (a plot $T'/T'_{\rm KTB}$ for the temperatures at which the noise data of Fig. 4.4 is shown in Fig. 4.24). As mentioned in Section 4.5, most experimental measurements have observed KTB-like behavior at temperatures which are theoretically outside of the range of validity of the KTB model. The Coulomb gas predictions are expected to be valid over a wider range of temperatures[67], but the numerical simulations presented above do not provide an adequate description of the measurements presented in Section 4.3.

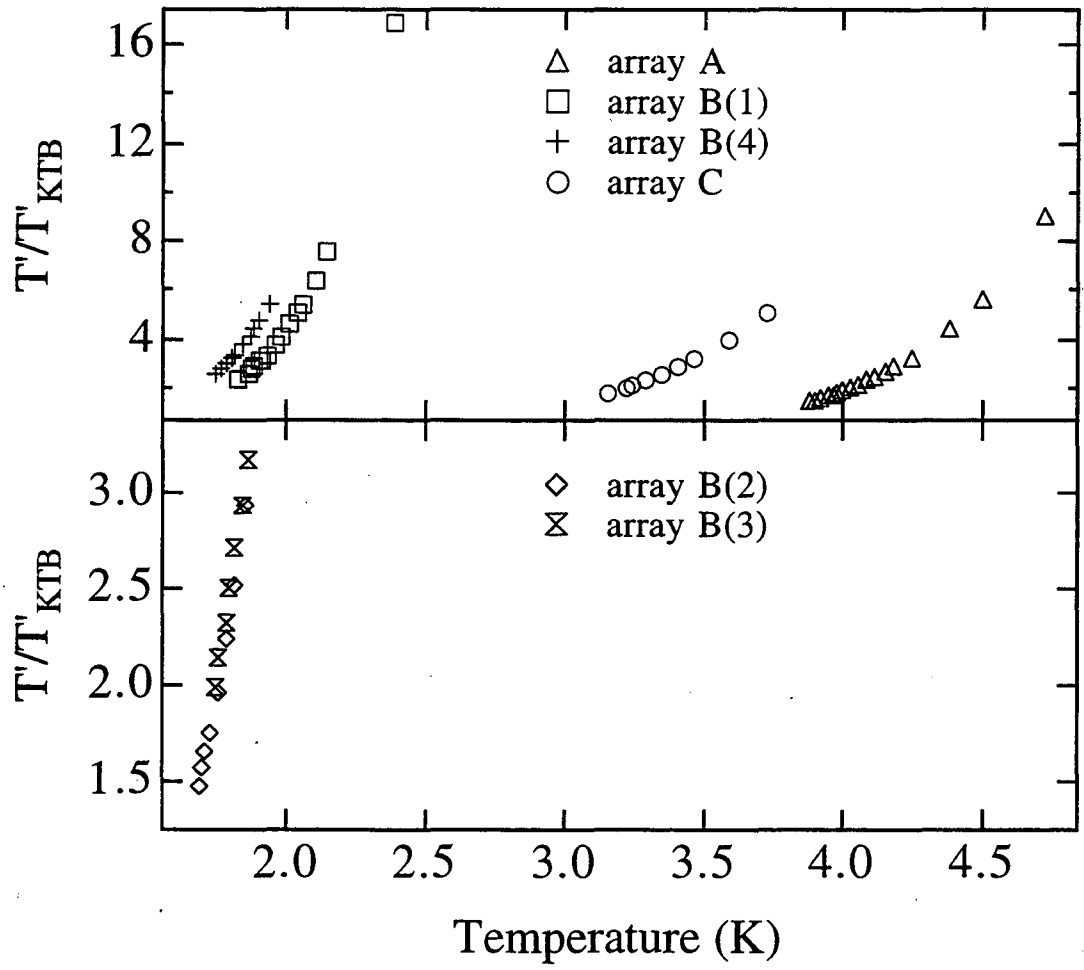

Figure 4.24: T'/T'_{KTB} versus temperature for the noise data measurements shown in Fig. 4.4.

4.6.5 Numerical Simulations Based on the Resistively Shunted Junction Model and Time-Dependent Ginzburg-Landau Dynamics

In order to study the dynamics associated with the KTB transition in Josephson junction arrays, Tiesinga *et al.*[4, 77] carried out numerical simulations for two types of dynamics, one based on the resistively shunted junction (RSJ) model which is used extensively in the treatment of single junctions, and another based on time-dependent Ginzburg-Landau (TDGL) dynamics. The equation of motion for the order parameter phase of both models can be written in the form

$$\frac{\partial\theta(r,t)}{\partial t} = \sum_{r'} \Gamma(r,r') \frac{\partial H}{\partial\theta(r',t)} + W(r,r',t), \tag{4.65}$$

where $\Gamma(r,r')$ is the damping function, $H = E_J \cos[\theta(r',t) - \theta(r,t)]$ is the Hamiltonian, and $W(r,r',t)$ is the noise function.

The difference between the RSJ and TDGL models is that in the RSJ model, current is conserved, *i.e.* current at site r can only flow to its neighbors, while for the TDGL model current is not conserved (this is sensible only for SNS arrays with a normal metal underlayer where the current can flow to the underlayer). To be more specific, for the RSJ model

$$\Gamma_{\mathrm{RSJ}}(r,r') \equiv \Gamma_0 G(r,r'), \tag{4.66}$$

where $G(r,r')$ is the two-dimensional lattice Green's function which accounts for current conservation at each site. The noise function $W_{\mathrm{RSJ}}(r,t;r',t') \equiv \eta_{\mathrm{RSJ}}(r,t;r',t')$ is defined as random, Gaussian noise such that

$$\langle \eta_{\mathrm{RSJ}}(r,t;r+e_i,t') \rangle = 0 \tag{4.67}$$

$$\langle \eta_{\mathrm{RSJ}}(r,t;r+e_i,t') \eta_{\mathrm{RSJ}}(r',t;r'+e_j,t') \rangle = 2\Gamma_0 T' \delta_{i,j} \delta(r-r') \delta(t-t'), \tag{4.68}$$

where e_j is a vector of one lattice spacing in direction j. For the TDGL model

$$\Gamma_{\mathrm{TDGL}} \equiv \Gamma_0 \delta(r-r') \tag{4.69}$$

and the noise function $W_{\mathrm{TDGL}}(r,t;r',t') \equiv \eta_{TDGL}(r,t)\delta(r-r')\delta(t-t')$ is again random, Gaussian noise defined such that

$$\langle \eta(r,t) \rangle = 0 \tag{4.70}$$

$$\langle \eta(r,t) \eta(r',t') \rangle = 2\Gamma_0 T' \delta_{i,j} \delta(r-r') \delta(t-t'). \tag{4.71}$$

The numerical simulations were then carried out on a 64×64 array, and the flux noise was calculated by covering the array with sensors of size $\ell_{\rm eff} \times \ell_{\rm eff}$ (4 sensors if $\ell_{\rm eff} = 32$, 16 sensors if $\ell_{\rm eff} = 16$ and etc.) and determining the vortex number noise in the time domain

$$g^V_{\ell_{\rm eff}}(t) \equiv \frac{1}{N_{\ell_{\rm eff}}}[\langle N^i_{\ell_{\rm eff}}(t) N^i_{\ell_{\rm eff}}(0)\rangle - \langle N^i_{\ell_{\rm eff}}(0)\rangle^2], \tag{4.72}$$

where $N^i_{\ell_{\rm eff}}(t)$ is the number of vortices under sensor i at time t. The spectral density of flux noise was determined by carrying out the Fourier transform of Eq. (4.72), and is shown in Fig. 4.25(a) for TDGL dynamics and in Fig. 4.25(c) for RSJ dynamics. Both types of dynamics exhibited $1/\omega^\alpha$-behavior at high frequencies and approaching white noise at low frequencies, with the slopes α near 1 but slightly larger for RSJ than for TDGL dynamics.

The major difference between the results for the two different dynamics appeared in the determination of the dynamic critical exponent z. In order to determine z, the correlation length was determined by calculating the zeroth-momentum phase correlation function from the equilibrium phase correlation function $g_\theta(r,t;r',t') \equiv \langle e^{[\theta(r,t)-\theta(r',t')]}\rangle$ and fitting it to form

$$g_\theta(r) \propto r^{-T'/2\pi} e^{r/\xi(T)}, \tag{4.73}$$

with ξ as given in Eq. (4.34). Then, a data collapse of $g^V_{\ell_{\rm eff}}(t)$ was performed by scaling the results from different temperatures and sensor sizes using the scaling form $g^V_{\ell_{\rm eff}}(t) \propto F_{\ell_{\rm eff}}(t/\tau_\xi)$ with $\tau_\xi \propto \xi^z$. Shown in Figs. 4.25(b) and 4.25(d) is the result of this procedure for TDGL and RSJ dynamics respectively, with the insets showing the resultant values of τ_ξ used to extract z. The somewhat surprising result was that $z(TDGL) \approx 2$ whereas $z(RSJ) \approx 0.9$. Clearly, the TDGL results provide a much better agreement with the data, for both z and the high-frequency slopes α. This is not surprising since, as mentioned in Section 4.6.3, the phase damping due to the shunt resistance from an island to the copper underlayer can dominate over that due to the junction resistance. In fact, these simulations indicate that this is likely the case.

The most striking aspects of these simulations are that they exhibit both white noise at low frequencies and $1/\omega^\alpha$-behavior, with $\alpha \approx 1$, at high frequencies and also exhibit this behavior at temperatures where the correlation length $\xi < \ell_{\rm eff}$. This latter result supports the assumption in Section 4.4 that the correlation length is smaller than the sensor's effective width, in contrast to the condition required for the local damping model of Section 4.6.3 that $\xi \gg \ell_{\rm eff}$. In addition, the data collapse in Figs. 4.25(b) and 4.25(d) was independent of the

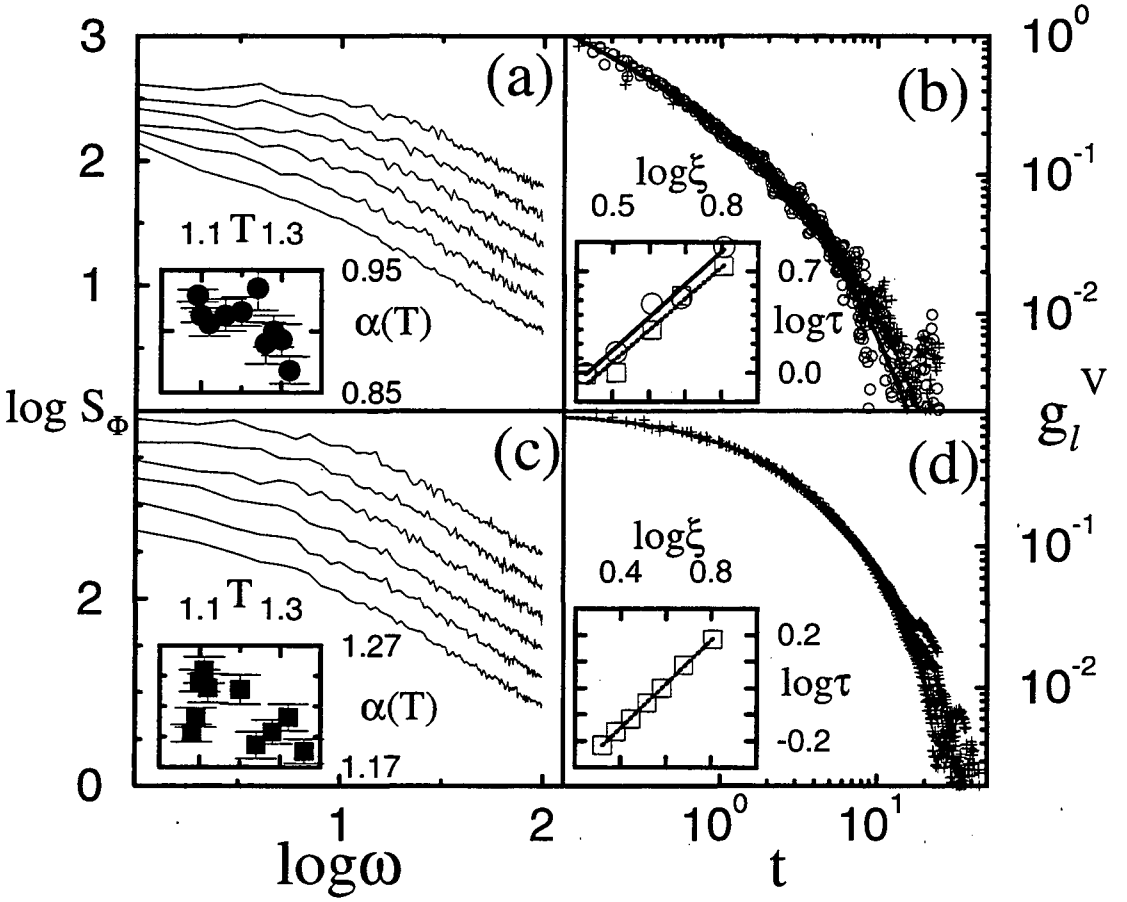

Figure 4.25: $S_\Phi(\omega)$ versus ω for (a) TDGL and (b) RSJ dynamics. The curves at different temperatures have been shifted vertically for clarity. From top to bottom, the temperatures for each spectrum are: (a) T'=1.08,1.16,1.24,1.32, and 1.48 (b) T'=1.08,1.10,1.12,1.20,1.28, and 1.36. The insets to (a) and (c) show the high-frequency slopes of each spectrum versus T' The collapse results for $g^V_{\ell_{\rm eff}}(t)$ are shown for (b) TDGL dynamics at temperatures T'=1.12,1.16,1.20,1.24, and 1.28 and (d) RSJ dynamics at temperatures T'=1.12,1.16,1.20,1.24,1.28,1.32, and 1.36 with (+) showing the results using a SQUID with $\ell_{\rm eff} = 16$ and (∘) denoting a SQUID with $\ell_{\rm eff} = 32$. The insets to (b) and (d) show the scaling of τ_ξ versus ξ for (□) $\ell_{\rm eff} = 16$ and (∘) $\ell_{\rm eff} = 32$. The dot-dashed (continuous) line is a linear fit to the $\ell_{\rm eff} = 16$ ($\ell_{\rm eff} = 32$) data. Figure taken with permission from Ref. [4].

size of the array and the sensor, supporting the conclusion in Section 4.4 that the scaling function $\mathcal{F}_2$ is independent of geometrical parameters.

4.6.6 Summary of Other Theories

None of the theories presented in this section gave a completely satisfactory description of the measurements of Section 4.3, and the numerical simulations lent support to the measurements but did not give sufficient insight to the problem to allow the determination of a correct theory. However, before discussing in detail the conclusions that can be gained from the material presented so far, an aspect of the measurements not previously discussed will be covered–namely the effects of the small background magnetic field in which the arrays were cooled.

4.7 Magnetic Field Effects

As mentioned in Section 4.3, the background field present inside the mu-metal shield produced an unknown frustration of less that 4% for array A and less than 5% for arrays B and C. A hint of these effects can be seen in Fig. 4.26(a), which exhibited qualitatively different behavior than the data from the six measurements shown in Fig. 4.4. Rather than showing white noise, the slope of the low frequency portion of the spectra show a non-zero slope which becomes more negative as temperature is lowered. These data were data taken on array C using SQUID 3 at several different temperatures. One possible explanation for this behavior is that the unknown background magnetic field was larger in this case than for the data of Fig. 4.4, so that there was a substantial number of vortices created by this field. As temperature was lowered, the density of thermally-created free vortices decreased and the behavior began to be dominated by the field-created vortices.

In an attempt to understand this behavior, a superconducting persistent-field coil [see Fig. 2.2(b)] was used to apply a magnetic field to array C while measuring $S_\Phi(\omega)$ using SQUID 1. Shown in Fig. 4.26(b) are noise spectra, at fixed temperature, for five different values of applied frustration: $f_{\rm app} = 0\%, -4\%, -6\%, -8\%, \text{and} -20\%$. There is obviously a strong magnetic field dependence. The data for $f_{\rm app} = 0\% \text{and} -20\%$ do not extend to low enough frequency to see if the noise becomes white at low frequency. However, the data at $f_{\rm app} = -4\%, -6\%, \text{and} -8\%$ do not look even qualitatively similar to either the data in Fig. 4.4 or Fig. 4.26(a). There are two regions of $1/\omega^\alpha$ noise with different slopes as in Fig. 4.26(a), but there is a rapid upturn in S_Φ at the lowest frequencies. A likely explanation for this behavior is that the superconducting washer of the SQUID [see Fig. 2.2] distorted the magnetic field lines and therefore produced a very non-uniform field at the array. This behavior likely did not occur previously, even though the fields applied were of the same order of magnitude as the ambient field, because in the measurements taken in the absence of an applied field, the SQUID did not cool below its transition temperature until after the background field was frozen in to the lead shield surrounding the vacuum can. In this situation, the background field would be trapped in the SQUID washer in the form of vortices and the field distribution would be more uniform than if the field were applied with the SQUID washer in a superconducting state.

To address the question of the distortion of the magnetic field due to the presence of the SQUID washer, a resistive heater was attached to the SQUID chip, allowing the

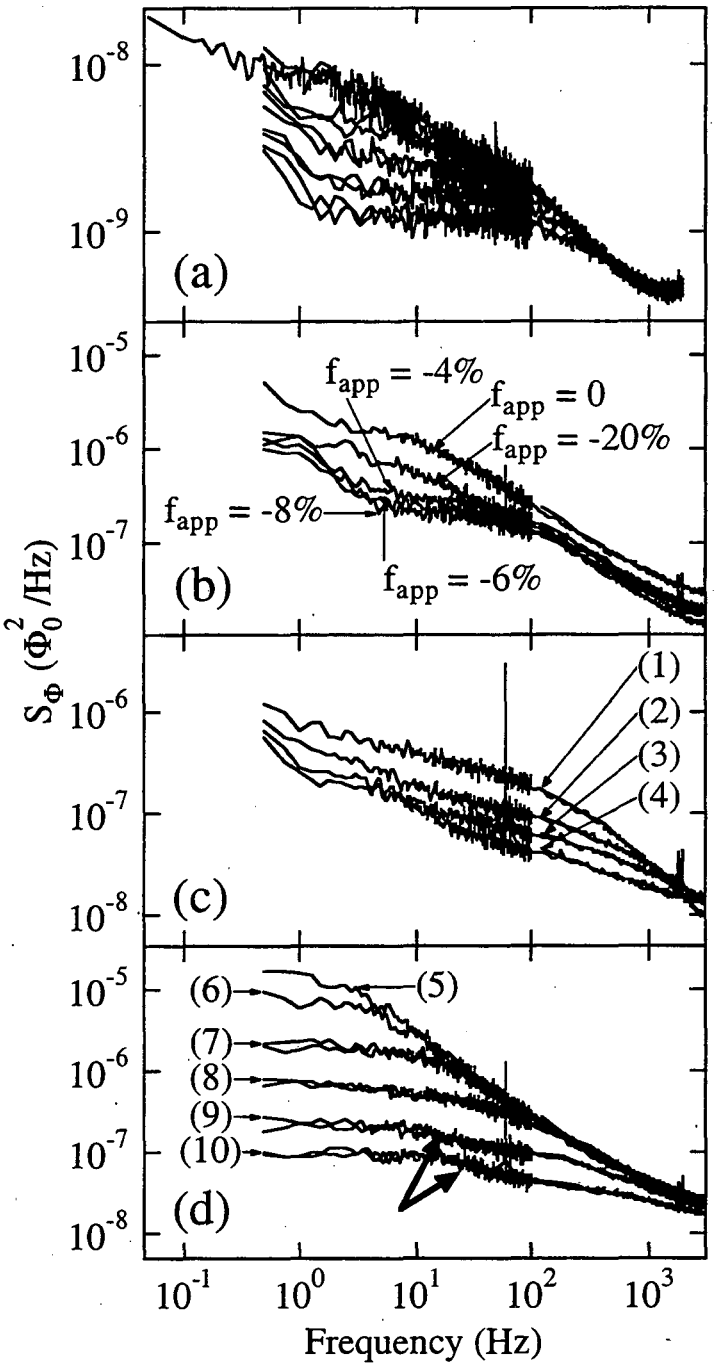

Figure 4.26: $S_\Phi(\omega)$ versus frequency of array C measured with SQUID 3 showing: (a) a situation where the low frequency noise is not white in the absence of an applied frustration, (b) effects caused by a frustration applied with the persistent current coil [see Fig. 2.2], (c) effects caused by a frustration applied by rotating the sample in the background field, and (d) effects caused by a 60 Hz external noise field.

SQUID to be heated above its transition temperature and cooled in the presence of the field. In addition, the lead can was removed from surrounding the vacuum can to allow the adjustment of $f_{\rm app}$ by rotation of the dewar in the ambient field. Shown in Fig. 4.26(c) are four sets of spectra all taken at the same temperature, labelled (1) through (4). Spectra (1) were taken first after which we removed the currents circulating in the persistent-field coil arising from any changes in ambient field. Then the spectra labelled (2) were measured. Following this, the dewar was rotated to roughly, within 10 degrees, the position where the background field was parallel to the array face. Then, the persistent current in the field coil was removed and spectra (3) were measured. At this point, the SQUID was heated and cooled in the ambient field, and spectra (4) were measured. It is evident that all these procedures had a dramatic effect on $S_\Phi(\omega)$, but none of the spectra exhibited the features seen in Fig. 4.4. The changes in frustration due to the above-mentioned procedures were less than 0.5%, which was determined by rotating the dewar more than 180 degrees while monitoring the flux through the SQUID. This change in frustration was much smaller than the maximum mentioned in Sec. 4.3.2 because the ambient magnetic field varies within the laboratory, being smaller inside the screened room where the measurements were made than in the part of the room where the apparatus was first cooled down from room temperature.

The fact that spectrum (4) does not have the form of the spectra of Fig. 4.4 is at first thought surprising, since heating and cooling the SQUID in the presence of the background field should have recreated the circumstances which produced the spectra of Fig. 4.4. However, the lack of the lead can surrounding the vacuum can resulted in a much larger level of 60 Hz noise. The ratio of S_Φ at 60 Hz to S_Φ due to the array near 60 Hz was approximately 2, 4, 40, and 60 for spectra (1) through (4) respectively. It is likely that the 60 Hz noise disrupted the equilibrium dynamics of the array. Further evidence for this hypothesis is shown in Fig. 4.26(d). The spectra of Fig. 4.26(d) were taken at six different temperatures and are labelled (5) through (10), in order of increasing temperature. They were taken with the lead can surrounding the vacuum can and the apparatus was cooled in the background field, just as for the the data of Fig. 4.4. However, there was a much larger 60 Hz external noise signal present, of unknown origin, than was present for the data of Fig. 4.4. The ratio of 60 Hz noise to array noise near 60 Hz, was approximately 3, 3, 3, 6, and 24 for spectra (5) through (10) respectively. Only the two highest temperature spectra show behavior qualitatively dissimilar to that of Fig. 4.4, namely a feature in the frequency region where white noise would be expected [see arrows in Fig. 4.26(d)]. The four lowest

temperature spectra show behavior very similar to the spectra of Fig. 4.4. This indicates that relatively small external magnetic field noise at a single frequency can disrupt the systems equilibrium dynamics. This small external 60 Hz signal, for spectra (9) and (10) in Fig. 4.26(d), corresponds to an an rms applied frustration of 1.3×10^{-5} and 9.7×10^{-6} respectively. If such a small external field source can disrupt the equilibrium dynamics of the system, the possibility of measuring the linear response by using a two-coil mutual inductance system as used by other groups [58, 78, 79] would be difficult. It should be mentioned that the 100 kHz field used to operate the SQUID corresponded to an rms frustration of approximately 10^{-4}, much larger than the 60 Hz noise in Figs. 4.26(c) and 4.26(d). The amplitude of the 100 kHz field was reduced by more than a factor of two and increased by more than a factor of three with no effect on the array's noise. Presumably the frequency was too large to affect the low frequency noise.

The data of Fig. 4.26 do not conclusively explain the fact that the high-frequency portions of the data of Fig. 4.4 exhibit different slopes. However, they do illustrate the rather strong effects that a small static or fluctuating field can have on the equilibrium noise properties of arrays and suggest that a small frustration could have caused the different values of α evident in Fig. 4.4. In addition, numerical simulations on the effects of a 2% frustration on the noise spectra of arrays found that the high-frequency slope was affected by the field, causing the slope to increase as temperature was lowered[77].

4.8 Summary, Conclusions, and Suggestions for Future Work

In summary, the spectral density of magnetic flux noise caused by the equilibrium KTB transition has been measured in three arrays of overdamped Josephson junctions using sensors of three different geometries. All of the noise data exhibited a similar form, white at low frequencies and proportional to $1/\omega^{\alpha}$, with $\alpha \approx 1$ at high frequencies. Through a data collapse, it was demonstrated that the noise obeyed dynamic scaling in agreement with the KTB theory over as many as five decades in frequency. In addition, measurement of the mutual inductance between sample and sensor as well as of flux versus time through the SQUID above and below the transition temperature extracted from the data collapse indicated that this transition temperature was indeed due to the true superconducting transition.

In addition, an analytic theory was presented based on the calculation of the vortex dielectric constant, assuming that the vortices obey diffusive dynamics. This theory described well the temperature dependence of the low frequency noise, S_{Φ}^{w}, but the $1/\omega$ frequency dependence at high frequencies was not adequately explained. From the temperature dependence of S_{Φ}^{w} and ω_{ξ} it was possible to obtain an estimate of the dynamic critical exponent which fell in the range $1.5 \lesssim z \lesssim 1.8$. However, the determination of z in this manner is of questionable validity because of the large variation of T' over the temperature ranges where $S_{\Phi}(\omega)$ was measured would indicate that z is temperature dependent, as discussed in Section 4.4 in association with Eq.(4.39). In fact, the theories of Wagenblast and Fazio and Capezzali *et al.* explicitly assumed that $z = 2$ and still found the temperature dependence $S_{\Phi}^{w} \propto T'\xi^2$ and $S_{\Phi}^{w} \propto T'\xi^2/E_J$ which would, in the same way as for the theory of Section 4.2, give a temperature dependent dynamic critical exponent.

Therefore, in contrast the the claim of Ref. [59], these measurements have not provided an unambiguous determination of the dynamic critical exponent. In order to do so, it would be necessary to have both an analytic prediction for the form of $S_{\Phi}(\omega)$ to determine the crossover frequency ω_{ξ} and also the ability to disentangle the temperature dependence of ξ from that of T'. The former is a challenge for theorists, and the hope is that the measurements presented here have given a better understanding of the dynamics of the phase transition from which theorists can begin to develop a more accurate model. The latter, namely studying the phase transition closer to the transition temperature, will likely not be possible in SNS arrays because of the strong temperature dependence of T' and the fact that the crossover frequency would be far to small to be accessible in a reasonable

measurement time. One method to possibly overcome this would be to carry out flux noise measurements on SIS arrays such as those studied by the Delft group[53, 56], since these arrays have a weakly temperature dependent critical current.

Two additional analytic theories were compared to the data, with the regime interpretation of Capezzali *et al.* in Section 4.6.2 giving nearly identical results to the theory of Section 4.2. The theory of Wagenblast and Fazio described in Section 4.6.3 gave results for $S_\Phi(\omega)$ bearing an incredible resemblance to the data of Fig. 4.4, but the issue of the renormalized coupling constant remains unresolved, as well as the issue of whether the correlation length can be much larger than the array size. Both of these theories assumed $z = 2$ and found noise spectra similar to the measurements of Fig. 4.4, and the Wagenblast and Fazio theory indicated the likelihood that local damping of the order parameter due to the shunt resistance between the islands and the metallic underlayer plays an important role in the system's dynamics.

Numerical simulations based on time-dependent Ginzburg Landau and resistively shunted junction dynamics presented in Sections 4.6.4 and 4.6.5 showed noise spectra similar to that of Fig. 4.4, and indicated that local damping is likely to be important in determining the dynamics of the phase transition in SNS arrays, in support of the Wagenblast an Fazio theory, The simulations of Tiesinga *et al.* gave evidence that the dynamic critical exponent in the local damping model $z \approx 2$ as well as indicating that the noise spectra of Fig. 4.4 are consistent with the correlation length ξ being smaller than the sensor size.

There remain unanswered two very fundamental questions regarding the superconducting transition in two-dimensional Josephson junction arrays. The first of these is the reason why nearly all experimental studies have shown results consistent with the KTB scaling predictions at temperatures far enough above the transition temperature that the KTB theory is not mathematically valid. The second is a complete understanding of the dynamics of the phase transition and the value of the dynamic critical exponent z. The former question presents a theoretical challenge which the measurements presented here can not address. However, the non-invasive measurements of the equilibrium vortex fluctuations, using a dc SQUID as a sensor, described in detail in this chapter, have shed considerable light on the latter.

In to order suggest possible future studies of the KTB transition in Josephson junction arrays, it is probably most instructive to describe what I believe to be a better measurement scheme. First, a modified sensor similar to the one used by the Neuchatel

group[58, 79], which could measure both the flux noise and the complex impedance of the array would provide much more information and would also provide a cross-check between the dissipative part of the impedance and the noise via the fluctuation-dissipation theorem. In addition, it would provide the ability to determine the transition temperature both by the data collapse of the flux noise and also by the supposed universal ratio of the dissipative to inductive components of the impedance. This measurement could be realized with a two-coil technique as shown schematically in Fig. 4.27. In this arrangement, a gradiometer consisting of a pair of superconducting, concentric, counter-wound coils is surrounded by a solenoidal drive coil, and the assembly is placed very close to the array. The leads from the top coil of the gradiometer are connected to the superconducting input coil of a SQUID, forming a closed superconducting loop. In order to measure the complex impedance, an alternating field is generated by the drive coil which is not sensed by the balanced gradiometer. However, currents generated in the sample in response to the field are picked up by the bottom coil of the gradiometer pair due to its proximity. The measurement of the flux noise then involves simply turning off the drive coil, and the bottom coil of the gradiometer senses the fluctuations in the sample. This technique, even with ideal balancing of the gradiometer and impedance matching the gradiometer to the SQUID's input coil, would not be as sensitive as the measurements presented in Section 4.3. However, for the noise measurements shown in Fig. 4.4, the noise floor of the SQUID was far below the sample noise and the reduced sensitivity would likely be acceptable.

In addition to this modified measurement scheme, it would be very instructive to study SIS arrays, because of their weakly temperature-dependent critical current as mentioned above, but also because it would shed light on the respective roles of local damping between superconducting islands and the underlying metallic ground plane and intersite damping between superconducting islands.

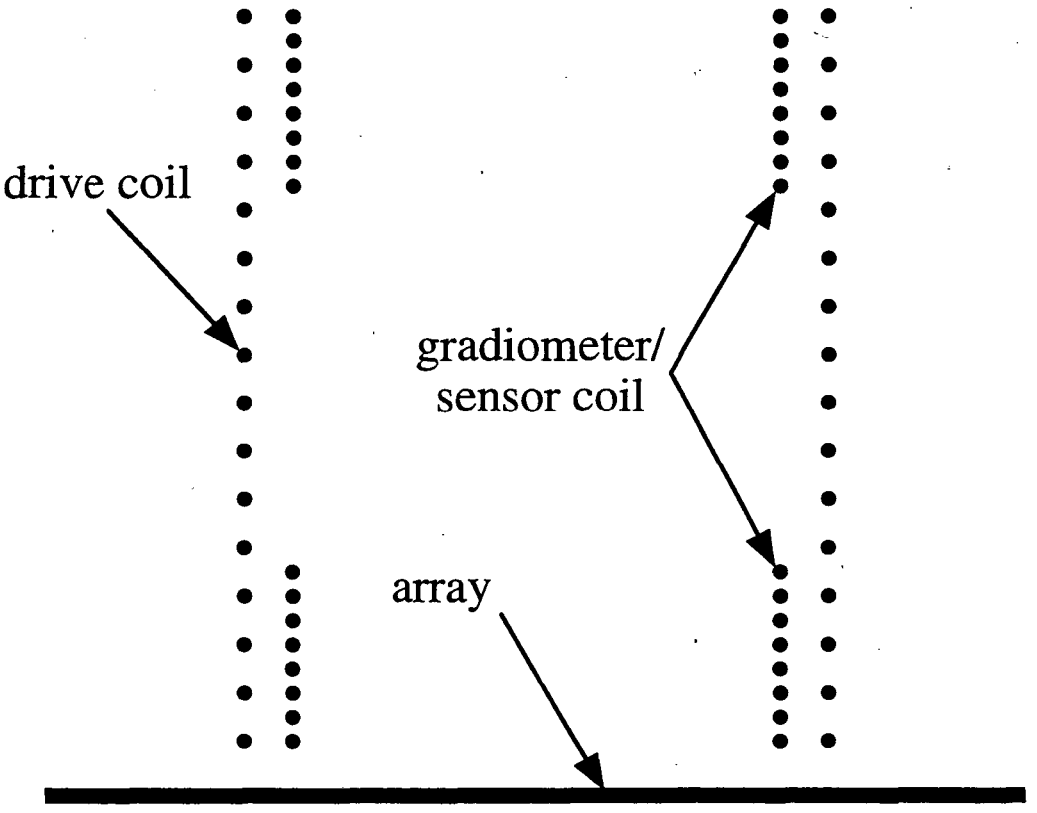

Figure 4.27: Scheme for measurement of complex impedance and flux noise.

Bibliography

[1] M. Tinkham, *Introduction to Superconductivity*, Robert E. Krieger Publishing Company, Inc., 1975.

[2] K.-H. Wagenblast and R. Fazio, unpublished, 1997.

[3] A. Jonsson and P. Minnhagen, "Characteristics of Two Dimensional Vortex Dynamics from XY-type Models with Ginzburg-Landau Dynamics", *Phys. Rev. B* **55**, 9035–9046 (1997).

[4] P. H. E. Tiesinga, T. J. Hagenaars, J. E. van Himbergen, and J. V. José, "$1/\omega$ Flux Noise and Dynamical Critical Properties of Two-Dimensional XY Models", *Phys. Rev. Lett.* **78**, 519–522 (1997).

[5] J. M. Kosterlitz and D. J. Thouless, "Ordering, Metastability and Phase Transitions in Two-Dimensional Systems", *J. Phys. C* **6**, 1181–1203 (1973).

[6] J. M. Kosterlitz, "The Critical Properties of the Two-Dimensional XY Model", *J. Phys. C* **7**, 1046–1060 (1974).

[7] V. L. Berezinskii, "[Violation of Long Range Order in One-Dimensional and Two-Dimensional Systems with a Continuous Symmetry Group]", *Zh. Eksp. Teor. Fiz. [Sov. Phys.– JETP]* **59 [32]**, 907–920 [493–500] (1970 [1971]).

[8] V. L. Ginzburg and L. D. Landau, *Zh. Eksp. Teor. Fiz.* **20**, 1064 (1950).

[9] J. Bardeen, L. N. Cooper, and J. R. Schrieffer, "Theory of Superconductivity", *Phys. Rev.* **108**, 1175–1204 (1957).

[10] L. P. Gorkov, "[Microscopic Derivation of the Ginzburg-Landau Equations in the Theory of Superconductivity]", *Zh. Eksp. Teor. Fiz. [Sov. Phys.–JETP]* **36** [**9**], 1918 [1364–1367] (1959).

[11] A. A. Abrikosov, "[On the Magnetic Properties of Superconductors of the Second Group]", *Zh. Eksp. Teor. Fiz. [Sov. Phys.–JETP]* **32** [5], 1442 [1174–1182] (1950).

[12] C. J. Lobb, D. W. Abraham, and M. Tinkham, "Theoretical Interpretation of Resistive Transition Data from Arrays of Superconducting Weak Links", *Phys. Rev. B* **27**, 150–157 (1983).

[13] A. M. Campbell and J. E. Evetts, *Critical Currents in Superconductors*, Taylor & Francis, London, UK, 1972.

[14] H. Ullmaier, *Irreversible Properties of Type II Superconductors*, Springer-Verlag, Berlin, 1975.

[15] M. Plischke and B. Bergersen, *Equilibrium Statistical Physics*, Prentice Hall, 1989.

[16] M. J. Ferrari, M. Johnson, F. C. Wellstood, J. J. Kingston, T. J. Shaw, and J. Clarke, "Magnetic Flux Noise in Copper Oxide Superconductors", *J. Low Temp. Phys.* **94**, 15–61 (1994).

[17] J. Clarke, "SQUIDs: Theory and Practice", in *The New Superconducting Electronics*, edited by H. Weinstock and R. W. Ralston, The Netherlands, 1993, Kluwer Academic.

[18] L. F. Schneemeyer, J. V. Waszczyk, T. Siegrist, R. B. van Dover, L. W. Rupp, B. Batlogg, and D. W. Murphy, "Superconductivity in $YBa_2Cu_3O_{7-\delta}$ Single Crystals", *Nature* **328**, 601–603 (1987).

[19] R. B. van Dover, E. M. Gyorgy, A. E. White, L. F. Schneemeyer, R. J. Felder, and J. V. Waszczak, "Critical Currents in Proton Irradiated Single-Crystal $Ba_2YCu_3O_{7-\delta}$", *Appl. Phys. Lett.* **56**, 2681–2683 (1990).

[20] L. Civale, A. D. Marwick, M. W. McElfresh, T. K. Worthington, A. P. Malozemoff, and F. H. Holtzberg, "Defect Independence of the Irreversibility Line in Proton-Irradiated $YBa_2Cu_3O_{7-\delta}$ Crystals", *Phys. Rev. Lett.* **65**, 1164–1167 (1990).

[21] L. Civale, A. D. Marwick, T. K. Worthington, M. A. Kirk, J. R. Thompson, L. Krusin-Elbaum, Y. Sun, J. R. Clem, and F. Holtzberg, "Vortex Confinement by Columnar Defects in $YBa_2Cu_3O_{7-\delta}$ Crystals: Enhanced Pinning at High Fields and Temeperatures", *Phys. Rev. Lett.* **67**, 648–651 (1991).

[22] R. Wheeler, M. A. Kirk, R. Brown, A. D. Marwick, L. Civale, and F. H. Holtzberg, "Columnar Defects in $YBa_2Cu_3O_{7-\delta}$", in *Phase Formation and Modification by Beam-Solid Interactions Symposium*, edited by G. S. Was, L. E. Rehn, and D. M. Follstaedt, volume 235, pages 683–688, Mat. Res. Soc., 1992.

[23] L. L. Sohn, *Geometrical Effects in Two-Dimensional Arrays of Josephson Junctions*, PhD thesis, Harvard University, 1992.

[24] J. R. Thompson, D. K. Christen, M. Paranthaman, L. Krusin-Elbaum, A. D. Marwick, L. Civale, R. Wheeler, J. G. Ossandon, P. Lisowski, and J. Ultmann, "The Impact of Tailored Defects on Length Scales and Current Conduction in High-T_c Superconductors", in *Lecture Notes in Phys.*, edited by P. K. *et al.*, pages 321–335, Heidelberg, Germany, 1996, Springer-Verlag.

[25] Y. Zhu, "Structural Defects in $Y_1Ba_2Cu_3O_{7-\delta}$ Superconductors", in *High-temperature Superconducting Materials Science and Engineering: New Concepts and Technology*, edited by D. Shi, New York, 1995, Pergammon Press, Ltd.

[26] G. Blatter, M. V. Feigel'man, V. B. Geskenbein, A. I. Larkin, and V. M. Vinokur, "Vortices in High-Temperature Superconductors", *Rev. Mod. Phys.* **66**, 1125–1388 (1994).

[27] P. Dutta, P. Dimon, and P. M. Horn, "Energy Scales for Noise Processes in Metals", *Phys. Rev. Lett.* **43**, 646–649 (1979).

[28] A. Sudbo and E. H. Brandt, "Flux-Line Tilt Moduli in Anisotropic Superconductors", *Phys. Rev. Lett.* **66**, 1781–1784 (1991).

[29] S. Machlup, "Noise in Semiconductors: Spectrum of a Two-Parameter Random Signal", *J. Appl. Phys.* **25**, 341–343 (1954).

[30] H. E. Porteanu, K. Karrai, R. Seifert, F. Koch, P. Berberich, and H. Kinder, "Microwave Fabry-Perot Transmission through $YBa_2Cu_3O_{7-\delta}$ Thin Films", *Phys. Rev. Lett.* **75**, 3934–3937 (1995).

[31] K. R. Farmer, C. T. Rogers, , and R. A. Buhrman, "Loacalized-State Interactions in Metal-Oxide-Semiconductor Tunnel Diodes", *Phys. Rev. Lett.* **58**, 2255–2258 (1987).

[32] T. T. M. Palstra, B. Batlogg, L. F. Schneemeyer, and J. V. Waszczak, "Thermally Activated Dissipation in $Bi_{2.2}Sr_2Ca_{0.8}Cu_2O_{8+\delta}$", *Phys. Rev. Lett.* **61**, 1662–1665 (1988).

[33] C. W. Hagen and R. Griessen, "Distribution of Activation Energies for Thermally Activated Flux Motion in HighT_c Superconductors: An Inversion Scheme", *Phys. Rev. Lett.* **62**, 2857–2860 (1989).

[34] C. B. Eom, J. Z. Sun, M. M. Lairson, S. K. Streiffer, A. F. Marshall, K. Yamamoto, S. M. Anlage, J. C. Bravman, T. H. Geballe, S. S. Laderman, R. C. Taber, and R. D. Jacowitz, "Synthesis and Properties of $YBa_2Cu_3O_{7-\delta}$ Thin Films Grown In-Situ by 90 Degrees Off-Axis Single Magnetron Sputtering", *Physica C* **171**, 354–382 (1990).

[35] A. Inam, X. D. Wu, L. Nazar, M. S. Hegde, C. T. Rogers, T. Venkatesan, R. W. Simon, K. Daly, H. Padamsee, J. Kerchgessner, D. Moffat, D. Rubin, Q. S. Shu, D. Kalokitis, A. Fathy, V. Pendrick, R. Brown, B. Brycki, E. Belohoubek, L. Drabeck, G. Gruner, R. Hammond, F. Gamble, B. M. Lairson, and J. C. Bravman, "Microwave Properties of Highly Oriented $YBa_2Cu_3O_{7-\delta}$ Thin Films", *Appl. Phys. Lett.* **56**, 1178–1180 (1990).

[36] J. C. Barbour, E. L. Venturini, D. S. Ginley, and J. F. Kwak, "Irradiation Effects in High Temperature Superconductors", *Nucl. Instrum. Methods B* **65**, 531–538 (1992).

[37] E. Danstker, S. Tanaka, and J. Clarke, "High-T_c SQUIDs with Slots or Holes: Low $1/f$ Noise in Ambient Magnetic Fields", *Appl. Phys. Lett.* **70**, 2037–2039 (1997).

[38] T. S. Lee, N. Missert, L. Sagdahl, J. Clarke, J. R. Clem, K. Char, J. N. Eckstein, D. K. Fork, L. Lombardo, A. Kapitulnik, L. F. Schneemeyer, J. V. Waszczak, and R. B. van Dover, "Correlation of Vortex Motion in High-T_c Superconductors", *Phys. Rev. Lett.* , 2796–2799 (1995).

[39] C. T. Rogers, K. E. Myers, J. N. Eckstein, and I. Bozovic, "Vortex Diffusion: A Path to $1/f$ Flux Noise in Thin Films of $Bi_2Sr_2CaCu_2O_8$", unpublished.

[40] C. T. Rogers, K. E. Myers, J. N. Eckstein, and I. Bozovic, "Brownian Motion of Vortex-Antivortex Excitations in Very Thin Films of $Bi_2Sr_2CaCu_2O_8$", *Phys. Rev. Lett.* **69**, 160–163 (1992).

[41] S. A. L. Foulds, J. Smithyman, G. F. Cox, and C. M. Muirhead, "Magnetic Flux Noise in Superconducting Rings and Discs Close to the Superconducting Transition", *Phys. Rev. B* **55**, 9098–9106 (1997).

[42] B. I. Halperin and D. R. Nelson, "Resistive Transition in Superconducting Films", *J. Low Temp. Phys.* **36**, 599–616 (1979).

[43] V. Ambegaokar, B. I. Halperin, D. R. Nelson, and E. D. Siggia, "Dissipation in Two-Dimensional Superfluids", *Phys. Rev. Lett.* **40**, 783–786 (1978).

[44] V. Ambegaokar and S. Teitel, "Dynamics of Vortex Pairs in Superfluid Films", *Phys. Rev. B* **19**, 1667–1670 (1979).

[45] V. Ambegaokar, B. I. Halperin, D. R. Nelson, and E. D. Siggia, "Dynamics of Superfluid Films", *Phys. Rev. B* **21**, 1806–1826 (1980).

[46] S. R. Shenoy, "Dynamic Conductivity of a Two-Dimensional Josephson Junction Array", *J. Phys. C* **18**, 5163–5189 (1985).

[47] D. J. Resnick, J. C. Garland, J. T. Boyd, S. Shoemaker, and R. S. Newrock, "Kosterlitz-Thouless Transition in Proximity-Coupled Superconducting Arrays", *Phys. Rev. Lett.* **47**, 1542–1545 (1981).

[48] R. F. Voss and R. A. Webb, "Phase Coherence in a Weakly Coupled Array of 20,000 Nb Josephson Junctions", *Phys. Rev. B* **25**, 3446–3449 (1982).

[49] D. W. Abraham, C. J. Lobb, M. Tinkham, and T. M. Klapwijk, "Resistive Transition in Two-Dimensional Arrays of Superconducting Weak Links", *Phys. Rev. B* **26**, 5268–5271 (1982).

[50] R. A. Webb, R. F. Voss, G. Grinstein, and P. M. Horn, "Magnetic Field Behavior of a Josephson-Junction Array: Two-Dimensional Flux Transport on a Periodic Substrate", *Phys. Rev. Lett.* **51**, 690–693 (1983).

[51] D. Kimhi, F. Leyvraz, and D. Ariosa, "Resistive Transition in Two-Dimensional Arrays of Proximity Josephson Junctions: Magnetic Field Dependence", *Phys. Rev. B* **29**, 1487–1489 (1984).

[52] R. K. Brown and J. C. Garland, "Effect of Magnetic-Field-Induced Frustration on the Superconducting Transition of Proximity-Coupled Arrays", *Phys. Rev. B* **33**, 7827–7829 (1986).

[53] B. J. van Wees, H. S. J. van der Zant, and J. E. Mooij, "Phase Transitions of Josephson-Tunnel-Junction Arrays at Zero and Full Frustration", *Phys. Rev. B* **35**, 7291–7294 (1987).

[54] J. P. Carini, "Magnetic-Flux Dependence of the Resistive Transition in a Square Josephson-Junction Arrray", *Phys. Rev. B* **38**, 63–73 (1988).

[55] H. S. J. van der Zant, H. A. Rijken, and J. E. Mooij, "The Superconducting Transition of 2-D Josephson-Junction Arrays in a Small Perpendicular Magnetic Field", *J. Low Temp. Phys.* **79**, 289–310 (1992).

[56] H. S. J. van der Zant, H. A. Rijken, and J. E. Mooij, "Phase Transition of Frustrated Two-Dimensional Josephson Junction Arrays", *J. Low Temp. Phys.* **82**, 67–92 (1991).

[57] D. C. Harris, S. T. Herbert, D. Stroud, and J. C. Garland, "Effect of Random Disorder on the Critical Behavior of Josephson Junction Arrays", *Phys. Rev. Lett.* **67**, 3606–3609 (1991).

[58] C. Leemann, P. Lerch, G.-A. Racine, and P. Martinoli, "Vortex Dynamics and Phase Transitions in a Two-Dimensional Array of Josephson Junctions", *Phys. Rev. Lett.* **56**, 1291–1294 (1986).

[59] T. J. Shaw, M. J. Ferrari, L. L. Sohn, D.-H. Lee, M. Tinkham, and J. Clarke, "Dynamic Scaling of the Magnetic Flux Noise Near the Kosterlitz-Thouless-Berezinskii Transition in Overdamped Josephson Junction Arrays", *Phys. Rev. Lett.* **76**, 2551–2554 (1996).

[60] D.-H. Lee, unpublished, 1996.

[61] J. Houlrik, A. Jonsson, and P. Minnhagen, "Flux Noise and Vortex Dissipation for Two-Dimensional Superconductors", *Phys. Rev. B* **50**, 3953–3958 (1994).

[62] V. Ambegaokar and B. I. Halperin, "Voltage Due to Thermal Noise in the dc Josephson Effect", *Phys. Rev. Lett.* **22**, 1364–1366 (1969).

[63] C. M. Falco, W. H. Parker, S. E. Trulliger, and P. K. Hansma, "Effect of Thermal Noise on Current-Voltage Characteristics of Josephson Junctions", *Phys. Rev. B* **10**, 1865–1873 (1974).

[64] P. G. de Gennes, "Boundary Effects in Superconductors", *Rev. Mod. Phys.* **36**, 225–237 (1964).

[65] E. Domany, M. Schick, and R. Swendsen, "First-Order Transition in an XY Model with Nearest-Neighbor Interactions", *Phys. Rev. Lett.* **52**, 1535–1538 (1984).

[66] A. Jonsson, P. Minnhagen, and M. Nylén, "New Critical Point for Two Dimensional XY-Type Models", *Phys. Rev. Lett.* **70**, 1327 (1993).

[67] P. Minnhagen, "The Two-Dimensional Coulomb Gas, Vortex Unbinding, and Superfluid-Superconducting Films", *Rev. Mod. Phys.* **59**, 1001–1066 (1987).

[68] J. Lidmar and M. Wallin, "Monte Carlo Simulation of a Two-Dimensional Continuum Coulomb Gas", *Phys. Rev. B* **55**, 522–530 (1997).

[69] M. Gabay and A. Kapitulnik, "Vortex-Antivortex Crystallization in Thin Superconducting and Superfluid Films", *Phys. Rev. Lett.* **71**, 2138–2141 (1993).

[70] C. Timm, "Generalization of the Berezinskii-Kosterlitz-Thouless Theory to Higher Vortex Densities", *Physica C* **265**, 31–39 (1996).

[71] H. Beck, "Anomolous Vortex Dynamics in Two-Dimensional Superconducting Arrays", *Phys. Rev. B* **49**, 6153–6157 (1994).

[72] I.-J. Hwang, S. Ryu, and D. Stroud, "Flux Noise and Fluctuation Conductivity in Unfrustrated Josephson Junction Arrays", unpublished.

[73] We thank M. Simkin for pointing out this fact.

[74] M. Capezzali, H. Beck, and S. R. Shenoy, "Regime Interpretation of Anomalous Vortex Dynamics in 2D Superconductors", *Phys. Rev. Lett.* **78**, 523–526 (1997).

[75] A. N. Berker and D. R. Nelson, "Superfluidity and Phase Separation in Helium Films", *Phys. Rev. B* **19**, 2488–2503 (1979).

[76] S. E. Korshunov, "Anomolous Vortex Diffusion in Proximity-Junction Arrays", *Phys. Rev. B* **50**, 13616–13621 (1994).

[77] P. H. E. Tiesinga, *Critical Fluctuations and Vortex Dynamics in Josephson-Junction Arrays*, PhD thesis, Universiteit Utrecht, The Netherlands, 1997.

[78] P. Lerch, C. Leemann, R. Théron, and P. Martinoli, "Zero Applied Force Magnetic Flux Noise in Josephson Junction Arrays", *Helv. Phys. Acta* **65**, 389–390 (1992), (The authors employed a SQUID-based measurement but found $S_\Phi(f) \propto 1/f$ for $T \leq T_{\mathrm{KTB}}$, but were not able to resolve any crossover to white noise for $T > T_{\mathrm{KTB}}$).

[79] R. Théron, J.-B. Simond, C. Leemann, H. Beck, P. Martinoli, and P. Minnhagen, "Evidence for Nonconventional Vortex Dynamics in an Ideal Two-Dimensional Superconductor", *Phys. Rev. Lett.* **71**, 1246–1249 (1993).

Ernest Orlando Lawrence Berkeley National Laboratory
One Cyclotron Road | Berkeley, California 94720

Prepared for the U.S. Department of Energy under Contract No. DE-AC03-76SF00098